UNIVERSIDAD DE CONCEPCIÓN
FACULTAD DE CIENCIAS FÍSICAS Y MATEMÁTICAS
MAGÍSTER EN CIENCIAS CON MENCIÓN EN FÍSICA

Campos Magnéticos en Binarias Cercanas

Magnetic Fields in Close Binaries

Profesor Guía: Dr. Dominik Schleicher

Departamento de Astronomía
Facultad de Ciencias Físicas y Matemáticas
Universidad de Concepción

Tesis para optar al grado de Magister en Ciencias con mención en Física

FELIPE HERNAN NAVARRETE NORIEGA
CONCEPCION, CHILE
ABRIL DEL 2019

UNIVERSIDAD DE CONCEPCIÓN

Resumen

Magnetic Fields in Close Binaries

by Felipe NAVARRETE

Las estrellas binarias cercanas *post-common-envelope binaries* (PCEBs) consisten en una Enana Blanca (WD) y una estrella en la sequencia principal (MS). La naturaleza de las variaciones de los tiempos de eclipse (ETVs) observadas en PCEBs aún no se ha determinado. Por una parte está la hipotesis planetaria, la cual atribuye las ETVs a la presencia de planetas en el sistema binario, alterando el baricentro de la binaria. Así, esto deja una huella en el diagrama O-C de los tiempos de eclipse igual al observado. Por otra parte tenemos al *Applegate mechanism* que atribuye las ETVs a actividad magnética en estrella en la MS. En pocas palabras, el Applegate mechanism acopla la actividad magnética a variaciones en el momento cuadrupolar gravitatiorio (Q) en la MS. Q contribuye al potencial gravitacional sentido por la primaria (WD), dejando así una huella igual a la observada en el diagrama O-C. Simulaciones magnetohidrodinámicas (MHD) en 3 dimensiones de convección estelar se encuentran en una etapa donde puede reproducir un gran abanico de fenómenos estelares, tales como, evolución magnética, migración del campo magnético, circulación meridional, rotación diferencial, etc. En esta tesis estudio el Applegate mechanism con dos códigos numéricos. Primero con el código MESA, un código para la evolución estelar en una dimensión. Usé este código para obtener perfiles radiales de la estrella MS en PCEBs y además determiné dónde se espera que el dínamo magnético actúe en el marco de un modelo simple. Comparando esto con el radio en donde la energía para que ocurra el Applegate mechanism se hace mínima, encontré que tales radios son los mismo para algunos sistemas. También encontré que la probabilidad de que el Applegate mechanism sea el responsable de las ETVs escala con la rotación estelar. Luego, con el código PENCIL, un código que resuelve las ecuaciones de la MHD en su formulación compresible, corrí dos simulaciones de la zona convectiva tipo Sol con velocidades de rotación diferentes. Encontré que el comportamiento de Q así como la actividad magnetica difieren entre ambas simulaciones. También hay diferentes soluciones del dínamo, momentum angular, y tensor de estrés de Reynolds. Esta es la primera vez que se establece una relación entre el dínamo y las variaciones en Q, lo cual sugiere que la solución del dínamo es la responsable de las variaciones en Q. Creemos que ésto nos podría proveer de una prometedora área para estudiar el dínamo estelar mediante ETVs, entregando una nueva herramienta para estudiar fenónemos magnético estelares.

UNIVERSIDAD DE CONCEPCIÓN

Abstract

Magnetic Fields in Close Binaries

by Felipe NAVARRETE

Post-common-envelope binaries (PCEBs) are close binary systems consisting of a White Dwarf (WD) and a main-sequence (MS) star. The nature of Eclipsing Time Variations (ETVs) PCEBs is not yet determined. On the one hand we have the planetary hypotheses, which states that the origin is a consequence of circumbinary planets which make the barycenter wobble. This will leave an imprint in the Observed-minus-calculated (O-C) diagram of the eclipsing times, the same as the observed. On the other hand we have the *Applegate mechanism*, which attributes the ETVs to the magnetic activity of the MS star. Basically, the Applegate mechanism couples the magnetic activity to gravitational quadrupole moment (Q) variations of the star. Q contributes to the gravitational potential felt by the companion, commonly a WD, and thus will a quasi-periodic variation of the Q will leave the same imprint in the O-C diagram as the one observed. 3D MHD simulations of convection in stellar convective regions are in a stage where they can reproduce a great amount of stellar phenomena, such as magnetic field evolution, magnetic field migration, meridional circulation, differential rotation, etc. In this thesis I study the Applegate mechanism with two numerical codes. First I use the MESA CODE, a one-dimensional stellar evolution code, to obtain radial profiles of MS stars in PCEBs and to determine where the magnetic dynamo is expected to take place. By comparing this to the radius at which the required energy to drive the Applegate mechanism is minimal, I found that they match in some systems. I also found that the likelihood of the Applegate mechanism being responsible of the ETVs scales with stellar rotation. Then, with the PENCIL CODE, a fully-compressible code which solves the magneto-hydrodynamic equations, I run two Sun-like convective-region simulations with different rotations and found that the behaviour of Q as well as magnetic activity is different in both simulations. They also have a different dynamo solutions, angular momentum and Reynolds stresses behaviours. This is the first time a link between the dynamo and the Q variations is made and suggests that the dynamo solution is the responsible of Q variations. We believe this will come to be a promising area to study the stellar dynamo by means of ETVs, which is a new tool to study stellar magnetic phenomena.

Acknowledgements

It would have been impossible to finish this research without the support from my friends and all the people I met on the road.

Many thanks to Edu, Hugo, Jara, Memo, Gonzalo, and Pedro, my long time friends from my hometown with whom I have never lost contact and shared uncountable laughs since we were five years old (give or take), even until today.

When I entered the university as a first year student in 2013 I came across with my friends and classmates Brits, Gorri, Gusa, Pasto, Pate, Polilla, Master Fabri, Morin, and Salmón. Also people who I met later during my time as a *tesista*: Cami, Bastián, Lientur, Matus, Rubén, and Vane.

To my parents for their support in many aspects of life. Also specially to my younger brother Pablo. Together, me and him shared long philosophical conversations about life, the cosmos, theories about why cheese is the best culinary discovery in human history, how to make the best scrambled eggs, how can a student survive without pasta and rice, etc.

Also thanks to Marcel Völschow, Jennifer Schober, and Petri Käpylä for helping me in the development of this thesis. Specially to Petri who provided me with the setup used in Chapter 5 of this work and helped me with the analysis of the simulations.

Many thanks to my supervisor, Dominik Schleicher. His guidance has been extremely important. My stays at Hamburg, Geneva, and Göttingen during October to December 2018 are a particular milestone in my time as his student. I have learned life standing lessons from his guidance.

Financial support from CONICYT (project code CONICYT-PFCHA/Magister Nacional/22181506) and FONDECYT 1161247 is acknowledged.

Analysis of the data and part of the simulations were performed using the KULTRUN cluster at the Astronomy Department of the Universidad de Concepción. Powered at NLHPC: This research was partially supported by the supercomputing infrastructure of the NLHPC (ECM-02).

Contents

List of Figures

List of Tables

Chapter 1

Introduction and Context

1.1 Importance of the study of binary stars

It is important to first state the value of studying binary systems. Important stellar parameters such as radius and mass are very difficult to obtain from isolated stars because spectroscopy will only reveal temperature. Fortunately, more than 50% of all star systems in the sky actually consist of two or more stars, and as we know classical mechanics with an exquisite precision, with the observation of eclipses and orbits (in the case of eclipsing binaries) it is easy to obtain stellar parameters of the stars in the system. This is reflected by the fact that most of our knowledge of stars come from binaries.

They also serve as celestial laboratories to test astrophysics, e.g. stellar structure and evolution, common-envelope evolution, and mass transfer, to name a few. They come in a variety of types, some being closer than others, and give rise to a wide range of physical processes.

1.2 Post-Common-Envelope Binaries

Post-Common-Envelope Binaries (PCEBs) are binary systems which normally consist of a white dwarf (WD) primary and a main sequence (MS) star, commonly an M dwarf (dM). For a binary system to reach the PCEB phase, it has to undergo a violent evolution as follows (Paczynski, 1976):

1. A MS-MS binary starts originally at a separation of $\sim$ 1 AU.
2. As the more massive star evolves faster and the binary separation is short, the secondary is engulfed by the envelope of the primary.
3. The orbital motion continues and the secondary spirals inwards towards the core of the primary as orbital energy is lost to the envelope because of the presence of frictional forces. This is known as the Common Envelope (CE) phase.
4. The CE material gains sufficient energy, so it mostly gets expelled from the system.

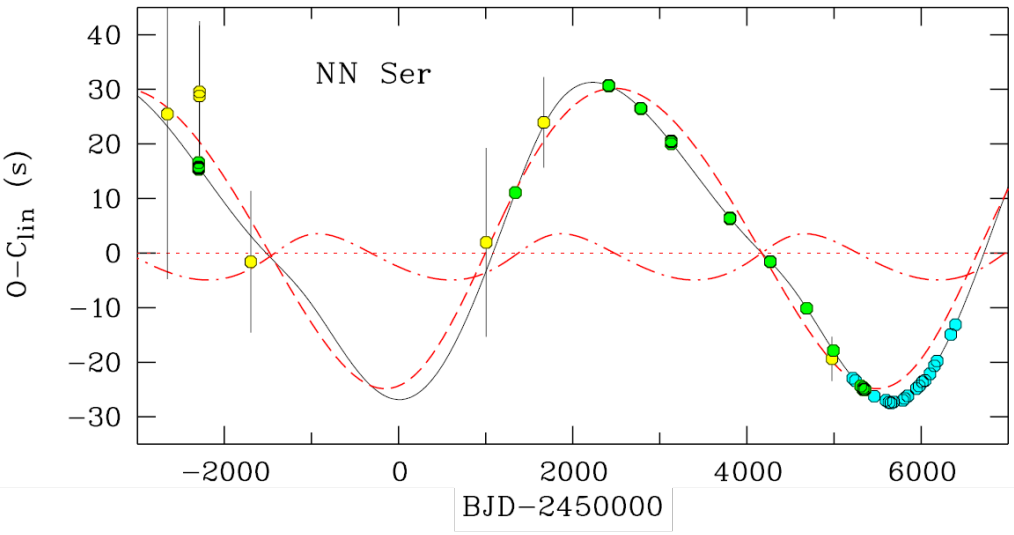

FIGURE 1.1: NN Ser O-C diagram from Beuermann, Dreizler, and Hessman (2013). Points are data, and the black line is the best fit model which is the sum of dashed and dot-dashed lines, namely the planets contributions. The horizontal dotted line marks the zero level where the data would lie if no eclipsing-time-variations are present.

5. A close binary is revealed, consisting of a WD and a low-mass MS star, with a separation of typically ~ 1 R$_\odot$ and orbital periods of less than 3 hours.

The evolution of the CE phase is not yet well understood and is a current subject of study. Apart from the common envelope evolution itself, these binaries are also being investigated for another reason. When constructing the O-C diagram of the eclipsing times, i.e. a diagram comparing the observed (O) eclipsing times with the calculated (C) ones, an intriguing characteristic is observed: periodic variations on timescales ranging from a few years to tens of years are obtained, suggesting the existence of giant planets orbiting the binary (Beuermann et al., 2010; Nasiroglu et al., 2017). There are two scenarios in which these hypothetical planets might have formed. The first one explains it via the survival of the planets during the CE phase, which were formed together with the binary (i.e. first-generation formation scenario). The second scenario is where the planets form from the CE material that is expelled from the system (i.e. second-generation formation scenario). Also a hybrid scenario is possible, where the third body formed together with the binary and later accreted material from the CE. Several studies have been carried out on this matter, some authors favoring one scenario over the other (see e.g., Völschow, Banerjee, and Hessman, 2014; Schleicher and Dreizler, 2014; Bear and Soker, 2014; Schleicher et al., 2015). In any case, these scenarios must take into account the fact that $\sim$90% of PCEBs have observed apparent period variations (Zorotovic and Schreiber, 2013). This implies that the hypothetical planets are very good at surviving the PCEB formation process and/or the CE material is very efficient in forming planets, unless the fluctuations are driven by magnetic activity.

Figure 1.1 shows the O-C diagram of NN Ser (Beuermann, Dreizler, and Hessman, 2013). Data points are in yellow, green, and cyan, and the best model is the black line which is the sum of the contributions from the two planets, the dot-dashed and dashed red lines. The variations are observed to be cyclic and for this particular system Beuermann, Dreizler, and Hessman (2013) found a two-planet stable solution.

A critical condition for making a detailed and accurate analysis is to have several data points spread across a wide range of time. For this reason it is common to find in the literature some claims of initially stable planetary solutions which are then proven to be unstable, or the other way around (see, e.g. Horner et al., 2012; Horner et al., 2013; Beuermann, Dreizler, and Hessman, 2013; Pulley et al., 2018).

There is another explanation of the eclipsing time variations known as the Applegate mechanism (Applegate, 1992), which will be explained in more detail in Chapter 2. Basically, the idea is that the magnetic activity of the MS in PCEBs redistributes the angular momentum within the star, thus changing the shape of the star, which is measured by the quadrupole moment Q. This in turn produces a change of the binary separation which translates into variations of the O-C diagram. Brinkworth et al. (2006) extended the model by introducing a finite shell formalism, considering the exchange of angular momentum between the core and the shell. Later, Völschow et al. (2016) examined and applied this model to a sample of 16 close binaries, including PCEBs, showing that the Applegate mechanism is energetically viable in the shortest and most massive binary systems. In the first part of this thesis (Chapter 4), we extend the analysis of Völschow et al. (2016) with a more detailed radial profile using the MESA code (Paxton et al., 2011) and included a new PCEB system to the data.

1.2.1 The case of V471 Tau

V471 Tau is a PCEB where the primary star is a white dwarf and the secondary is a K2V star. The K2V star has a mass of 0.93 $M_\odot$, radius of 0.96 $R_\odot$, and a surface temperate of 5040 K. The binary separation is 3.3 $R_\odot$ and the binary period is 0.522 days (Nelson and Young, 1970; Guinan and Sion, 1984; Hardy et al., 2015). The eclipsing time variations (ETVs) as seen in the O-C diagram in V471 Tau have been interpreted as caused by a circumbinary brown dwarf. While Hardy et al. (2015) reported the non-detection of the proposed third body, Vaccaro et al. (2015) proposed that the brown dwarf might have escaped detection or may have actually been seen. The later study reported the following parameters of the brown dwarf: period of 30.1 years, eccentricity of 0.39, a mass of 0.035 $M_\odot$, and an inclination of 30 deg.

More recently, Vanderbosch et al. (2017) studied the orbital period of the system and the spin period of the white dwarf. If there is a third body in V471 Tau, the O-C of the white dwarf spin period should have the same amplitude as the eclipsing time O-C. However, the authors found a flat trend scattered around zero for the former, whereas there is a clear non-linear trend for the later. They concluded that the third

body hypothesis should be ruled out for V471 Tau. However, in a short research note Marchioni et al. (2018) argued that the data covered by Vanderbosch et al. (2017) is short (∼7 years) and it was taken at the minimum of the eclipsing times O-C diagram so the effect of the third body is at its minimum. Marchioni et al. (2018) also added new data to the eclipsing times O-C and presented a new third-body interpretation analysis. After removing the 35.5 years period contribution to the proposed brown dwarf, additional O-C oscillations with a semi-amplitude of $\sim$ 20 seconds and a period of $\sim$ 9.5 years are remaining.

The case of V471 Tau reflects the difficulty of explaining the ETVs in general. This difficulty comes from both observational and theoretical sides. Firstly, it is really hard to obtain direct observations of a third body. Planets around stars in general are inferred from the stellar luminosity variability, and this is by itself a problem because in principle the photometric footprint of the third body can also be interpreted as magnetic activity, and disentangling between them is not trivial (Robertson, Roy, and Mahadevan, 2015). Spectroscopic data can also be affected by magnetic phenomena since they cause radial velocity variations that can be misinterpreted as a planetary companion (Boisse, Bonfils, and Santos, 2012; Faria et al., 2016). Secondly, simulations of magnetic activity are really expensive and the current computational power is still way behind the needed power to cover all of the physical conditions inside stars (see the thesis by Käpylä, 2006, Sect. 4.3), particularly in the convective region where the Applegate mechanism should operate.

Overall it is energetically feasible to explain ETVs in at least some PCEBs with the Applegate mechanism. This has to be confirmed with more detailed simulations and with observations. If we remember that the Applegate mechanism is a process that starts within the magnetically-active main-sequence star, then one can only probe it through the consequences it has on the surface of the star, and the binary itself. Another tool we can use is to look for the Applegate mechanism in action by means of simulations that include all physical processes relevant to the time frame of tens of years. Some of these processes are: magnetic field generation, convection, and rotation. Ideally, this model has to be self-consistent in order to look what causes the mechanism.

This thesis is structured as follows: Chapter 2 gives an overview of stellar magnetism in the Sun and other stars, followed by a section on the solar dynamo theory. Later, in Chapter 2 the Applegate mechanism is presented from a theoretical point of view and ordered by progress made over the years. Following, Chapter 3 introduces the MESA CODE and PENCIL CODE together with the setups used in the two papers of the thesis, which are included in Chapter 4 (Navarrete et al., 2018) with the 1D stellar evolution code MESA, and Chapter 5 with the 3D MHD PENCIL CODE. Conclusions and future prospects are given in Chapter 6.

Chapter 2

Magnetism in Stars & the Applegate Mechanism

In this chapter I will give an overview on our current understanding of stellar magnetism and the dynamo theory.

2.1 Magnetism in the Sun

The Sun has been under intense study since the time of Babylonians. The amount of observations of solar eclipses and solar phenomena in general has increased through history. It is of no surprise how the Sun and solar phenomena was and still is the central motivation for human religious beliefs.

There is a wide range of solar physics we can observe at its surface. For example, the *Maunder Minimum* is a period of decreased magnetic activity, inferred by the almost null report of sunspots (see Figure 2.1 for a picture of sunspots) noted by astronomers, which occurred approximately from 1645 to 1715. Carbon-14 is produced from the interaction of galactic cosmic rays (GCRs) with the earth's atmosphere. This interaction is modulated by the interplanetary magnetic field, which in turn is modulated by solar magnetic activity. C14 is then absorbed by trees and thus leaves an

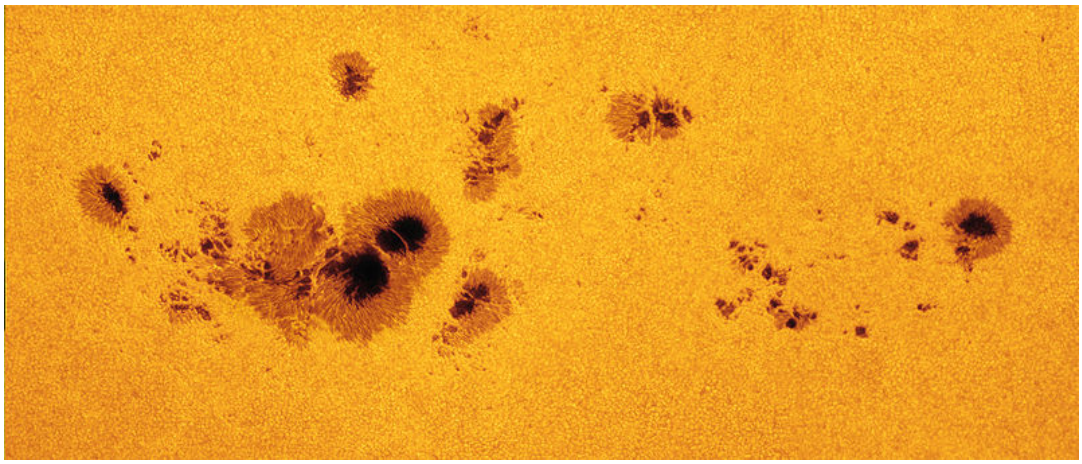

FIGURE 2.1: Some typical sunspots. Image from NASA's Goddard Space Flight Center.

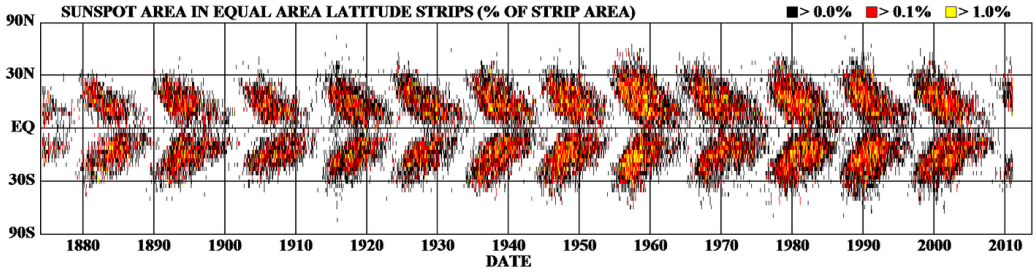

FIGURE 2.2: Solar butterfly diagram. Image from the Solar Group at the NASA Marshall Space Flight Center.

imprint in tree rings. Miyake et al. (2017) used this fact to study a long living tree and identified a peculiar event of increased concentration of C14 around 5480 BC and 5470 BC. This can be explained by a "grand solar minimum, meaning the solar activity rapidly decreased to an extremely low level, and then the solar activity became gradually higher, in a similar way to other grand solar minima" (Miyake et al., 2017).

It is clear that solar activity is quasi-periodic which means the activity level is not constant over its period and has more than one periodicity. The most well known and studied solar periodic magnetic activity is reflect in Figure 2.2, which shows the sunspot migration. At the beginning of the cycle, sunspots appear at mid latitude ($\pm$ 30°) and move towards the equator until a solar minimum is reached. This cycle lasts for 11 years and is followed by a flip of the magnetic field sign. This completes the Sun's 22-year cycle.

All solar surface phenomena start from within. The plasma contained in the last 30% of the solar interior (i.e. the convective zone) is heated by the inner radiative core where the energy, created in the core, is carried by photons. The heating of the bottom part of the convective zone makes the material move towards the surface, gradually cooling down. This motion is known as *convection* and, together with differential rotation, is responsible of the generation, amplification, and cyclic behaviour of the magnetic field. The dynamo theory, which explains the generation, amplification, and reconstruction of the magnetic field is treated in Section 2.3.

2.2 Magnetism in other stars

From early observations, more modern tools like satellite solar observations, and helioseismology we know a lot of what is happening inside and outside the Sun, making this celestial object the one we know the most about. But when we put the Sun in the bigger picture, that is compare it with other stars from an evolutive point of view or their physical properties, this statement is no longer valid. How will the solar magnetic field change over long periods of time? How will the magnetic field cycle be affected when rotation changes? How do fully convective stars evolve their magnetic fields, considering they are structurally different from the Sun?

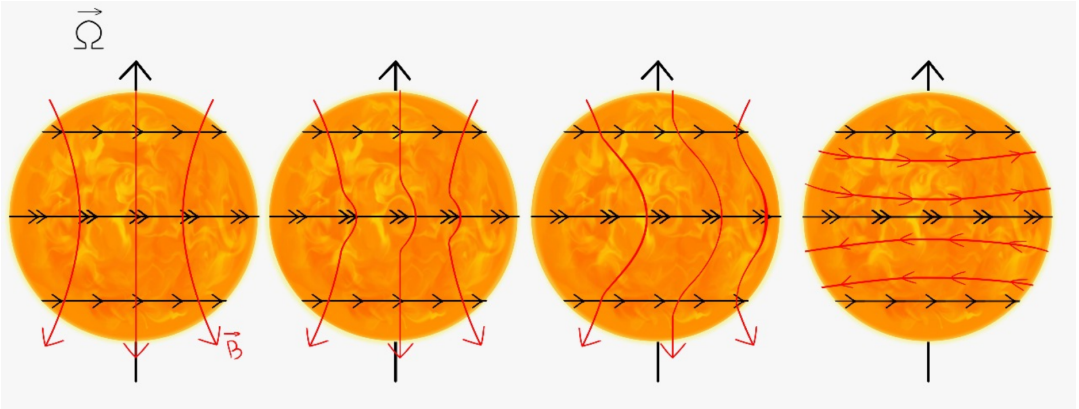

FIGURE 2.3: Visualization of the Ω effect in the Sun. The azimuthal black lines represent angular velocity, where double arrows are faster rotation. The perpendicular black line is the rotation axis marked with the rotation vector $\vec{\Omega}$. The initially poloidal magnetic field lines, in red, are twisted more are the equator because of faster rotation. The final configuration is a toroidal field.
Image credits to my friend Pedro Diaz Puig.

Stars vary in mass, radius, rotation. A complete theory that captures the magnetic activity as a function of these properties is far from being finished.

2.3 The Solar dynamo

Sunspots and all surface phenomena of not only the Sun but all stars are consequences of emerging magnetic fields from the stellar interior. The development of a theory of magnetic field generation constrained only by surface phenomena observations is an incredibly challenging task. The central part of it is turbulent convection influenced by rotation and stratification.

2.3.1 The Ω effect

When studying the dynamo action in differentially rotating spheres such as stars, the Ω effect is one of the contributions to the magnetic field generation. Its name originates from the effect differential rotation has on the initially poloidal magnetic field lines, namely a field line crossing from the north to the south pole. A Sun-like star rotates faster on the equator and slower on the poles, so a poloidal field line suffers more stretching at the equator. This effect is accumulative and the stretching becomes stronger as the star rotates, up to a point where the initially poloidal field line becomes a toroidal one. See Figure 2.3 for a visual representation.

Let us consider an axisymmetric magnetic field **B** in cylindrical coordinates (r, ϕ, z), which is given by

$$\mathbf{B} = \nabla \times \frac{\zeta}{r}\hat{\phi} + r\psi\hat{\phi}, \tag{2.1}$$

where $\zeta = \zeta(r,z,t)$ is the *poloidal flux function* and $\psi = \psi(r,z,t)$ is the *toroidal magnetic stream function*. Accordingly, we define the axisymmetric velocity field $\mathbf{U}$ as

$$\mathbf{U} = \mathbf{U}_\mathrm{p} + r\Omega\hat{\phi}, \tag{2.2}$$

where $\mathbf{U} = \mathbf{U}_p(r,z,t)$ is the poloidal velocity field in the (R,z) plane and $\Omega = \Omega(r,z,t)\hat{\phi}$ is the axisymmetric toroidal differential rotation. Furthermore, the induction equation can be written as

$$\frac{\partial \mathbf{B}}{\partial t} + \mathbf{U}\cdot\nabla\mathbf{B} = \mathbf{B}\cdot\nabla\mathbf{U} + \eta\nabla^2\mathbf{B}, \tag{2.3}$$

where η is the magnetic diffusivity and ∇^2 is the Laplacian operator. The second term on the LHS of Eq. 2.3 represents the advection term and the first term on the RHS represents the stretching. By inserting Eqs. 2.1 and 2.2 into Eq. 2.3, and separating the poloidal (ζ) and toroidal (ψ) components respectively, we are led to the equations

$$\frac{\partial \zeta}{\partial t} + \mathbf{U}_\mathrm{p}\cdot\nabla\zeta = \eta\left(\nabla^2\zeta - \frac{2}{r}\frac{\partial\zeta}{\partial r}\right) \tag{2.4}$$

and

$$\frac{\partial \psi}{\partial t} + \mathbf{U}_\mathrm{p}\cdot\nabla\psi = \mathbf{B}_\mathrm{p}\cdot\nabla\Omega + \eta\left(\nabla^2\psi + \frac{2}{r}\frac{\partial\psi}{\partial r}\right). \tag{2.5}$$

Looking into the toroidal field component equation (Eq. 2.5) we see a source term $\mathbf{B}_\mathrm{p}\cdot\nabla\Omega$ which takes the poloidal magnetic field lines and transforms them into toroidal lines by the action of differential rotation. This is know as the Ω *effect*. To sustain the dynamo action, the toroidal components must then be transformed into poloidal lines so the magnetic activity continues. In Eq. 2.4 there is no such term. This means that there is no possible way to maintain dynamo action which is a consequence of the restrictive geometric symmetry we have imposed. To summarize, a purely axisymmetric magnetic field cannot be sustained by any dynamo and must eventually decay. This is know as the *Cowling's anti-dynamo theorem* (Cowling, 1933) and it also tells us that the magnetic field in stars must be complex and an analytic treatment that assumes axisymmetric magnetic fields is not feasible.

2.3.2 The α effect

The work by Steenbeck, Krause, and Rädler (1966) uses the *mean-field magneto-hydrodynamics* approach to develop a theory in which the toroidal magnetic field is transformed into a poloidal one, thus closing the magnetic field (re-)generation cycle. This mathematical theory has proven to be an extreme success in the study of dynamo theory.

Mean-field theory

The central part of *mean-field* MHD is to split the velocity and magnetic fields into a mean part plus their corresponding fluctuations. This is done by writing

$$\mathbf{U} = \overline{\mathbf{U}} + \mathbf{u}, \tag{2.6}$$

$$\mathbf{B} = \overline{\mathbf{B}} + \mathbf{b}, \tag{2.7}$$

where the overline denotes the statistical ensemble average, and the lowercase is the fluctuating part with $\overline{\mathbf{u}} = \overline{\mathbf{b}} = 0$. By applying the Reynolds rules

$$\overline{\overline{\mathbf{P}}} = \overline{\mathbf{P}}, \tag{2.8}$$

$$\overline{\overline{\mathbf{P_1}} + \overline{\mathbf{P_2}}} = \overline{\mathbf{P}}_1 + \overline{\mathbf{P}}_2, \tag{2.9}$$

$$\overline{\overline{\mathbf{P_1}}\,\overline{\mathbf{P_2}}} = \overline{\mathbf{P}}_1\overline{\mathbf{P}}_2, \tag{2.10}$$

$$\overline{\overline{\mathbf{P}}\mathbf{p}} = 0, \tag{2.11}$$

$$\overline{\mathbf{P_1}\mathbf{P_2}} = \overline{\mathbf{P}}_1\overline{\mathbf{P}}_2 + \overline{\mathbf{p_1}\mathbf{p_2}}, \tag{2.12}$$

$$\overline{\frac{\partial \mathbf{P}}{\partial t}} = \frac{\partial \overline{\mathbf{P}}}{\partial t}, \tag{2.13}$$

$$\overline{\frac{\partial \mathbf{P}}{\partial x_i}} = \frac{\partial \overline{\mathbf{P}}}{\partial x_i}, \tag{2.14}$$

to the induction equation (Eq. 2.3), we obtain the following equation for the evolution of $\overline{\mathbf{B}}$:

$$\frac{\partial \overline{\mathbf{B}}}{\partial t} + \overline{\mathbf{U}} \cdot \nabla \overline{\mathbf{B}} = \overline{\mathbf{B}} \cdot \nabla \overline{\mathbf{U}} + \nabla \times \bar{\varepsilon} + \eta \nabla^2 \overline{\mathbf{B}}, \tag{2.15}$$

where

$$\bar{\varepsilon} = \overline{\mathbf{u} \times \mathbf{b}} \tag{2.16}$$

is the *mean electromotive force* (EMF) that drives the dynamo. By taking equation 2.3 and subtracting equation 2.15 from it, we obtain

$$\frac{\partial \mathbf{b}}{\partial t} = \nabla \times [(\mathbf{u} \times \overline{\mathbf{B}}) + (\overline{\mathbf{U}} \times \mathbf{b}) + (\mathbf{u} \times \mathbf{b} - \overline{\mathbf{u} \times \mathbf{b}})] + \eta \nabla^2 \mathbf{b}. \tag{2.17}$$

The third term inside brackets in the last equation is quadratic in fluctuations. An analytic expression of this term contains correlations of higher order in fluctuations. This is known as the *closure problem*. The second term inside brackets corresponds to the contribution the large-scale velocity field has on the small-scale magnetic fluctuations. And the first term is the contribution of the tangling and shearing of the mean field due to small-scale velocity fluctuations.

The mean-field ansatz states that the mean magnetic field $\overline{\mathbf{B}}$ varies slowly in space and time. If this holds, and we think of an inhomogeneous, stratified, anisotropic, and differentially rotating flow, then we can write the electromotive force as (Rädler,

1980):

$$\bar{\varepsilon}_i = \alpha_{ij}\overline{B}_j + (\boldsymbol{\gamma} \times \overline{\mathbf{B}})_i - \beta_{ij}(\nabla \times \overline{\mathbf{B}})_j - [\delta \times (\nabla \times \overline{\mathbf{B}})]_i + \frac{\kappa_{ijk}}{2}(\nabla_j \overline{B}_k + \nabla_k \overline{B}_j), \quad (2.18)$$

where $\boldsymbol{\alpha}$ and $\boldsymbol{\beta}$ are symmetric second-order tensors defined as

$$\alpha_{ij} = \frac{1}{2}(a_{ij} + a_{ji}), \quad (2.19)$$

$$\beta_{ij} = \frac{1}{4}(\epsilon_{ijk} b_{jkl} + \epsilon_{jkl} b_{ikl}), \quad (2.20)$$

and ϵ is the Levi-Civita pseudotensor. $\boldsymbol{\alpha}$ is know as the α-effect, related to the Parker mechanism (Parker, 1955), which can drive a large-scale dynamo by transforming a toroidal field into a poloidal one, thus ending with the problem of Cowling's anti-dynamo theorem. $\boldsymbol{\beta}$ is a turbulent magnetic diffusion. For completeness, $\boldsymbol{\gamma}$, δ, and $\boldsymbol{\kappa}$ are given by

$$\gamma_i = -\frac{1}{2}\epsilon_{ijk} a_{jk}, \quad (2.21)$$

$$\delta_i = \frac{1}{4}(b_{jji} - b_{jij}), \quad (2.22)$$

$$\kappa_{ijk} = -\frac{1}{2}(b_{ijk} - b_{ikj}). \quad (2.23)$$

The first term represents the turbulent pumping of the mean field. The last two are a pseudovector and a pseudotensor, respectively.

2.3.3 Convection

Convection is the movement a flow has when the more internal hot layers rise to the more external cooler layers. This process exchanges energy between the hotter and cooler layers. The mass elements are called *parcels*, *blobs*, *eddies* or just *mass elements*. As the hotter mass elements rise they are dissolved into their new surrounding, whereas the cooler mass elements fall into the hotter layers. In the convective region of stars the density stratification is very high, so convection is very efficient.

A realistic description of convection is extremely difficult and perhaps impossible. This is because any "complete" model of convection must be non-local and nonlinear as the full set of hydrodynamic equations must be included. It is one of the stellar processes we have the least understanding of.

The stability criterion against convection is given by the *Ledoux criterion*

$$\nabla_{\text{rad}} < \nabla_{\text{ad}} - \frac{\chi_\mu}{\chi_T}\nabla_\mu, \quad (2.24)$$

where ∇_{rad} is the radiative logarithmic temperature gradient, ∇_{ad} is the adiabatic logarithmic temperature gradient, and $\nabla_\mu = (\partial \ln \mu / \partial \ln P)$ is the logarithmic mean

molecular weight gradient. Furthermore,

$$\chi_\mu = \left(\frac{\partial \ln P}{\partial \ln \mu}\right)_{\rho,T}, \tag{2.25}$$

$$\chi_T = \left(\frac{\partial \ln P}{\partial \ln \rho}\right)_{T,X_i}, \tag{2.26}$$

where X_i means that the composition is held constant. When the composition is chemically homogeneous $\nabla_\mu = 0$, the Leudox criterion is replaced by the *Schwarzschild criterion* for stability against convection

$$\nabla_{\rm rad} < \nabla_{\rm ad}. \tag{2.27}$$

The convection criterion can also be recasted in terms of the entropy: if entropy decreases outward (with radius) at some point, then it is said that the fluid is convectively unstable and convection will thus develop.

The Rossby number (Ro) serves as a measure of the influence rotation has on the flow. It is defined as

$$\mathrm{Ro} = \frac{P_{\rm rot}}{\tau_c}, \tag{2.28}$$

where $P_{\rm rot}$ is the rotation period and τ_c is the convective turnover time. At the photosphere, $\mathrm{Ro} \gg 1$ so photospheric convection is unaffected by rotation; at the bulk of the convection zone, $\mathrm{Ro} \leq 1$ so there is a significant rotational influence; whereas at the bottom of the convective region, $\mathrm{Ro} \sim 0.1$, meaning that convection is highly influenced by rotation. This means we have another level of complexity when dealing with the convection in stars as not only convection by itself can be studied, but the influence of rotation must be included.

The Mixing Length Theory

The mixing length theory (MLT) is an analytic theory to treat convection. Here, the central idea is to consider a fluid parcel in the cooler (hotter) parts of a fluid with a temperature gradient; there is nothing special in physical terms about this fluid element compared to its surrounding. This mass element will move to the hotter (cooler) layers with the special constrain of moving a length l, i.e. the *mixing length*, before losing its identity by merging into its new surrounding. During this motion, the fluid parcel remains in pressure equilibrium with its surrounding. This idea was first proposed by Prandtl in 1925 and in its stellar form by Biermann (1951), Vitense (1953), and Böhm-Vitense (1958). Despite being very simplistic it has given many useful insight in stellar convection.

For a more complete treatment of convection see the books by Kippenhahn, Weigert, and Weiss (2012), and Hansen, Kawaler, and Trimble (2004).

2.4 Original Applegate Model

Applegate (1992) proposed an alternative method to the planetary hypothesis to explain the ETVs. The model itself relates the evolution of the magnetic field, described by the dynamo theory and explained in Chapter 2.3, to the orbital period modulations. The basic idea of the model is that some amount of angular momentum within the star is being continuously exchanged between an inner and outer convective shell of the star. The torque necessary to redistribute angular momentum is provided by a varying magnetic torque which changes together with the magnetic activity cycle.

As angular momentum is exchanged within the star, the gravitational quadrupole moment changes which can be seen as a measure of the oblateness of the star or the level of deviation from a perfect sphere. The gravitational quadrupole moment, denoted by Q is related to the gravitational potential $\phi(\boldsymbol{x})$ outside the active star via (Applegate, 1992)

$$\phi(\boldsymbol{x}) = -\frac{GM}{r} - \frac{3}{2}GQ_{ik}\frac{x_i x_k}{r^5}, \tag{2.29}$$

where $x_i, x_k = x, y, z$ denote Cartesian components and $\boldsymbol{x} = (x, y, z)$. The gravitational quadrupole moment is calculated via

$$Q_{ik} = I_{ik} - \frac{1}{3}\delta_{ik}\,\mathrm{Tr}\,I, \tag{2.30}$$

where ρ is the density,

$$I_{ik} = \int d^3x\rho(\boldsymbol{x})x_i x_k \tag{2.31}$$

is the inertia tensor, Tr I its trace, and x_i, x_k are Cartesian coordinates measured from the centre of mass of the star. For a close binary system we can assume that tidal friction has synchronized the stellar spin with the binary spin, circularized the orbit (Zahn and Bouchet, 1989), and brought the rotational and orbital angular momenta into alignment. We can adopt the z-axis to lie in the direction of the angular momentum together with an x-axis pointing at the companion, and let this coordinate system rotate about the z-axis with the angular velocity. In this coordinate system, only the Q_{xx} term contributes to the total quadrupole moment.

Then, following Applegate (1992), the variations in the binary period are related to variations in the quadrupole moment via

$$\frac{\Delta P}{P} = -9\left(\frac{R}{a_{\mathrm{bin}}}\right)^2\frac{\Delta Q_{xx}}{MR^2}, \tag{2.32}$$

or,

$$\frac{\Delta P}{P} = -9\frac{\Delta Q_{xx}}{M\,a_{\mathrm{bin}}^2}, \tag{2.33}$$

where M, R are the mass and radius of the magnetically active star, and a_{bin} is the binary separation.

Applegate worked with the assumption that variations of Q are only present on a thin shell surrounding the stellar core with a mass of $M_s = 0.1 M_\odot$. The quadrupole moment of the outer shell can be computed as

$$Q_s = \frac{1}{9} M_s R^2 \frac{\Omega^2 R^3}{GM}, \tag{2.34}$$

where Ω is the angular velocity of the shell. The derivative of Q_{xx} with respect to the angular momentum J is calculated via

$$\frac{dQ_{xx}}{dJ} = \frac{1}{3} \frac{\Omega R^3}{GM}. \tag{2.35}$$

For angular momentum transfer to take place, a torque of some nature must be present. Applegate (1992) assumes this torque to be provided by a subsurface magnetic field with a lever arm of 0.1R. The mean subsurface field is then

$$B^2 \sim \frac{GM^2}{R^4} \left(\frac{a}{R}\right)^2 \frac{\Delta P}{P_{\rm mod}}, \tag{2.36}$$

where $P_{\rm mod}$ is the orbital period modulation. The calculations yield a magnetic field strength of the order of a few kG. Applegate (1992) explained the binary period variations with a good match for different close binaries. For a period modulation with an amplitude of $\Delta P/P \sim 10^{-5}$ the mechanism requires a magnetically active star with a luminosity variation of $\Delta L/L \sim 0.1$ and a differential rotation variation of $\Delta\Omega/\Omega \sim 0.01$

This work established the basis for future attempts to explain the variations of the eclipsing times of several types of close binaries.

2.5 Brinkworth Model

Brinkworth et al. (2006) studied the eclipsing times of the PCEB system NN Ser with photometric data and found that the binary period is decreasing at a rate of $\dot{P} = (9.06 \pm 0.06) \times 10^{-12}\,\mathrm{s\,s^{-1}}$.

The original Applegate mechanism is applied considering a thin outer shell of mass $M_s = 0.1\ M_\odot$ but the M dwarf in NN Ser has a mass of 0.111 $M_\odot$, which is a common number among PCEBs (see Table 1 of Völschow et al., 2016, for a summary of relevant parameters of some PCEB systems). This raises the problem that a "thin" shell of 0.1 $M_\odot$ is not a thin shell in this context because it is a major part of the star. For this reason, Brinkworth et al. (2006) generalized the Applegate model by splitting the star into an inner core and an outer shell, denoted by subscripts 1 and 2, respectively, and including the back reaction of the core that arises from the angular momentum exchange.

The inertia momenta are calculated via

$$I = \frac{2}{3} \int R^2 \mathrm{d}M, \tag{2.37}$$

where one integral is taken for the mass encompassed by the core and another encompassing the shell. An overall change in the quadrupole moment due to a change in the angular frequencies of both the shell and the core is given by

$$\Delta Q = Q_1' \left[2\Omega_1 \Delta\Omega_1 + (\Delta\Omega_1)^2\right] + Q_2' \left[2\Omega_2 \Delta\Omega_2 + (\Delta\Omega_2)^2\right] \tag{2.38}$$

where the coefficients Q' are given by integrals over shells of the form

$$Q' = \frac{1}{9} \int \frac{R^5}{GM(R)} \mathrm{d}M, \tag{2.39}$$

and $M(R)$ is the mass inside the radius R (Brinkworth et al., 2006).

An orbital period change requires a change in the quadrupole moment which in turn requires an angular momentum transfer of $\Delta J = I_2 \Delta\Omega_2$. This leads to an energy change of

$$\Delta E = \Delta J \left(\Omega_2 - \Omega_1\right) + \frac{1}{2} \left(\frac{1}{I_1} + \frac{1}{I_2}\right) (\Delta J)^2 . \tag{2.40}$$

Combining this with a stellar density profile obtained from the Lane-Emdem equation for an $n = 1.5$ polytrope to model the secondary star, stellar parameters of $M = 0.15\,\mathrm{M}_\odot$, $R = 0.174\,\mathrm{R}_\odot$ and $\Delta P = -0.00426$ s, and assuming a differential rotation of $\Omega_2 - \Omega_1 = 0$ to obtain minimum energy, Brinkworth et al. (2006) obtained an energy requirement of a few 10^{40} ergs, which is $\sim$10 times the energy budget of the secondary in NN Ser obtained from $L_2 = 4\pi R^2 \sigma T_{\mathrm{eff}}^4$.

The main contribution of Brinkworth et al. (2006) model is that it includes the reaction of the core to the angular momentum exchange between itself and the convective shell. This makes the generalized model less energetically feasible than the original one. In the particular case of NN Ser it is then not viable to explain the eclipsing time variations with the Applegate mechanism for this system. The Brinkworth et al. model was further examined and systematically applied to PCEBs by Völschow et al. (2016).

2.6 Lanza Model

The above models focus on the energetic feasibility of the mechanism rather than trying to develop a detailed and consistent model of angular momentum transfer and magnetic field variations.

Lanza (2005) developed a more detailed mean-field model with the basic assumption that the angular velocity of a magnetically active star is a function only of the distance from its rotation axis, thus the angular velocity is constant over cylindrical surfaces co-axial with the rotation axis. This is a consequence if one assumes

the convection zone stratification to be strictly adiabatic, so the Taylor-Proudman balance can be used[1]. This model enabled Lanza (2005) to establish constraints to the amplitude and radial profile of the angular momentum variations that are needed to explain orbital period variations in a class of close binaries known as RS Canum Venaticorum (RS CVn), which present a typical relative amplitude of $\Delta P/P \sim (1-3)\times 10^{-5}$ and time-scales of about 30-50 yr (Lanza and Rodonò, 2004).

The model is as follows. A cylindrical polar coordinate system (s, z, ϕ) is adopted, with s the distance from the $\hat{z}$ axis, z the coordinate along the rotation axis, and ϕ the azimuthal coordinate. A mean-field description implies that a Reynolds decomposition is made, so for the case of the velocity field $\boldsymbol{V}$ it can then be written as

$$\boldsymbol{V} = \boldsymbol{v} + \boldsymbol{v}', \tag{2.41}$$

where $\boldsymbol{v}$ is the mean velocity and $\boldsymbol{v}'$ the velocity fluctuations with respect to the mean value at a given point and time. The anelastic approximation is adopted[2], and as the convection zone is strictly adiabatic, the energy equation reduces to the constancy of the specific entropy, so only the mass continuity equation and the equation of angular momentum conservation need to be considered. Lanza (2005) worked on solving the angular momentum equation in the form

$$\mathfrak{C}(s)\langle\rho\rangle s^2\frac{\partial\omega}{\partial t} - \frac{\partial}{\partial s}\left[\mathfrak{C}(s)s^2\langle\eta_t\rangle\frac{\partial\omega}{\partial s}\right] = \frac{\partial}{\partial s}\left\{\mathfrak{C}(s)\left[\frac{s}{\tilde{\mu}}\left(\langle B_s B_\phi\rangle + \langle M_{s\phi}\rangle\right) - s\langle\Lambda_{s\phi}\rangle\right]\right\}, \tag{2.42}$$

where terms in $\langle\cdot\rangle$ are averages of the quantity over the lateral surface of the cylinder of radius s co-axial with the rotation axis $\hat{z}$, so for a generic function f it is written as

$$\langle f\rangle \equiv \int_0^{2\pi}\int_{-\sqrt{R^2-s^2}}^{\sqrt{R^2-s^2}} s f(s,z,\phi)\mathrm{d}z\mathrm{d}\phi, \tag{2.43}$$

R is the radius of the star, $\mathfrak{C}(s) = 4\pi s\sqrt{R^2-s^2}$ is the lateral surface area of the cylinder, ρ is the density, $\omega(s,t) \equiv v_\phi(s,t)/s$ is the angular velocity, η_t is the turbulent dynamical viscosity, $\tilde{\mu}$ is the magnetic permeability, B_s and B_ϕ are the s and ϕ component of the magnetic field, $M_{s\phi} = \overline{B'_s B'_\phi}$ is the Maxwell stress tensor with the overline denoting averaging, and $\Lambda_{s\phi} = \rho\overline{v'_s v'_\phi}$ the turbulent Reynolds stress tensor. To solve Eq. 2.42, the stress-free boundary condition is applied, i.e.

$$\left(\frac{\partial\omega}{\partial s}\right)_{s_1,s_2} = 0, \tag{2.44}$$

so there is no angular momentum flux outside the domain $[s_1, s_2]$, thus ensuring angular momentum conservation.

[1]The Taylor-Proudman theorem states that if there is a balance between the Coriolis force, pressure gradients, and buoyancy forces in a compressible medium, then the angular velocity is constant along cylindrical surfaces co-axial with the rotation axis.

[2]The anelastic approximation filters out acoustic waves by eliminating the temporal derivative of the density perturbation in the mass conservation equation.

The application of this model to RS CVn systems led Lanza (2005) to reject the Applegate hypothesis because the required angular velocity variations are one or two orders of magnitude larger than the upper limits set by observations and the mechanical energy dissipated in the turbulent convection zone during one cycle of the modulation exceeds that supplied by the stellar luminosity.

Lanza (2006) extended his previous model to a more general one where the angular velocity depends on both radius and latitude. A spherical polar coordinate system is adopted (r, θ, ϕ), where r is the distance from the origin placed at the centre of the star, θ is the colatitude measured from the North Pole, and ϕ is the azimuthal angle. In the model, all variables do not depend on ϕ. The Reynolds decomposition is used, and the mean velocity field is assumed to be arising from stellar rotation $v = (0, 0, v_\phi)$ where $v_\phi = v_\phi(r, \theta, \phi)$. The density fluctuations are neglected and ϕ is assumed to depend only on r. In this case $\omega \equiv v_\phi / (r \sin\theta)$, and Eq. 2.42 can be recasted as

$$\frac{\partial \omega}{\partial t} - \frac{1}{\rho r^4}\frac{\partial}{\partial r}\left(r^4 \eta_t \frac{\partial \omega}{\partial r}\right) - \frac{\eta_t}{\rho r^4}\frac{1}{(1-\mu^2)}\frac{\partial}{\partial \mu}\left[(1-\mu^2)^2 \frac{\partial \omega}{\partial \mu}\right] = S, \tag{2.45}$$

where $\eta_t = \eta_t(t)$, $\mu \equiv \cos\theta$, and $S = S(r, \mu, t)$ is a source term given by

$$S = -\frac{\nabla \cdot \boldsymbol{\tau}}{\rho r^2 (1-\mu^2)}, \tag{2.46}$$

and $\boldsymbol{\tau}$ is a vector whose components are

$$\tau_i = r \sin\theta \left[\Lambda_{i\phi} + \frac{1}{\tilde{\mu}}(B_i B_\phi + M_{i\phi})\right]. \tag{2.47}$$

By applying the stress-free boundary condition, i.e.

$$\left(\frac{\partial \omega}{\partial r}\right)_{r_b, R} = 0, \tag{2.48}$$

Lanza (2006) worked on solving Eq. 2.45 and applied the model to a typical active component in a RS CVn system, and the author concluded that the results found in Lanza (2005) are confirmed with the extension of an angular velocity dependence on both radius and colatitude. This means the Applegate mechanism is insufficient to explain the eclipsing time variations observed on RS CVn binaries.

However, Lanza (2006) did not apply his model to other systems like PCEBs so this question remained open.

2.7 Völschow et al. (2018) model

Völschow et al. (2018) extended the Lanza (2006) model by assuming a time-dependent magnetic field, and velocity and magnetics field fluctuations in the convective zone.

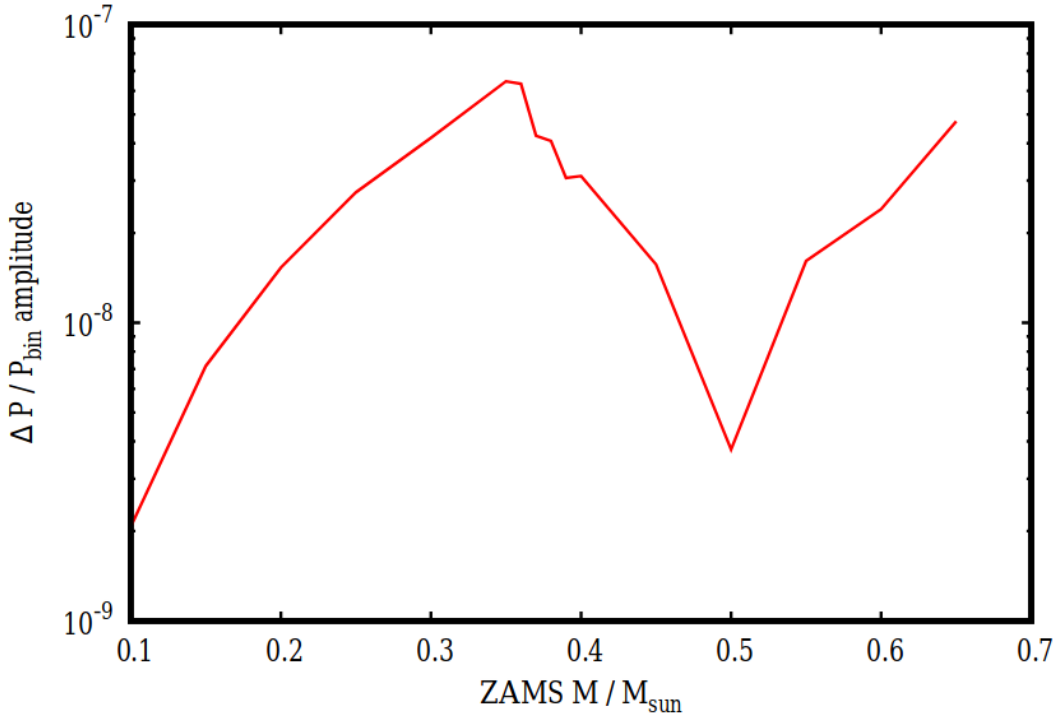

FIGURE 2.4: Period variation amplitude as a function of secondary stellar mass. The peak coincides with the transition from partially- to fully-convective stars. Figure from Völschow et al. (2018)

The authors also considered superposition of angular momentum redistribution modes and applied the model to a sample of stars with different masses.

A change in the quadrupole moment ΔQ is related to a variation of the quadrupole moment potential $\Delta\Phi_{12}$ via

$$\Delta Q = -\frac{R^3 \Delta\Phi_{12}(r)}{3G}. \tag{2.49}$$

Furthermore, $\Delta\Phi_{12}$ depends upon the radial eigenfunctions (see Völschow et al., 2018). The model was presented with special focus on the system HR1099, for which they found that if the observed period variations are energetically and mechanically feasible the expected activity cycle would be 70 yr. This contrasts significantly with the magnetic activity period of 14.8 years found by Perdelwitz et al. (2018).

However, an important result is presented in one of their figures and is shown here as Figure 2.4. By assuming typical PCEB parameters, namely $a_{\rm bin} = 1R_\odot$ and $M_{\rm white\,dwarf} = 0.5M_\odot$, magnetic and velocity fields fluctuations of the order of 10%, and with secondary masses between 0.1 $M_\odot$ and 0.7 $M_\odot$, the authors found a peak of $\Delta P/P$ as a function of mass right at the transition from partially- to fully-convective stars (i.e. at 0.35 $M_\odot$). This is attributed to the fact that when the radiative zone appears, the convective zone bottom boundary is pushed towards the radial direction, so the mass and angular momentum redistribution process zones are reduced as they are constrained to the convective region (Völschow et al., 2018). This

peak is of the order of $\sim 6 \times 10^{-8}$ and is lower than the values from observations ($10^{-7} - 10^{-6}$).

Still, the chosen values of the fluctuations are somewhat conservative just like the magnetic field strength. The authors close their study by saying that PCEBs with the aforementioned parameters are the ideal Applegate candidates, but further studies are needed to draw stronger conclusions.

Chapter 3

Codes

The thesis work presented here consists of two parts. The first uses the MESA CODE, and the second uses the PENCIL CODE. Here I will briefly introduce the two of them, also explaining the setup I worked with.

3.1 MESA code

The MESA CODE[1] (Paxton et al., 2011) is an open source 1D stellar evolution code parallelized with OpenMP. It implements the stellar structure and evolution equations. It is highly modular with a wide range of applications. In particular, the MESA STAR module solves the fully coupled structure and composition equations simultaneously. With this module one can follow the evolution of a single star throughout the evolutionary track.

Among the particularities of the MESA CODE is that it includes PGSTAR, a program for visualizing plots on the fly. For example one can follow the evolutionary path of the star while the code is running without having to manually make the plot. One can also visualize radial profiles with this tool.

3.1.1 Files in the simulation directory

The files *star_job* and *controls* are the ones that control the simulation. The first one is to specify parameters like stopping conditions, nuclear reactions, etc. The latter controls the physical parameters such as the ones needed to implement the mixing length theory, rotation, equation of state, etc.

[1] http://mesa.sourceforge.net/

3.1.2 The Equations

MESA solves the stellar structure equations, namely the momentum equation, mass conservation, energy conservation, and energy conservation, which respectively are

$$\frac{dP}{dr} = -\frac{GM\rho}{r^2}, \tag{3.1}$$
$$\frac{dM}{dr} = 4\pi r^2 \rho, \tag{3.2}$$
$$\frac{dL}{dr} = 4\pi r^2 \rho \varepsilon, \tag{3.3}$$
$$\frac{dT}{dr} = -\frac{3\kappa\rho L_r}{64\pi\sigma r^2 T^3}, \tag{3.4}$$

where P is pressure, r is the radius, G is the gravitational constant, ρ is the density, M is the mass, L is the luminosity, $\varepsilon = \varepsilon(\rho, T, \mu)$ is the nuclear energy generation rate (with μ the molecular weight), T is the temperature, $\kappa = \kappa(\rho, T, \mu)$ is the opacity, and σ is the Stefan-Bolzmann constant. Equation (3.4) is only appropriate where there is radiative energy transport. For convection, this equation is replaced by

$$\frac{dT}{dr} = \left(1 - \frac{1}{\gamma}\right)\frac{T}{P}\frac{dP}{dr}, \tag{3.5}$$

where $\gamma = c_p/c_v$ is the adiabatic index. An equation of state must also be specified, adding a fifth equation. Finally, a nuclear reaction network must also be provided. The mixing length theory of convection is used to treat convection.

3.1.3 The setup

In the work Navarrete et al. (2018) we have started with the *very low mass* test-suite. We used the proton-proton reaction chain, changed the rotation parameter implemented as the fraction between stellar to critical rotation velocities, and adjusted the mass.

3.2 Pencil Code

The PENCIL CODE[2] (Brandenburg and Dobler, 2002; Brandenburg, 2003) is a finite-difference code written in Fortran 95. It implements a sixth-order spatial derivative and third-order Runge-Kutta time integrator scheme, which makes the code particularly useful for studying weakly compressible turbulent flows. The PENCIL CODE is highly modular, including self-gravity, chemical reactions, magnetic fields, etc., which can be easily switched on or off depending on the physical problem of interest. The *Message passing interface* (MPI) is used to implement parallelization.

[2] http://pencil-code.nordita.org/

The first and second derivatives of a field f can be written, in a centered finite difference of 6th order, as

$$f_i' = \frac{1}{60\,\delta x}\left(-f_{i-3} + 9f_{i-2} - 45f_{i-1} + 45f_{i+1} - 9f_{i+2} + f_{i+3}\right),$$
$$f_i'' = \frac{1}{180\,\delta x^2}\left(2f_{i-3} - 27f_{i-2} + 270f_{i-1} - 490f_i + 270f_{i+1} - 27f_{i+2} + 2f_{i+3}\right).$$

For the timestepping, a high-order scheme is implemented in order to reduce amplitude errors and to allow longer time steps. This time step is a Runge-Kutta scheme (Williamson, 1980) named *RK-2N*, where the "2N" stands its memory consumption of two chunks.

The time step is specified by the *Courant time step* given as

$$\delta t = \min\left(c_{\delta t}\frac{\delta x_{\min}}{U_{\max}}, c_{\delta t,v}\frac{\delta x_{\min}^2}{D_{\max}}, c_{\delta t,s}\frac{1}{H_{\max}}\right), \tag{3.6}$$

where

$$\delta x_{\min} = \min(\delta x, \delta y, \delta z), \tag{3.7}$$
$$U_{\max} = \max\left(|\boldsymbol{u}| + \sqrt{c_s^2 + v_A^2}\right), \tag{3.8}$$
$$D_{\max} = \max(\nu, \gamma\chi, \eta, D), \tag{3.9}$$
$$H_{\max} = \max\left(\frac{2\nu S^2 + \zeta_{\text{shock}}(\nabla\cdot\boldsymbol{u})^2 + \ldots}{c_v T}\right), \tag{3.10}$$

where $\boldsymbol{u}$ is the velocity of the flow, c_s and v_A are the sound and Alfvén speeds, ν is the kinematic viscosity, χ the thermal diffusivity, γ the adiabatic index, η the magnetic diffusivity, D the passive scalar diffusivity, $\boldsymbol{S}$ is the rate of strain tensor (defined in Equation 3.18), and ζ_{shock} is the shock viscosity.

3.2.1 Modularity

All run directories contain the file "$RUN_DIR/src/Makefile.local" where modules are to be chosen. For example

```
MPICOMM    =  mpicomm

HYDRO      =  hydro
DENSITY    =  density
ENTROPY    =  entropy
MAGNETIC   =  magnetic
RADIATION  =  noradiation

EOS        =  eos_idealgas
GRAVITY    =  gravity_simple
```

The first line tells the code that we are going to use MPI communication. The 2nd to 6th lines specify that we are going to use the modules of hydrodynamics, density, entropy, magnetic fields, and no radiation, while the 7th and 8th lines say we are applying an ideal gas equation of state and simple gravity modules. This file is to be processed by *make*.

3.2.2 Files in the simulation directory

Initial and boundary conditions are set in the file *start.in*. In *run.in* the runtime parameters are set, like timestepping and file-storing conditions.

To check how the evolution of the simulation is going one can edit the file *print.in* and add, for example, the lines *it*, *t*, *brms*, and *urms*. This will print the quantities timestep number, time unit, rms magnetic field and velocity, respectively, every *it1* timesteps (which is specified in *run.in*).

Both are Fortran *namelists*.

3.2.3 Snapshots, slices, and averages

A *snapshot* refers to a file, called *var.dat* in the case of the *current snapshot* or *VARN* for a *permanent snapshot*, containing all the physical quantities necessary to restart a simulation. In *run.in* the parameter *isav* specifies the number of time units between the writing of the first, while *dsnap* controls the frequency of the latter.

Slice files (or video files) contain a series of values in a given plane. For example one might be interested in studying the magnetic field evolution at the star surface. In order to do so, the parameter *dvid* needs to be set to control the storing frequency (in code time units) of the slice. *slice_position* determines the position where the slice is taken, e.g. the combination of *slice_position* = 's' together with *xtop_slice* $= 0.98$ and *ytop_slice* $= 1.57$ will tell the code to take the slices in the surface of a sphere located at $r = 0.98R$, where R is the radius of the star.

Averages can be one or two dimensional, and can be taken on the x, y, and z directions, or all three planes. The quantities for which the averages are to be taken are specified in e.g. *yzaver.in*. In this case the quantities are averaged over the y and z directions and it will depend on the remaining one, this case being x.

3.2.4 The Model

The model we used in Chapter 5 is the same as in Käpylä et al. (2013) and is reproduced here for completeness. The computational domain is spherical but without the poles, which allows to reach higher spatial resolutions but at the cost of omitting connecting flows across the poles and introducing artificial boundaries at both poles. The domain (r, θ, ϕ) denotes radial, colatitude, and longitude directions. The radius extends from 0.7 R to 1.0 R, θ goes from $\pi/12$ to $11\pi/12$, and ϕ from 0 to 2π. The compressible magneto-hydrodynamic equations are solved in this domain, i.e.

$$\frac{\partial \boldsymbol{A}}{\partial t} = \boldsymbol{u} \times \boldsymbol{B} - \mu_0 \eta \boldsymbol{J}, \tag{3.11}$$

$$\frac{D \ln \rho}{Dt} = -\nabla \cdot \boldsymbol{u}, \tag{3.12}$$

$$\frac{D\boldsymbol{u}}{Dt} = \boldsymbol{g} - 2\boldsymbol{\Omega}_0 \times \boldsymbol{u} + \frac{1}{\rho}\left(\boldsymbol{J} \times \boldsymbol{B} - \nabla p + \nabla \cdot 2\nu\rho\boldsymbol{S}\right), \tag{3.13}$$

$$T\frac{Ds}{Dt} = \frac{1}{\rho}\left\{-\nabla \cdot \left(\boldsymbol{F}^{\mathrm{rad}} + \boldsymbol{F}^{\mathrm{SGS}}\right) + \mu_0 \eta \boldsymbol{J}^2\right\} + 2\nu \boldsymbol{S}^2. \tag{3.14}$$

Here, $\boldsymbol{A}$ is the magnetic vector potential, $\boldsymbol{u}$ and $\boldsymbol{B} = \nabla \times \boldsymbol{A}$ are the velocity and magnetic field, $\boldsymbol{J} = \mu_0^{-1} \nabla \times \boldsymbol{B}$ is the current density with μ_0 being the vacuum permeability. $D/Dt = \partial/\partial t + \boldsymbol{u} \cdot \nabla$ is the convective derivative, ρ is the density, ν is the kinematic viscosity, η is the magnetic diffusivity,

$$\boldsymbol{F}^{\mathrm{rad}} = -K \nabla T, \tag{3.15}$$

and

$$\boldsymbol{F}^{\mathrm{SGS}} = -\chi_{\mathrm{SGS}} \rho T \nabla s, \tag{3.16}$$

are the radiative and subgrid scale (SGS) fluxes. The first accounts for the flux coming from the radiative core and the latter is added to stabilize the scheme and to reduce the radiative background flux. K and χ_{SGS} are the radiative and turbulent head conductivities. The last one represents the unresolved convective transport of heat. s is the specific entropy, p is the pressure, and T is temperature. Furthermore, the system of equations 3.11 - 3.14 is closed by assuming an ideal gas law,

$$p = (\gamma - 1)\rho e, \tag{3.17}$$

where $\gamma = c_P/c_V = 5/3$ is the ratio of specific heats at constant pressure and volume, and $e = c_V T$ is the specific internal energy. $\mathbf{S}$ is the rate of strain tensor and is given by

$$S_{ij} = \frac{1}{2}(u_{i;j} + u_{j,i}) - \frac{1}{3}\delta_{ij} \nabla \cdot \mathbf{u}, \tag{3.18}$$

where semicolons denote covariant differentiation. $\mathbf{g} = -GM\hat{r}/r^2$ is the gravitational acceleration where G is the gravitational constant, M is the stellar mass, and $\hat{r}$ is the radial unit vector. The stellar rotation vector is given by $\boldsymbol{\Omega}_0 = (\cos\theta, -\sin\theta, 0)\Omega_0$. Note that the centrifugal force as been omitted in the Navier-Stokes equations (3.13) because the increased luminosity in the model increases the centrifugal force, which is of the same order as gravity, thus significantly altering the hydrostatic balance (Käpylä et al., 2013).

3.2.5 Initial and Boundary Conditions

The initial state is isentropic with a temperature gradient given by

$$\frac{\partial T}{\partial r} = -\frac{GM/r^2}{c_V(\gamma-1)(n_{\rm ad}+1)}, \tag{3.19}$$

where the polytropic index is

$$n = 2.5\left(\frac{r}{r_0}\right)^{-15} - 1, \tag{3.20}$$

and takes the values of $n = n_{\rm ad} = 1.5$ at the bottom and -1 at the top. This choice is made to ensure that the energy flux at the bottom is the only responsible for supplying energy to the system.

The fixed values that define a simulation are (i) the energy flux at the bottom,

$$F_b = -K\left(\frac{\partial T}{\partial r}\right)\Big|_{r=r_0}, \tag{3.21}$$

where $K = (n+1)K_0$ is the radiative conductivity and K_0 a constant (Käpylä et al., 2013), (ii) the angular velocity Ω_0, (iii) viscosity ν, (iv) magnetic diffusivity η. and (v) turbulent heat conductivity $\chi_{\rm SGS}$.

The velocity and magnetic fields are initialized with a small-scale low amplitude Gaussian noise.

Radial boundary

The radial boundaries are assumed to be impenetrable and stress-free for both boundaries, i.e at $r = r_0,\ R$:

$$u_r = 0, \tag{3.22}$$

$$\frac{\partial u_\theta}{\partial r} = \frac{u_\theta}{r}, \tag{3.23}$$

$$\frac{\partial u_\phi}{\partial r} = \frac{u_\phi}{r}. \tag{3.24}$$

The bottom $(r = r_0 = 0.7R)$ is assumed to be a perfect conductor

$$\frac{\partial A_r}{\partial r} = A_\theta = A_\phi = 0, \tag{3.25}$$

and at the top $(r = R)$ the magnetic field only has a radial component

$$A_r = 0, \tag{3.26}$$

$$\frac{\partial A_\theta}{\partial r} = -\frac{A_\theta}{r}, \tag{3.27}$$

$$\frac{\partial A_\phi}{\partial r} = -\frac{A_\phi}{r}. \tag{3.28}$$

The value of $\partial T/\partial r$ is fixed at the bottom and the upper radial boundary has a black body condition

$$\sigma T^4 = -K\nabla_r T - \chi_{\rm SGS}\rho T\nabla_r s, \tag{3.29}$$

where σ is a modified value of the Stefan-Bolzmann constant (see Käpylä et al., 2013).

Latitudinal boundary

The latitudinal boundary is also assumed to be stress-free at $\theta = 15°, 165°$

$$\frac{\partial u_r}{\partial \theta} = u_\theta = 0, \tag{3.30}$$

$$\frac{\partial u_\phi}{\partial \theta} = u_\phi \cot\theta, \tag{3.31}$$

and a perfect conductor

$$A_r = \frac{\partial A_\theta}{\partial \theta} = A_\phi = 0. \tag{3.32}$$

Density and entropy are assumed to have zero first derivative on both boundaries, thus suppressing heat fluxes through them.

3.2.6 Re-scaling of Q_{xx}

We have to rescale the density fluctuations in the simulations. This is because simulations of stellar magneto-convection with a fully compressible formulation have an increased luminosity to ensure the Mach number [defined in the RHS of Equation(3.37)] is lower than unity, particularly important when the density stratification is strong (Käpylä et al., 2013). Realistic energy fluxes are not possible because this would imply extremely short timesteps. So the energetic flux coming from the bottom is much higher than in the Sun. The ratio of fluxes $\mathfrak{F}_r$ is

$$\mathfrak{F}_r = \frac{\mathfrak{F}_{\rm simulation}}{\mathfrak{F}_\odot} = 807430. \tag{3.33}$$

A variation in pressure can be written as

$$\Delta p = \left(\frac{\partial p}{\partial \rho}\right)_s \Delta\rho, \tag{3.34}$$

where the subindex s indicates constant entropy. The above derivative equals the square of the sound speed c_s. Also, variations in pressure scale as

$$\Delta p \sim \rho \boldsymbol{u}^2, \tag{3.35}$$

where $\boldsymbol{u}$ is the velocity vector. Then,

$$\Delta p = c_s^2 \Delta\rho. \tag{3.36}$$

We can thus rewrite the variation in density $\rho' = \frac{1}{\rho}\Delta\rho$ as

$$\rho' \sim \frac{\boldsymbol{u}^2}{c_s^2} = \mathrm{Ma}^2. \tag{3.37}$$

Here Ma is the Mach number, which scales as

$$\mathrm{Ma} \sim \mathfrak{F}_{\mathrm{r}}^{1/3}, \tag{3.38}$$

thus,

$$\rho' \sim \mathfrak{F}_r^{2/3}. \tag{3.39}$$

All of the numbers given in Sections 5.2.4 and 5.3.4 are presented by doing this rescaling, which is a factor of $807430^{2/3} = 8671$, i.e.

$$Q_{xx} = \frac{1}{8671} Q_{xx,\mathrm{sim}}, \tag{3.40}$$

where the subindex 'sim' denotes the crude quadrupole moment obtained in the simulations.

Chapter 4

Applegate mechanism in post-common-envelope binaries: Investigating the role of rotation

In this chapter we first use the Modules for Experiments in Stellar Astrophysics (MESA) code to simulate the MS star for a sample of PCEBs. The simulations include rotation. A simple analytical dynamo model is then applied, which relates activity cycle to rotation period. This, together with the Applegate model provided by Völschow et al. (2016) and implemented in the publicly available Applegate Calculator[1]*, makes us conclude that the PCEBs with higher rotation-to-critical-rotation ratio are the most likely to have their O-C diagram shape explained via the Applegate mechanism.*

This work led to the publication of the paper Navarrete et al. (2018).

4.1 Simulations and Calculations

We use the MESA code (Paxton et al., 2011) to simulate the secondary star for every system under consideration (see table 4.1)

In particular, we use the module MESA star, which is a one dimensional stellar evolution code to evolve a single star. Three main input parameters are of interest for our simulations

1. Stellar mass. It is kept constant during the run, and equal to the mass of the convective star in each system.

2. Rotation. Set as the fraction $\Omega_{\rm ZAMS}/\Omega_{\rm crit}$, where $\Omega_{\rm crit} = \sqrt{GM/R^3}$ is the critical angular velocity. If this limit is exceeded, then the star can no longer sustain hydrostatic equilibrium. $\Omega_{\rm ZAMS}$ is the angular velocity of the star at the zero age main sequence. This ratio is kept fixed during the run.

3. Maximum age. The simulation is stopped when the star reaches its corresponding derived age.

[1] http://theory-starformation-group.cl/applegate/index.php

TABLE 4.1: Main stellar parameters together with the relative rotation of the secondary star. Different radii R_d are calculated for different γ in Eq. 4.1 for which the rotation period $P_{\rm rot}$ is equal to the calculated activity period $P_{\rm cycle}$. The value $\gamma = 0.86$ is that found for the Sun. Source: own work (Navarrete et al., 2018).

System	$M_{\rm sec}/M_\odot$	$R_{\rm sec}/R_\odot$	$\Omega/\Omega_{\rm crit}$	R_d/R		
				$\gamma = 0.7$	$\gamma = 0.86$	$\gamma = 1.0$
RX J2130.6+4710	0.555	0.534	0.116	0.67	0.86	0.92
HS 0705+6700	0.134	0.186	0.265	0.87	0.95	0.97
HW Vir	0.142	0.175	0.192	0.60	0.89	0.95
NN Ser	0.111	0.149	0.154	0.81	0.96	0.97
NSVS 14256825	0.109	0.162	0.208	0.88	0.94	0.98
NY Vir	0.15	0.14	0.155	0.88	0.96	0.98
HU Aqr	0.18	0.22	0.324	0.79	0.93	0.96
QS Vir	0.43	0.42	0.318	0.80	0.92	0.96
RR Cae	0.183	0.209	0.085	0.80	0.92	0.96
UZ For	0.14	0.177	0.262	0.82	0.94	0.97
DP Leo	0.1	0.134	0.288	0.78	0.93	0.97
V471 Tau	0.93	0.96	0.216	-	0.78	0.87

For every run we choose the 'ML1' mixing length implementation, with the free parameter $\alpha_{\rm MLT} = 1.5$ and a basic reaction network. Metallicity is chosen to be equal to the Solar metallicity. For stars with masses lower than 0.14 $M_\odot$ the 'very low mass' test-suite available in MESA is used as a guide to properly evolve them. In the remaining of this chapter, all derived quantities described are obtained from the last written MESA profile which corresponds to the age of the binary.

4.2 Analytical dynamo models

The MESA models are used as input for the stellar structure to explore the expectations based on simple dynamo models. We use here a similar approach to that of Schleicher and Mennickent (2017) and Perdelwitz et al. (2017).

The relation between magnetic activity cycle $P_{\rm cycle}$ and rotation period $P_{\rm rot}$ is given by (Soon, Baliunas, and Zhang, 1993; Baliunas et al., 1996)

$$P_{\rm cycle} = D^\gamma P_{\rm rot}\,, \tag{4.1}$$

where D is the dynamo number, and γ is a parameter that depends upon the activity level of the star (Dubé and Charbonneau, 2013). As PCEBs are close binaries, we can safely assume the secondary to be tidally locked (Zahn, 1989; Zahn and Bouchet, 1989) meaning that $P_{\rm rot}$ is equal to the binary period. D is further related to the Rossby number Ro via $D = {\rm Ro}^{-2}$, where Ro is refined as the ratio between the rotation period and the convective turnover time ${\rm Ro} = P_{\rm rot}/\tau_c$. Following (Soker, 2000), we can calculate Ro as

$$\mathrm{Ro} = 9 \left(\frac{v_c}{10\,\mathrm{km/s}} \right) \left(\frac{H_p}{40\,R_\odot} \right)^{-1} \left(\frac{\omega}{0.1\,\omega_{\mathrm{Kep}}} \right)^{-1} \left(\frac{P_{\mathrm{Kep}}}{\mathrm{yr}} \right), \tag{4.2}$$

where v_c is the convective velocity, H_p is the pressure scale height, ω and ω_{Kep} are the angular and keplerian angular velocity, respectively. Finally, P_{Kep} is the Keplerian orbital period. The convective velocity and pressure scale height can be obtained from the MESA simulations.

To obtain the expected cycle period with equation 4.1 we must first calculate Ro to then get D. We also need to obtain a value for γ. To do the latter, we run a simulation for the Sun. Then use the relevant stellar parameters at $r = 0.7R_\odot$, as the solar dynamo is expected to be relevant at this position, together with the fact that the magnetic cycle is equal to 22 year. With this, we obtain $\gamma = 0.86$. The Sun is a slow rotator, with a rotation period at the equator of 24.5 days, and it has a weak magnetic field of about ~ 1 G. On the other hand, even single M dwarfs (dM) have rotation periods of less than ten days (Somers et al., 2017), and in PCEBs their rotation periods are less than three hours, with field strengths on the order of a few kG (Johns-Krull and Valenti, 1996). This means that the actual value of γ may be different for the case of dM in PCEBs. For this reason we also explore $\gamma = 0.7$ and $\gamma = 1.0$ (see table 4.1). For a given value of γ, it is then possible to calculate the fraction of the stellar radius R_d/R where the predicted activity period is equal to the observed one.

4.3 The Applegate mechanism

Given an idea of the radius where the dynamo operates inside the star, it is also important to find out whether it is energetically feasible to produce the observed eclipsing time variations via magnetic activity. In this section I will briefly introduce the formalism we employ. The reader is referred to Völschow et al. (2016) and to the Applegate calculator[2]. The latter allows us to calculate the required energy ΔE as a fraction of the available energy in the magnetically active star, E_{sec}, to drive the corresponding change of the quadrupole moment. The equation is given as

$$\frac{\Delta E}{E_{sec}} = k_1 \frac{M_{\mathrm{sec}} R_{\mathrm{sec}}^2}{P_{\mathrm{bin}}^2 P_{\mathrm{mod}} L_{\mathrm{sec}}} \left(1 \pm \sqrt{1 - k_2 G \frac{a_{\mathrm{bin}}^2 M_{\mathrm{sec}} P_{\mathrm{bin}}^2}{R_{\mathrm{sec}}^5} \frac{\Delta P}{P_{\mathrm{bin}}}} \right)^2, \tag{4.3}$$

where P_{bin}, a_{bin}, and $\Delta P/P_{\mathrm{bin}}$ are the orbital period, semi-major axis, and observed relative change of the orbital period during one cycle of the binary, respectively; P_{mod} is the observed modulation period of the binary; M_{sec}, R_{sec}, L_{sec}, T_{sec} are the mass, radius, luminosity, and temperature of the magnetically active star, respectively. The

[2] http://theory-starformation-group.cl/applegate/

k_1 and k_2 parameters are defined as

$$k_1 = \frac{4\pi^2}{5} \frac{\lambda(\gamma+1)(\xi^3 - \xi^{-2})}{1+\lambda(\xi^3-1)} \frac{(f-\gamma)^2}{(\gamma^2/\lambda + f)^2}, \tag{4.4}$$

$$k_2 = \frac{15}{36\pi^2} \frac{\xi^5}{\lambda} \frac{(\gamma/\lambda + f)}{(f-\gamma)^2}. \tag{4.5}$$

Both k_1 and k_2 depend on the stellar structure, particularly on the density. The first one regulates the overall magnitude of the required energy to drive quasi-periodic period variations. The latter affects the separation between low- and high-energy solutions for the Applegate mechanism. Two mean densities enter the calculation of k_1 and k_2: $\rho_{\rm in}$ from the bottom of the star to R_d, and $\rho_{\rm out}$ from R_d to the radius of the star $R_{\rm star}$. The model assumes interchange of angular momentum between these two zones. The additional parameters are defined as $\lambda = \rho_{\rm out}/\rho_{\rm in}$ and $\xi = R_{\rm star}/R_d$.

An important parameter is $r/R_{\rm core}$, which is the radial position that separates the core and shell between which angular momentum is exchanged. As a first approach, we assumed that it corresponds to the scale where the dynamo model produces an activity cycle that corresponds to the observed period. We also discuss other choices and explore their implications. Note that k_1 and k_2 are explicitly evaluated based on the stellar profiles obtained from MESA. As also discussed by Lanza (2006), the angular velocity variations in the radiative core are confined to a thin layer, so its contribution to the changes on the quadrupole moment are negligible. So we have chosen to assume that the interchange of angular momentum is confined to the convective zone, thus neglecting any contribution of the radiative cores found in the secondaries of QS Vir and V471 Tau. The latter was taken into account when calculating the mean density in the core and thus in the resulting stellar structure parameters.

4.4 Results

In the following, I will present the results from our stellar structure calculations, focusing initially on the resulting timescales for the magnetic activity cycles, and subsequently assessing the implication for the feasibility of the Applegate mechanism.

4.4.1 Stellar structure and dynamo timescales

To illustrate the stellar structure calculations, Figure 4.1 shows the convection velocity and density profile for DP Leo as simulated with MESA. As we are considering rather rapidly rotating stars as a result of tidal locking, we have explored the impact of varying the rotational velocity of the star, which is shown in figure 4.1, but fund overall still moderate effects, with density changes of at most 20% even in strong rotating scenarios. Figure 4.2 shows the dynamo number D calculated as a function of radius for DP Leo based on equation 4.2 together with the relation $D = {\rm Ro}^{-2}$. Using

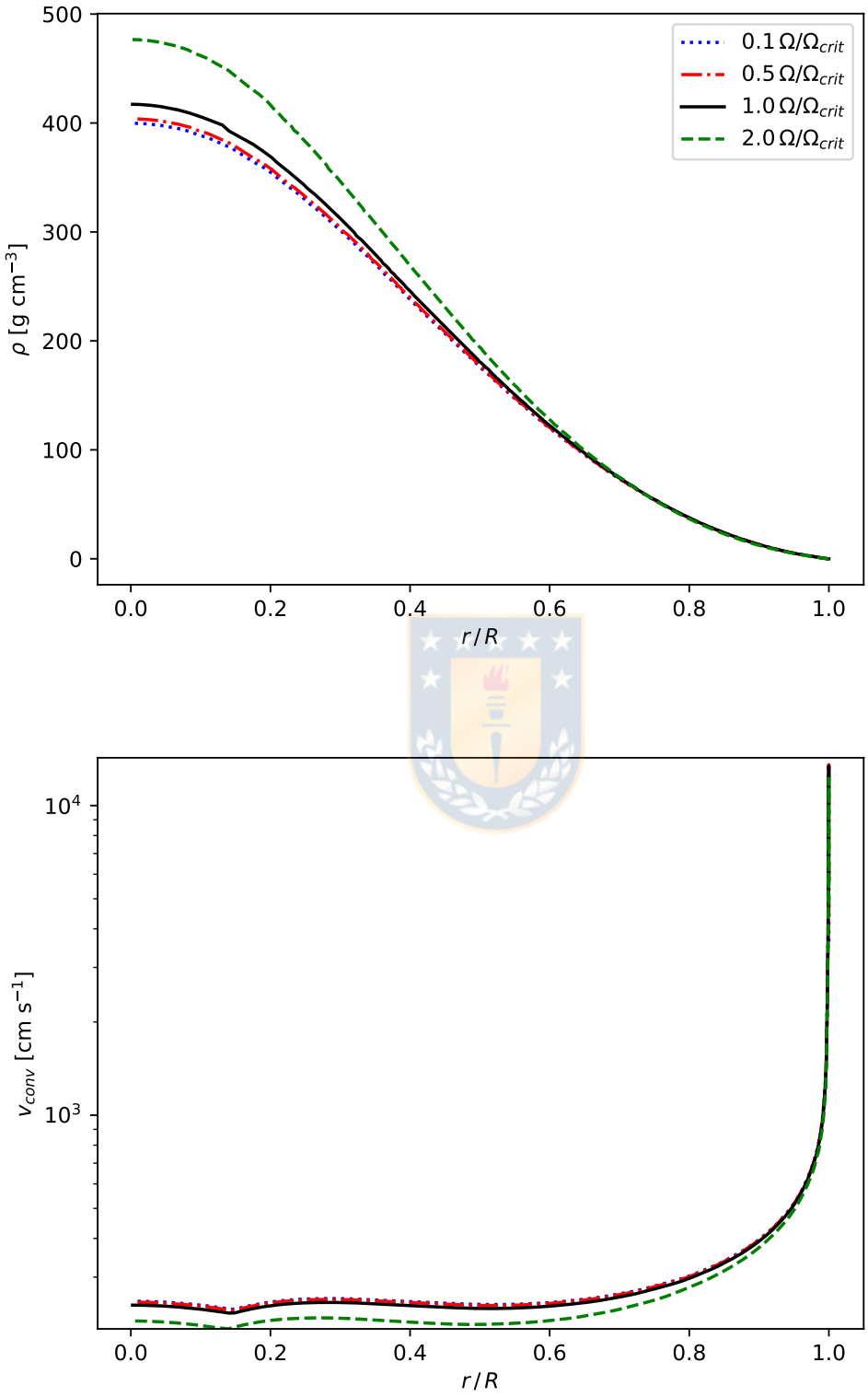

FIGURE 4.1: Density profile (top) and convection velocity profile (bottom) for DP Leo simulated by MESA for different rotation velocities. The ratio $1.0\,\Omega/\Omega_{\rm crit}$ corresponds to the observed one and is ~ 0.288 for DP Leo. Source: own work (Navarrete et al., 2018).

$\gamma = 0.86$ and $P_{\rm rot} = P_{\rm binary}$ we then calculate $P_{\rm cycle}$ using equation 4.1. Figure 4.2 also shows the normalized period as a function of the radius. The horizontal gray line corresponds to a ratio of one, and the intersection thus marks the point where the calculated activity period equals the observed modulation period. This intersection point provides a first estimate for the effective radius that produces the observed modulation period.

This same analysis was pursued for the 12 PCEBs provided in the sample by Völschow et al. (2016), and we summarize the obtained results together with the main parameters of the secondary star in table 4.1. In particular, we provide the calculated radii R_d/R for γ = 0.7, 0.86, and 1.0. Generally, we find a reduced ratio of R_d/R when lowering γ. Specifically, for γ = 0.86 they range between 0.78 and 0.97, and for γ = 1.0 the ratios range between 0.87 and 0.98. While the correct value of γ is not clear, we nevertheless note the general trend that the dynamo appears to be driven within the outer parts of the star, corresponding to a radius of at least 60% of the stellar radius. Only in the case of V471 Tau, we have to note that the observed activity cycle cannot be reproduced for γ = 0.7 or less, providing a stronger constraint on dynamo models for that system.

4.4.2 Feasibility of the Applegate mechanism

We now assess whether the Applegate mechanism in these systems is capable of driving the observed eclipsing time variations. For this purpose, the ratio of required to available energy is calculated using Eq. 4.3. The results of the calculation are summarized in table 4.2 for different scenarios. Note that the results in Table 4.2 are different from those reported in the Völschow et al. (2016) two zone model (their Table 4). While they determined the core radius based on radial density profiles obtained with Evolve ZAMS[3] that were rescaled to the stellar radius, we have employed here the radial profiles obtained via MESA star. More importantly, we varied the position that is considered as the separation point between the core and the shell, and we also explored the effect of choosing this position according to the radius where the modulation period is reproduced by our dynamo model. The Völschow et al. (2016) results are re-obtained by choosing the separation of the core and the shell to be at $r/R \sim 0.88$. To give an idea of the uncertainties in the energetics, we provide error bars on $\Delta E/E$ in the case of RX J2130.6+4710 in Table 4.2, which are evaluated adopting the upper and lower limits for secondary mass and radius, respectively. The latter shows that the values of $\Delta E/E$ should be taken as indicative, but come with uncertainties of about a factor of two. A more accurate determination of stellar parameters would certainly help to reduce these errors, though we caution the reader that intrinsic uncertainties are also present within the two-zone approximation of the model, and further theoretical developments will be necessary as well.

[3]http://www.astro.wisc.edu/ townsend/static.php?ref=ez-web

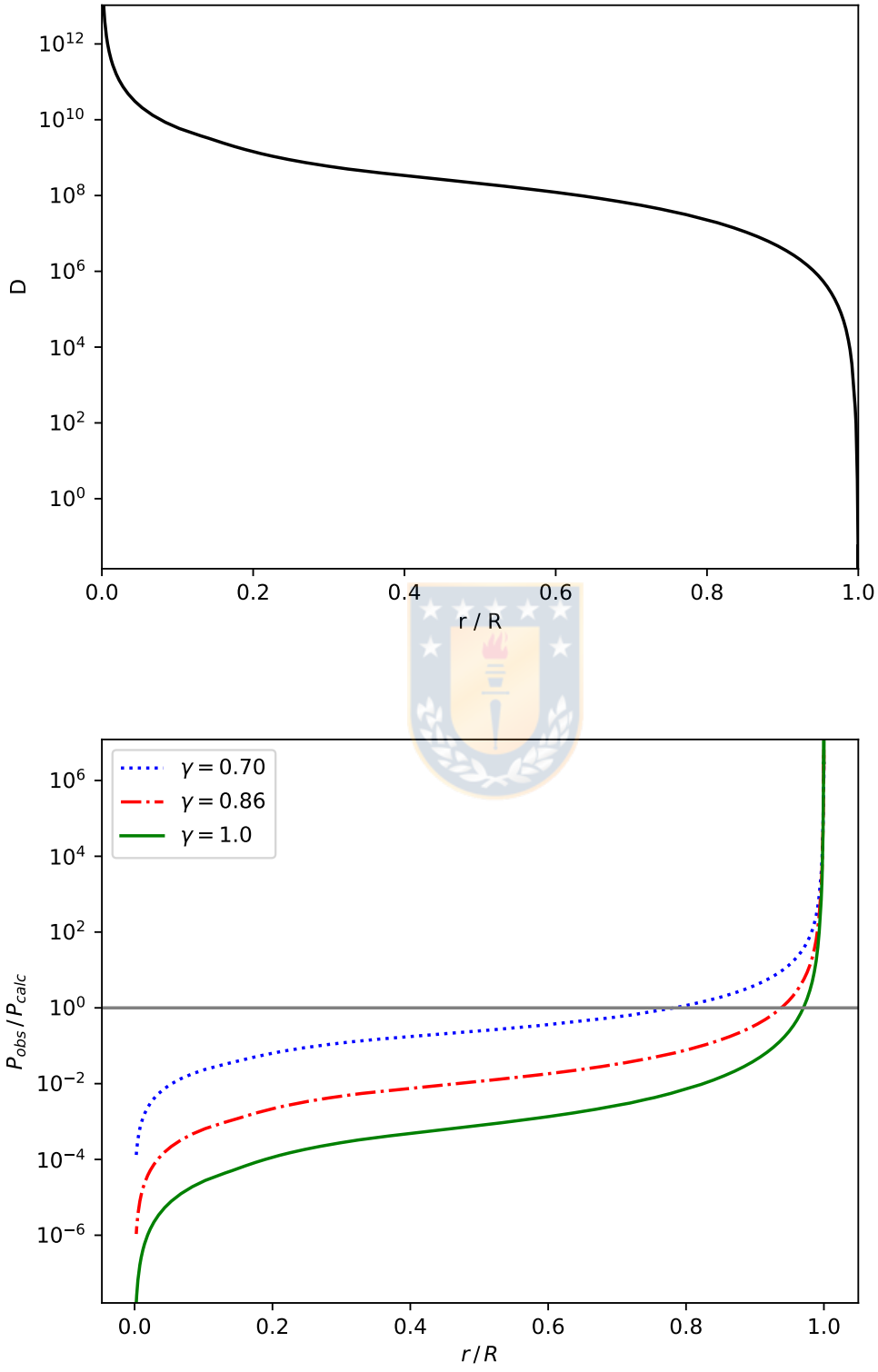

FIGURE 4.2: Dynamo number profile (top) and ratio of the observed vs. calculated activity cycle (bottom) for DP Leo calculated using Eq. 4.1. Source: own work (Navarrete et al., 2018).

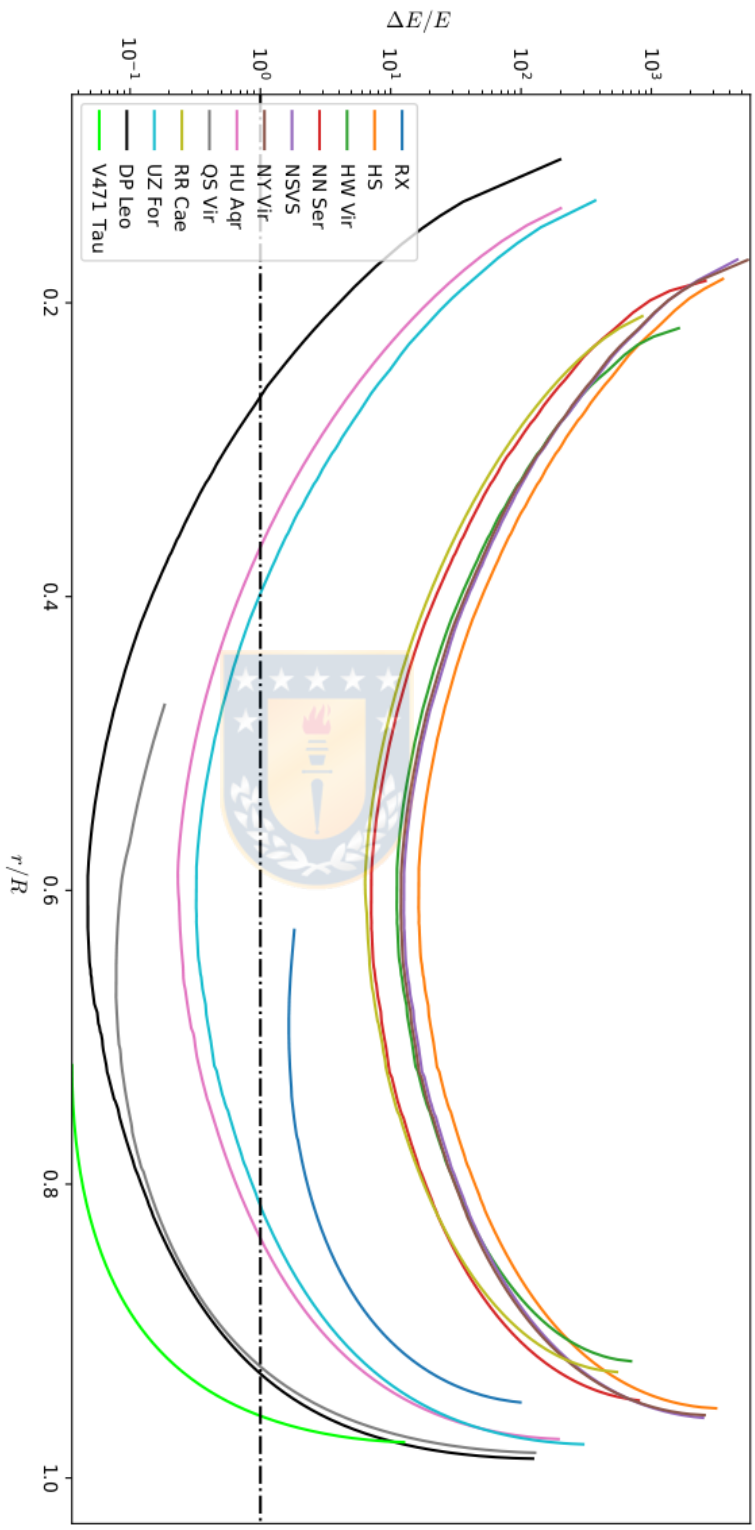

FIGURE 4.3: $\Delta E/E$ calculated for varying radii for all systems. Two groups can be identified: those that fell bellow $\Delta E/E = 1$ and those above it. At the borders the solutions for the Applegate energy become imaginary (see Völschow et al. (2016) for a discussion on this). Source: own work (Navarrete et al., 2018).

TABLE 4.2: Results for the energy required to drive the Applegate mechanism for all systems considered in this work. R_d/R denotes the core-shell transition radius. $\Delta E/E_{\rm sec}$ is the necessary energy to drive the change in the quadrupole moment to give raise to the observed period, as a fraction of the available energy, calculated considering different shells including the point at which the observed period matches the calculated, i.e., R_d/R. Results with $\Delta E/E_{\rm sec} < 1$ are highlighted in bold. RX J2130.6+4710 is presented with errors, as mentioned in section 4.4.2. Source: own work (Navarrete et al., 2018).

System	$\Delta E/E_{\rm sec}$			
	$R_d/R(\gamma = 0.86)$	$R_d/R = 0.85$	$R_d/R = 0.75$	$R_d/R = 0.65$
RX J2130.6+4710	$4.2^{-2.3}_{+7.6}$	$3.6^{-1.8}_{+5.4}$	$1.8^{-0.96}_{+2.5}$	$1.7^{-0.93}_{+2.3}$
HS 0705+6700	1354	56	22	93
HW Vir	93	43	15	16
NN Ser	-	24	9.5	6.7
NSVS 14256825	500.5	57	21	13
NY Vir	-	54	19	12
HU Aqr	6.3	**0.88**	**0.41**	**0.25**
QS Vir	**0.88**	**0.22**	**0.097**	**0.078**
RR Cae	237.3	34	11	6.8
UZ For	12	1.5	**0.56**	**0.34**
DP Leo	**0.98**	**0.21**	**0.081**	**0.049**
V471 Tau	**0.039**	**0.061**	**0.036**	-

Particularly in the case of RX J2130.6+4710, we note that $\Delta E/E$ may still be less than one if the error are taken into account.

If we first focus on our reference case, this is $\gamma = 0.86$, and adopt the radius R_d as the radius that separates the shell from the core, we find that in three systems, namely QS Vir, DP Leo, and V471 Tau, the Applegate mechanism is energetically feasible; in two of them (QS Vir and DP Leo) though only marginally so. The system RX J2130.6+4710 in principle yields values $\Delta E/E > 1$. Considering the error bars, it may however be consistent still with the scenarios where Applegate is marginally feasible. We also note that, in case of RX J2130.64710, there is only a lower limit available for the modulation period, translating into an upper limit on $\Delta E/E$. As we noted above, it is not clear that the normalization to $\gamma = 0.86$ is appropriate for these type of systems, or if even a constant γ is justified, given the different types of secondary stars in the sample. We thus explore how the energetic feasibility of our results depends on the adopted ratio $R_{\rm core}/R$, exploring ratios of 0.85, 0.75, and 0.65, which lie within the plausible range determined in the previous subsection. In particular, we find that the required energy at least initially decreases when adopting a larger shell, only for some systems it starts increasing again at $R_{\rm core}/R = 0.65$. Exploring the results in this parameter space, we then find that in five systems, namely HU Aqr, QS Vir, UZ For, DP Leo and V471 Tau, the Applegate mechanism is potentially feasible, with ratios $\Delta E/E$ ranging from 0.036 to 0.98.

Figure 4.3 shows $\Delta E/E$ as a function of r/R. The curves end when there is no

longer a physically meaningful solution, that is, when the required change in the angular momentum violates angular momentum conservation within the star. For all systems, we see that the required energy fraction follows an approximately parabolic shape with a minimum near $R_{\rm core}/R \sim 0.6$. While all curves are of similar shape and share the same asymptotic behavior, the magnitude or normalization varies significantly, and the systems can be roughly divided into two groups. In particular, there is a first group of six systems with the minimum $\Delta E/E \sim 60 - 300$, where the Applegate mechanism is not feasible. Another group consists of the systems identified above, with minimum $\Delta E/E \sim 0.03 - 0.9$, where the mechanism becomes feasible. While the gap between these groups appears striking within the figure and corresponds to roughly two orders of magnitudes in $\Delta E/E$, we cannot entirely exclude in full that the latter is due to the relatively small number of systems in our sample.

While RX J2130-6+4710 appears to lie somewhat in between the gap, though towards the lower end, it is important to note that the values of $\Delta E/E$ here represent only an upper limit, and better constraints on the modulation period will be necessary to evaluate whether the systems lies within the gap, or if it is part of the lower group. Now, within the error bars, the system is now already consistent with potentially driving the Applegate mechanism.

In order to determine if there is a physical origin of the bimodality that is indicated in the plot, we examine whether the minimum value of $\Delta E/E$ depends critically on relevant physical parameters of the system. Let us introduce the parameters

$$\alpha = k_1 \frac{M_{\rm sec} R_{\rm sec}^2}{P_{\rm bin}^2 P_{\rm mod} L_{\rm sec}} \tag{4.6}$$

and

$$\beta = k_2 G \frac{a_{\rm bin}^2 M_{\rm sec} P_{\rm bin}^2}{R_{\rm sec}^5} \frac{\Delta P}{P_{\rm bin}}. \tag{4.7}$$

Figure 4.4 shows $\Delta E/E$ as a function of both parameters. While $\Delta E/E$ shows no correlation with α, it is clearly recognizable that the lowest values of $\Delta E/E$ can be found for the lowest values of β with a clear trend, with the remaining scatter being introduced by the dependence on α. The latter provides a first indication that β is most relevant in determining the feasibility of the Applegate mechanism.

While α shows no correlation with $\Delta E/E$, in Figure 4.5 one can see a clear dependence of $\Delta E/E$ on β, with the remaining scatter being due to the dependence on α. Consider the ratio of binary period vs critical period of the secondary star, where the critical period is defined through the break-up velocity when the star reaches critical rotation, i.e.

$$P_{\rm crit}^2 = 4\pi^2 \frac{R_{\rm star}^3}{G M_{\rm star}}, \tag{4.8}$$

thus

$$\left(\frac{P_{\rm binary}}{P_{\rm critic}}\right)^2 = \frac{M_{\rm sec}}{M_{\rm total}} \left(\frac{a_{\rm bin}}{R_{\rm sec}}\right)^3. \tag{4.9}$$

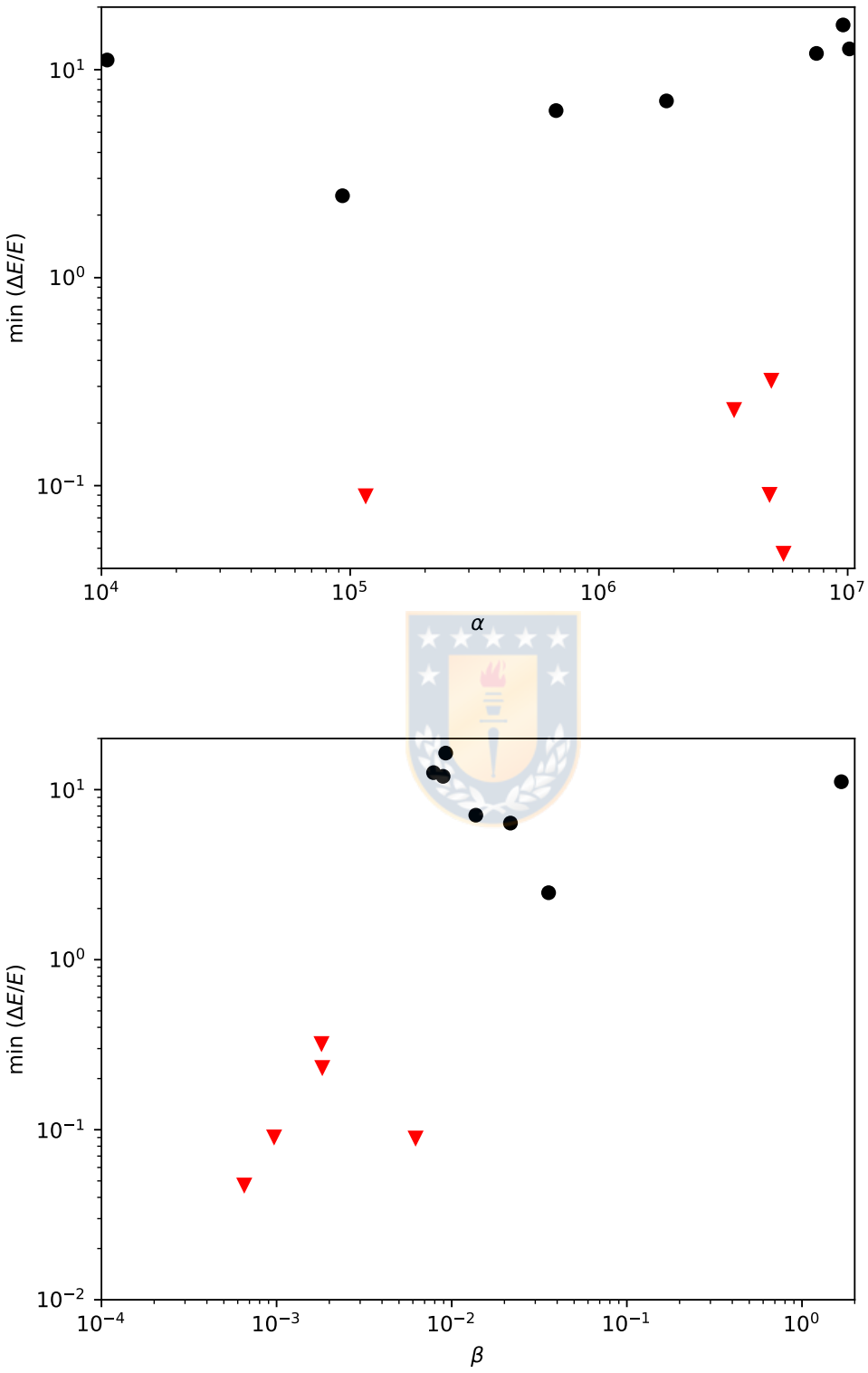

FIGURE 4.4: *Top*: Minimum value of $\Delta E/E$ as a function of the parameter α defined in Eq. 4.6. *Bottom*: Minimum value of $\Delta E/E$ as a function of β defined in Eq. 4.7. Red triangles represent the systems falling below the horizontal dashed line at Fig. 4.3. Source: own work (Navarrete et al., 2018)

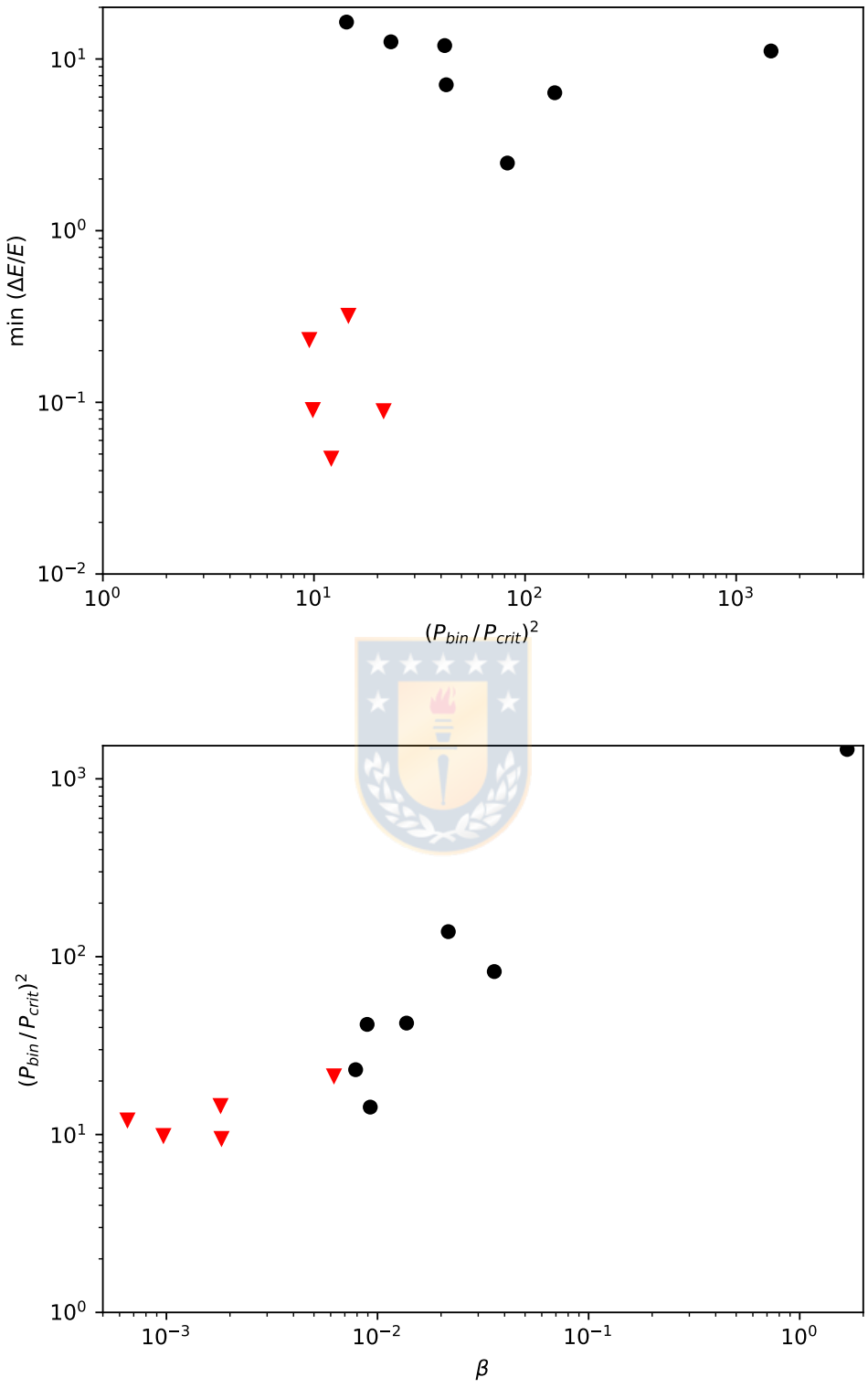

FIGURE 4.5: *Top*: Minimum value of $\Delta E/E$ against the squared fraction between the binary period $P_{\rm bin}$ and the critical period $P_{\rm crit}$ defined as the period the binary would have if the secondary is rotating at its critical rotation velocity under the assumption of tidal locking. *Bottom*: $(P_{\rm bin}/P_{\rm crit})^2$ plotted against β defined in Eq. 4.7; the rightmost circle corresponds to HW Vir. Red triangles are the systems falling below the horizontal dashed line at Fig. 4.3. Source: own work (Navarrete et al., 2018)

Under the assumption of tidal locking, which is highly plausible within these systems, this ratio thus describes the ratio of actual over critical rotation period of the secondary star. Figure 4.5 shows how minimum $\Delta E/E$ depends on this quantity. In this case, the correlation is less clear as the correlation with β, but low ratios of $P_{\rm binary}/P_{\rm critic}$ still yield the lowest ratios of $\Delta E/E$, thus implying that high rotation rates (relatives to breakup) are beneficial to drive the Applegate mechanism. In the same figure, we also explore whether the parameter β is correlated with Pbinary$/P_{\rm critic}$. Here we also find that low ratios of $P_{\rm binary}/P$critic imply low values of β, and vice versa. The latter strengthens our conclusion that rapid rotation may play a central role in the feasibility of the Applegate mechanism in PCEBs.

In fact, one can show that

$$\beta = k_2 \frac{4\pi^2 a_{\rm bin}^2}{R_{\rm sec}^2} \frac{P_{\rm bin}^2}{P_{\rm critic}^2} \frac{\Delta P}{P_{\rm bin}}, \tag{4.10}$$

suggesting a quadratic dependence on the ratio of rotation period over critical period. Furthermore, we note here that rapid rotation may frequently imply a short binary period and thus also a lower value of $a_{\rm bin}$, which strengthens this correlation further. The remaining parameter $R_{\rm sec}$ depends primarily on the mass of the secondary star, which is very similar in many of the PCEB systems (see Table 4.1), and only occasionally introduces scatter when the secondary star is more massive. Equation 4.10 can be rewritten using Eq. 4.9, leading to

$$\beta = k_2 4\pi^2 \left(\frac{P_{\rm bin}}{P_{\rm critic}}\right)^{10/3} \left(\frac{M_{\rm total}}{M_{\rm sec}}\right)^{2/3} \frac{\Delta P}{P_{\rm bin}}. \tag{4.11}$$

This last equation provides evidence of a stronger dependence on the ratio of the rotation period over critical period. It is then plausible overall that the main visible dependence is due to rotation.

4.5 Discussion of selected system

4.5.1 HW Vir

Consisting of a primary of 0.485 $M_\odot$ and a secondary of 0.142 $M_\odot$, this system was first proposed to have a two-planet system by Lee et al. (2009) that was later proven to be secularly unstable and replaced with another two-planet secularly-stable system by Beuermann et al. (2012b). We find rather high values of $\Delta E/E$ for this system (see Fig. 4.3), and thus HW Vir might be a good candidate to test the planetary hypothesis using direct imaging.

4.5.2 NN Ser

This system consists of a white dwarf with a M4 companion (Parsons et al., 2010). The planetary solutions that explain the eclipsing time variations were proven to be

dynamically stable (Beuermann, Dreizler, and Hessman, 2013). This, together with the recent detection of dust around NN Ser by Hardy et al. (2016) which was not expelled from the common envelope phase, add credibility to the planetary hypothesis. On the other hand, the most recent data require the subtraction of a quadratic term from the ephemeris to obtain the planet solution (Bours et al., 2016). Based on the calculations in this paper, we find that it is energetically difficult to explain the observed ETVs based on the Applegate effect ones, as there are no solutions with $\Delta E/E < 1$. However, there are solutions with $\Delta E/E \leqslant 10$, suggesting that relevant fluctuations of the ETV could be induced by the Applegate mechanism, even if it is not the entire signal.

4.5.3 HU Aqr

HU Aquarii is a system of particular interest. First discovered by Schwope, Thomas, and Beuermann (1993), it has a strongly magnetized primary white dwarf and a M4 secondary and it is constantly being monitored by several groups. Bours et al. (2014) concluded that a planetary model with up to three members cannot explain the observed ETVs as they are dynamically unstable over short periods of time. Goździewski et al. (2015) revisited the planetary hypothesis and concluded that it might be possible that a three-planet system is present. However, either one of these planets must have a retrograde orbit or they should have high mutual inclinations.

In the calculations presented here. HU Aqr was found to indeed have solutions that might trigger the Applegate mechanism, with $\Delta E/E \sim 0.3$. Such solutions require the dynamo to operate further in the interior of the star. The ratio of $\Delta E/E$ is reduced compared to the value reported by Völschow et al. (2016) due to the evaluation of the coefficients k_1 and k_2 from the stellar structure profiles.

4.5.4 QS Vir

Horner et al. (2013) performed a detailed dynamical study of the proposed planets for QS Vir. The authors performed more than 180 thousand simulations of the proposed planetary systems but found that none of them with long enough stability to explain the eclipsing time variations. More recently, Parsons et al. (2016) used high-resolution spectroscopy to study the magnetic activity of this PCEB and found that the M dwarf is covered with a large number of star spots, thus indicating that it is a very active star. We have found that the M dwarf on this system is among those with the highest relative rotation, where the Applegate mechanism appears to be feasible (see Table 4.2). The secondary dM star has a radiative core, which we assumed here not to contribute to the Applegate mechanism.

4.5.5 V471 Tau

It was predicted by Beavers, Lui, and Herczeg (1986) that a third body with a period of ∼25 yr could exist in this system. Recently, Hardy et al. (2015) used direct imaging to test the hypothesis, resulting in non-detection of the proposed brown dwarf. Later, Vaccaro et al. (2015) analyzed the system and proposed several ways for the third body to have avoided detection. However, Vanderbosch et al. (2017) studied the eclipsing time variations with two independent clocks, namely the orbital period of the binary and white dwarf spin period. They do not find the same magnitude of variation of the O–C of the spin period as for the diagram based on the binary period. The latter thus favors the Applegate mechanism as opposed to the presence of a third body.

As the secondary of V471 Tau is a Sun-like star with a mass of ∼0.93 $M_\odot$, it is expected to have an $\alpha\Omega$-dynamo operating on the radiative-convective inter-phase. As this star is rotating much faster than the Sun, one may expect that a strong magnetic field due to rapid rotation may trigger the Applegate mechanism, consistent with our findings.

4.5.6 NSVS 14256825

For the system NSVS 14256825, the cyclic behavior of the O–C residuals was previously attributed to the presence of one or two Jupiter-like planets (Beuermann et al., 2012a; Almeida, Jablonski, and Rodrigues, 2013; Wittenmyer, Horner, and Marshall, 2013), new data by Nasiroglu et al. (2017) revealed a systematic, quasi-sinusoidal variation deviating from the older ephemeris by about 100 s. As the most plausible explanation for this deviation, they propose a one-companion model to be the most reliable explanation and propose that the Applegate mechanism is not energetically feasible to drive the changes. We note here that while there are no solutions with $\Delta E/E < 1$ that could explain the eclipsing time variations entirely, there are solutions with $\Delta E/E \sim 10$, implying that magnetic activity could at least induce relevant scatter in the observed variations.

4.5.7 RX J2130.6+4710

This PCEB consists of a red dwarf with a mass of 0.555 $M_\odot$ and radius 0.534 $R_\odot$, and a white dwarf of mass 0.554 $M_\odot$ and radius 0.0137 $R_\odot$ with a separation of 2–3 $R_\odot$ (Maxted et al., 2004). The large O–C variations from a relatively long observational baseline were detected by Bours et al. (2016). They identified this system to have a lower limit for the period of the mechanism at work to be 30 yr and we adopted this limit for our calculation together with an eclipsing time variation of 250 s. This translates into $\Delta P/P = 1.6 \times 10^{-6}$. Considering the error bars, the system may be able to drive the Applegate mechanism. In addition, if the modulation period is greater, say 50 yr, then this would mean that $\Delta P/P \sim 9 \times 10^{-7}$ and the system will clearly fall bellow the line $\Delta E/E = 1$. As noted by Bours et al. (2016), the

observational baseline is yet too small to draw a more robust conclusion for this system and further eclipsing observations will be crucial.

4.6 Conclusions

In this paper we have explored whether the Applegate mechanism can drive the observed eclipsing time variations in a sample of 12 PCEB systems. For this purpose, we have obtained radial profiles of the secondaries using the MESA code (Paxton et al., 2011), and applied simple dynamo models following Soon, Baliunas, and Zhang (1993) and Baliunas et al. (1996) to determine the radius at which the expected activity cycle matches the observed modulation period. This radius was found to depend on the power exponent γ, but even for different choices of γ, we found that the dynamo can generally be expected to be driven in the outer layers, at radii $R_d/R \sim 0.6$.

We subsequently explored whether the Applegate mechanism to drive the eclipsing time variations is also energetically feasible, employing the framework presented by Völschow et al. (2016), which is now publicly available through the *Applegate Calculator*. Based on this analysis, we show that the Applegate mechanism may be energetically feasible in up to five systems, HU Aqr, QS Vir, UZ For, DP Leo and V471 Tau. Plotting the required energy $\Delta E/E$ as a function of the assumed radius of the core, we also find that the latter yields a characteristic shape for all systems explored here, with a minimum at a core radius $R_{\rm core}/R \sim 0.6$. The normalization of the curves depends however on the system, which appears to be separated into two groups, those with $\Delta E/E \sim 0.03 - 0.9$ where the Applegate mechanism is clearly feasible, and another group with $\Delta E/E \sim 60 - 300$. Our current sample shows a gap in between these groups of about two orders of magnitude in $\Delta E/E$. It does, however, remain to be explored whether the gap is of physical origin. In the case of RX J2130.6+4710, whether or not it is part of the lower group, with $\Delta E/E < 1$, or if it indeed lies within the gap needs to be further explored. Such a determination is currently not possible, as there is only a lower limit on its modulation period, and observations over a longer baseline will be necessary to test this possibility.

We explore further what determines if the Applegate mechanism is feasible in a particular system, focusing on the parameters α and β in our Applegate framework. While the first parameter appears uncorrelated to the minimum $\Delta E/E$, β shows clear correlation for our sample. We also show that this correlation appears related to the strength of rotation in the system, particularly the ratio of the rotation period of the secondary star (which is equal to the binary period in the case of tidal locking) over the critical breakup period of the secondary. In particular, we emphasize that all systems with low minimum values of $\Delta E/E$ have low ratios of $P_{\rm bin}/P_{\rm critic}$. The latter suggests that rotation plays a relevant role in determining the feasibility of the Applegate mechanism. The effect that rapid rotation plays on the magnetic field of M dwarfs is explored by Morgan et al. (2012) using WD+dM binaries and comparing the activity level and strength to field dMs. The authors find that dMs have a higher

activity fraction in the range of spectral types M0 to M7, when they are in a close binary and it was attributed to the increment of stellar rotation in the paired dMs. In the same study, it was also found that the activity is increased in WD+dM across all spectral types when compared to the unpaired dM. This strengthens our main conclusion, namely higher rotation relative to critical rotation supports the Applegate mechanism in PCEBs.

We also note that there may be other mechanisms that can change the quadrupole moment of a star. A minor effect could be related to the side of the M dwarf facing the white dwarf, which will be more deformed than the other side, and this effect is expected to depend on the binary separation. The magnetic fields from the white dwarfs in the systems, considered here, have been neglected so far, but it is also straightforward to show that their expected contributions would be smaller than the typical surface fields from M dwarfs required to drive the Applegate mechanism (see Applegate, 1992). A generic remark, that is important to make, is that several of the systems examined here cannot be explained under the Applegate hypothesis (at least with the two-zone model adopted here), and it remains to be explored if another mechanism is operating in them, or if the latter hints at a more fundamental problem in our current understanding.

To make further progress on this topic, we encourage direct imaging attempts as pursued by Hardy et al. (2015), particularly for cases where the presence of planets appears plausible. In addition, other methods like radial velocity measurements can be employed to determine independent constraints on the potential motion of the secondary star (Oshagh, Heller, and Dreizler, 2017). The precise photometry obtained via the Gaia satellite may further be valuable to determine if motions of the center of mass of the systems can be confirmed in the plane of the sky. Such independent constraints or measurements will be extremely valuable to confirm or rule out the existence of planets.

At the same time, it will be important to probe the presence of magnetic activity and in particular the duration of the magnetic cycle, as recently pursued for instance by Perdelwitz et al. (2017). The latter is critical to understanding if the observed modulation period is consistent with the activity cycle of the secondary star, and provides an independently relevant test to probe the physics of the eclipsing time variations. We also note here that stellar magnetism and the presence of planets are not necessarily mutually exclusive alternatives, but may simultaneously occur. In particular, we have identified several systems here, where we expect that magnetic activity may not explain the observed eclipsing time variations, but include relevant scatter in the observed eclipsing times, due to values of $\Delta E/E \sim 10$, corresponding to fluctuations on the 10% level. The presence of such fluctuations may potentially also explain that in some cases, the subtraction of approximately quadratic terms is needed, as noted recently by Bours et al. (2016) in the case of NN Ser. They also presented eclipsing times for a set of 67 close binaries. Besides the PCEBs from Völschow et al. (2016) we have included RX J2130.6+4710. This is because this is

the only new system with a long enough observational baseline to constrain the modulation period, namely at least 30 yr, and with large O–C variations. Extending the baselines will be important to extend the analysis presented in this paper.

We expect additional theoretical work to be necessary in the future, as the Applegate model employed here (Völschow et al., 2016), while being a significant improvement compared to the first version laid out by Applegate (1992), is still based on a two-zone approximation. While some suggestions for generalizations exist (e.g. Lanza, 2005; Lanza, 2006), the models require further exploration before applying them systematically to a larger sample of systems, and need to be linked more strongly to the dynamo itself. We expect this to be a promising area for further developments.

Chapter 5

Applegate Mechanism from 3D MHD Simulations

This chapter presents the results from the simulations performed with the PENCIL CODE introduced in Section 3.2 together with the setup in Section 3.2.4. Based on Navarrete et al. (In preparation).

We run two simulations with different rotation rates, namely *run3x* with 3 times solar rotation, and *run20x* with 20 times solar rotation rate. Quantities with an overline indicate an average over the azimuthal angle; e.g. $\overline{B_r}$ indicates an average of the r component of B over ϕ and is given by

$$\overline{B}_r = \frac{\int B_r(\phi)\, d\phi}{\int d\phi}. \tag{5.1}$$

Other averages are presented inside angular brackets with subindexes and superindexes. For example, $\langle \overline{B}_r \rangle_i^k$ indicates an average of $\overline{B_r}$ in regions denoted with i and k. The subindex indicates the depth at which the quantity of interest is taken and the superindex indicates the latitude where the average is further calculated with the following rules:

$$i = \{\mathrm{s}, \mathrm{m}, \mathrm{b}\}, \tag{5.2}$$

$$k = \{\mathrm{np}, \mathrm{eq}, \mathrm{sp}\}, \tag{5.3}$$

where

$$\mathrm{s} = \mathrm{surface} \rightarrow \mathrm{r} = 0.98\mathrm{R}, \tag{5.4}$$

$$\mathrm{m} = \mathrm{middle} \rightarrow \mathrm{r} = 0.85\mathrm{R}, \tag{5.5}$$

$$\mathrm{b} = \mathrm{bottom} \rightarrow \mathrm{r} = 0.72\mathrm{R}, \tag{5.6}$$

and

$$\mathrm{np} = \mathrm{north} - \mathrm{pole} \qquad 75^\circ < \theta < 0^\circ, \tag{5.7}$$

$$\mathrm{eq} = \mathrm{equator} \qquad 20^\circ < \theta < -20^\circ, \tag{5.8}$$

$$\mathrm{sp} = \mathrm{south} - \mathrm{pole} \qquad 0^\circ < \theta < -75^\circ, \tag{5.9}$$

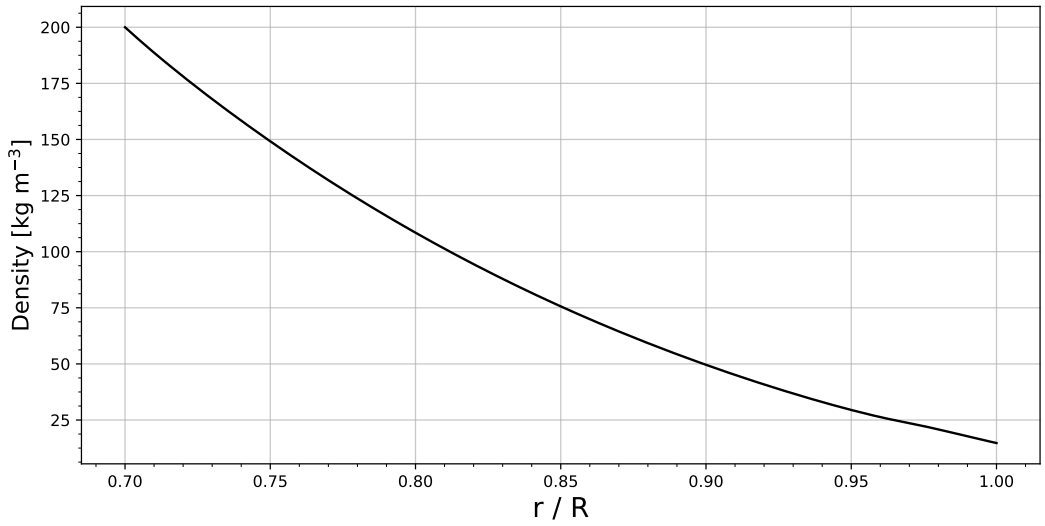

FIGURE 5.1: Density profile for run20x. Source: own work (Navarrete et al., In preparation).

where θ is latitude. So for example, $\langle \overline{B}_r \rangle_s^{eq}$ indicates the average of the azimuthally-averaged B_r over $20^\circ < \theta < -20^\circ$, i.e. the **eq**uator, at the **s**urface of the computational domain.

A typical density and temperature profile is shown in Figures 5.1 and 5.2, respectively, which correspond to run20x at the end of the run. The density at the bottom is 181.8 kg m^{-3} and 13.6 kg m^{-3} at the surface. This corresponds to a density stratification of

$$\frac{\rho_{\text{bottom}}}{\rho_{\text{surface}}} = 13.4. \tag{5.10}$$

The density profile corresponds to an $n = 1.5$ polytrope (see Figure 5.1). The temperature profile is shown in Figure 5.2. The temperature at the bottom is set to be the same as the temperature at the bottom of the convective zone in the Sun, namely $T = 2 \times 10^5$ K. At the surface the temperature is 1.9×10^4 K.

The time-averaged rotation profile at six latitudes for run20x is shown in Figure 5.3. Overall the rotation is faster in the equator than in the poles, but between r = 0.90 and r = 0.95 we observe an increase in the rotation of the north pole (see the cyan-dotted line in 5.3, where it becomes comparable to the rotation in the equator. In Figure 5.4 we also show the time-averaged rotation profile for run3x. Closer to the equator the radial variation of rotation is larger than in the case of run20x where it doesn't vary much with radius at low latitudes. The ratio of the rotation rate of run20x to run3x at the surface's equator is 6.3.

The simulations first have to go through a relaxation phase. The description that follows corresponds to run20x but it is qualitatively similar run3x, with the only difference being the exact timescales. On the one hand the system has to reach dynamo saturation, which is seen in Figure 5.5 where we plot the root-mean-squared magnetic field for run20x. The seed magnetic field first decays very rapidly because

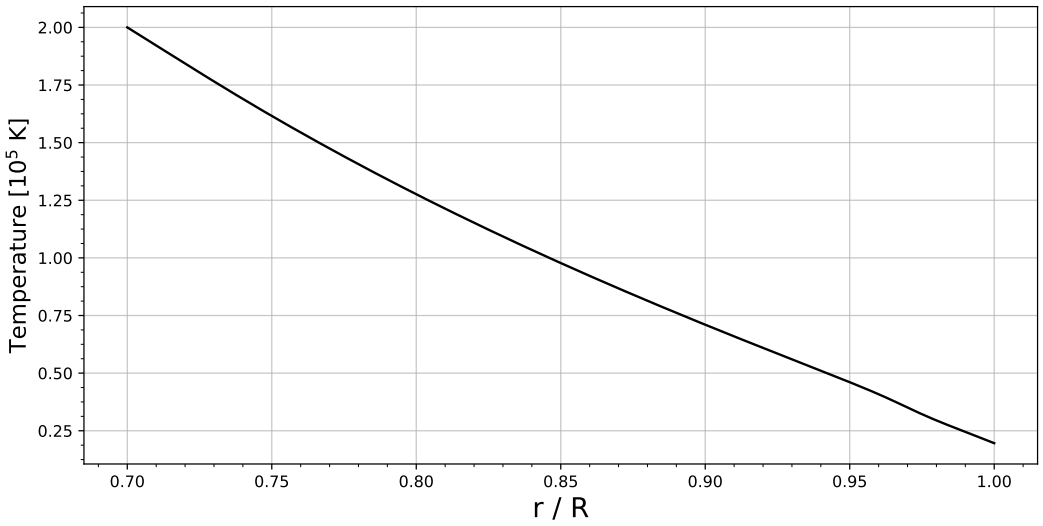

FIGURE 5.2: Temperature profile for run20x. Source: own work (Navarrete et al., In preparation).

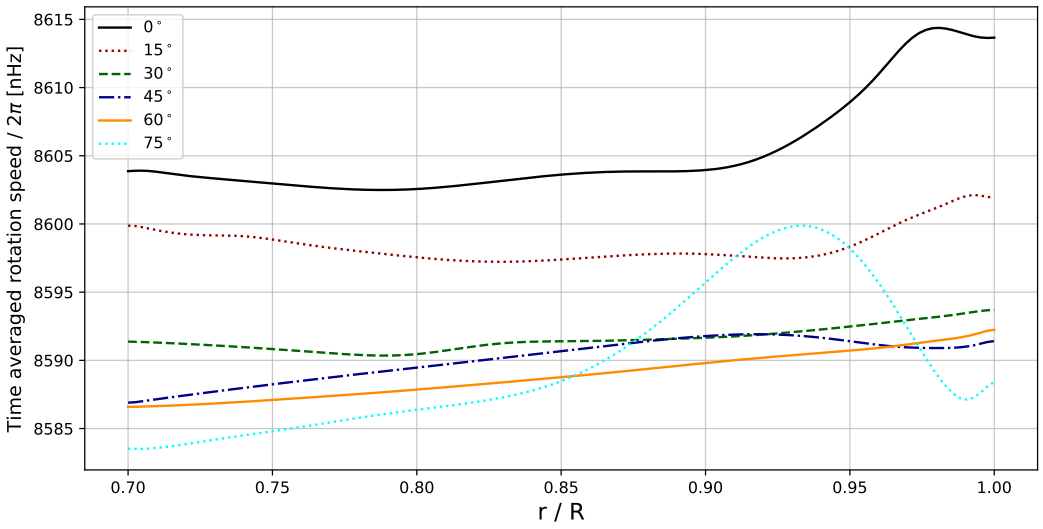

FIGURE 5.3: Rotation profile for run20x. Source: own work (Navarrete et al., In preparation).

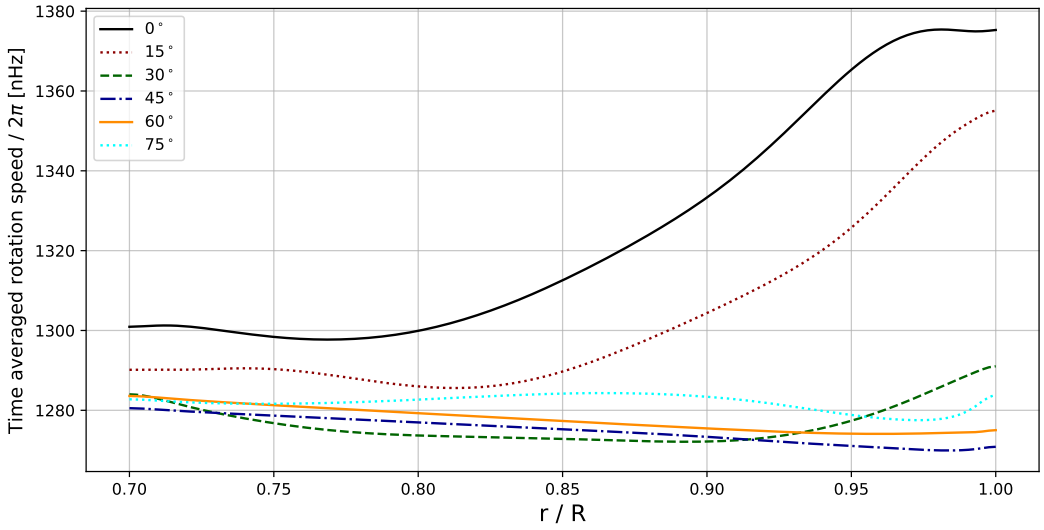

FIGURE 5.4: Rotation profile for run3x. Source: own work (Navarrete et al., In preparation).

most of its magnetic energy is contained in the small scales and quickly gets dissipated (Dobler, Stix, and Brandenburg, 2006). Following this the magnetic field

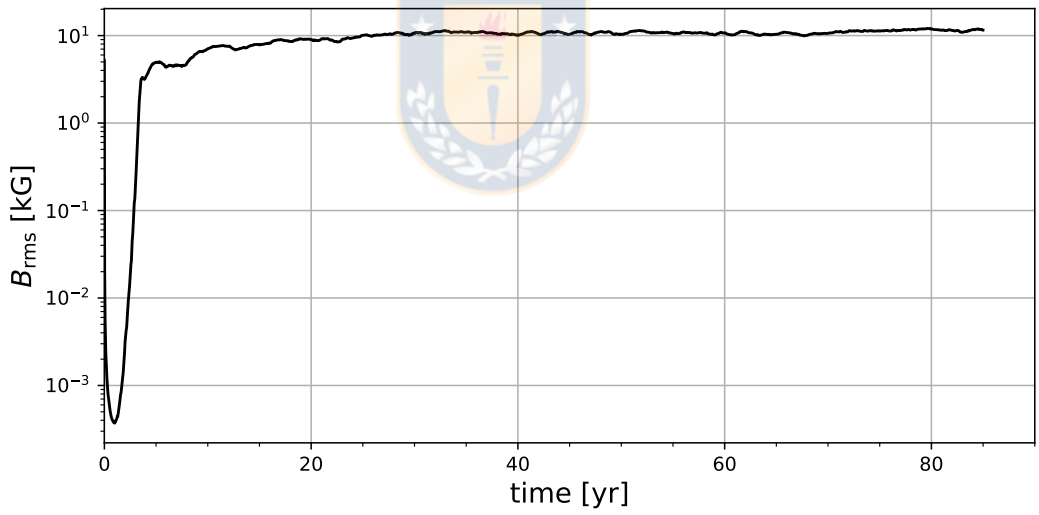

FIGURE 5.5: Saturation of the dynamo. B_{rms} grows exponentially up to the saturation regime where the analysis is performed. Source: own work (Navarrete et al., In preparation).

grows exponentially during the next three years, know as the kinematic stage. This growth then becomes less violent until it reaches the saturation stage at the 22 years mark.

The system also has to reach what is called the thermally saturated regime, which is shown in Figure 5.6, where we plot the fraction of thermal to total energy. The only energy source in the simulations is the energy injected from the bottom. This energy is slowly carried to the surface, thus increasing the thermal energy. After $\sim$ 8 years

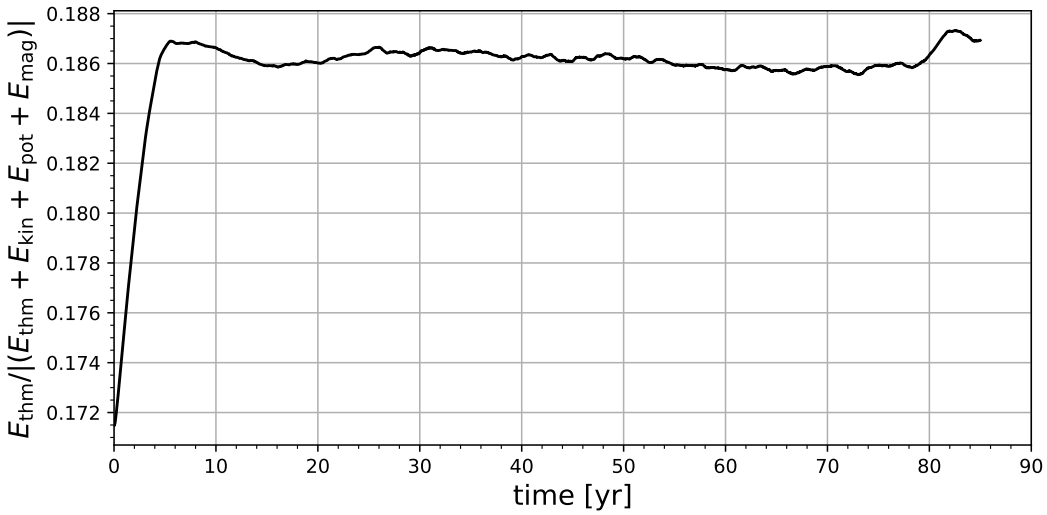

FIGURE 5.6: Evolution of the thermal energy as a fraction of the total energy of the system. E_{thm} is the thermal energy, E_{kin} is the kinetic energy, E_{pot} is the potential energy, and E_{mag} is the magnetic energy. The first exponential growth is because it takes time for the system to carry the radiated energy coming from the bottom to the surface. Source: own work (Navarrete et al., In preparation).

the thermal saturation is reached.

All of the presented analysis is performed in the saturated regime. The calculation and output of the gravitational quadrupole moment was implemented after the beginning of the simulations, which is why the time axis does not start at 0.

First we show the gravitational quadrupole variations of a fully-hydro simulation which will become useful when presenting the simulations with magnetic fields included. The case of the slow rotator (run3x) is presented in Sect. 5.2 followed by the analysis of the fast rotator (run20x) in Sect. 5.3.

5.1 Purely hydrodynamical simulation

In this section we present the variations in the gravitational quadrupole moment of the same simulation as in run20x (i.e. 20 times solar rotation) but without magnetic fields.

Figure 5.7 shows the gravitational quadrupole moment component Q_{xx} in the dotted line, together with the thermal energy as a fraction of the total energy of the system as solid line. Here we can see very high frequency oscillations with a period of 0.18 years. This might correspond to the sound-crossing time τ_{sc}, which we calculate as

$$\tau_{sc} = \frac{2\, r_{conv}}{\langle c_s \rangle_{vol}}, \tag{5.11}$$

where r_{conv} is the radial extent of the simulations, and $\langle c_s \rangle_{vol}$ corresponds to the sound-speed, c_s, averaged over the radial direction. The sound-speed is calculated

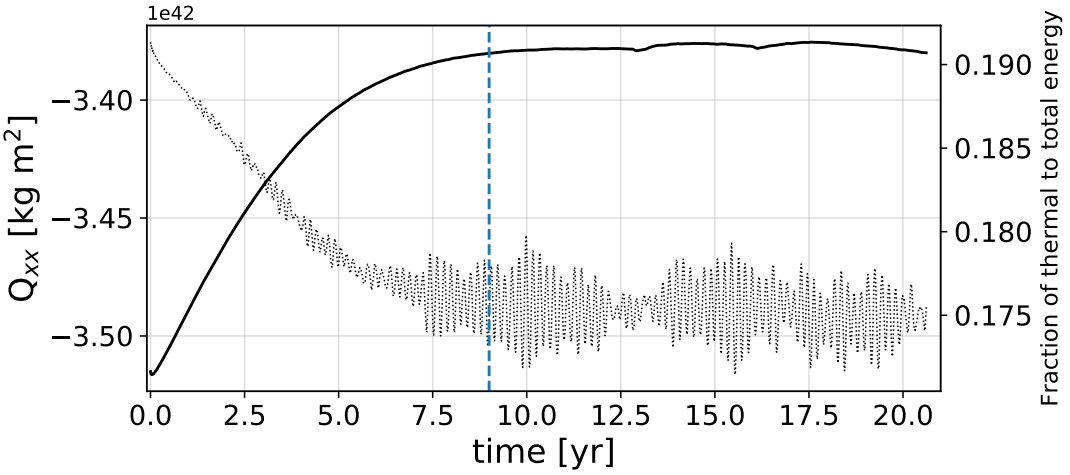

FIGURE 5.7: Gravitational quadrupole moment (Q_{xx}; dotted line) variations together with the thermal energy of the system (solid line). High frequency oscillations are obtained. The thermal relaxation phase coincides with the phase of gravitational quadrupole moment relaxation, marked with the dashed blued line. Source: Navarrete et al. (In preparation).

as

$$c_s = \sqrt{\left(\frac{\partial p}{\partial \rho}\right)_s} \tag{5.12}$$

where the subscript 's' indicates the derivative is taken at constant entropy. By doing this, we obtain

$$\tau_{sc} = 0.182 \text{ years}, \tag{5.13}$$

confirming that these high frequency oscillations have a purely hydrodynamical nature.

5.2 The case of the slow rotator (run3x)

5.2.1 Overview of convective and magnetic states

First we show two snapshots at the end of the simulation. Figure 5.8 shows a Mollweide projection (namely an equal-area map projection also known as *homolographic projection*) of the surface radial velocity, i.e. the convection velocity at the top. The colorbar is cut at ± 90 m s^{-1} to improve visualization. At the equator we see elongated cells (sometimes called banana cells). Their existence is due to the influence that rotation has on the flow (see Käpylä et al., 2011; Viviani et al., 2018). At higher latitudes the effects of rotation are smaller and thus the banana cells disappear, giving rise to more symmetric cells. It should be noted that these cells are much bigger than the real ones observed in the Sun. The mean radial velocity is $\pm$ 60 m s^{-1}, but it can be as high as $\sim \pm$ 1000 m s^{-1}.

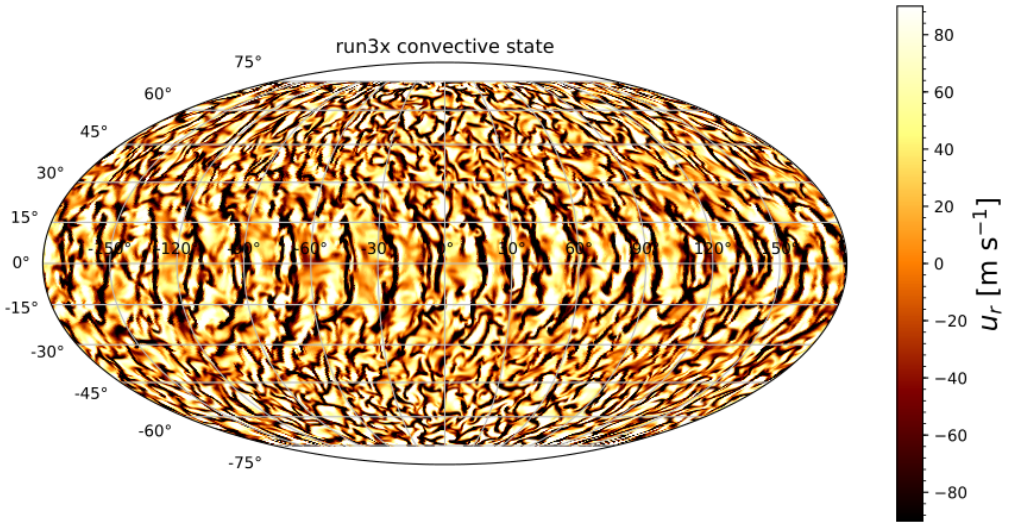

FIGURE 5.8: Radial velocity at the surface for run3x. The colorbar is cut at ± 90 m s^{-1} to improve visualization. Source: own work (Navarrete et al., In preparation).

In Figure 5.9 we plot the surface radial magnetic field at the end of the simulation. The colorbar is cut at ± 5 kG to improve visualization. Overall, there are no large

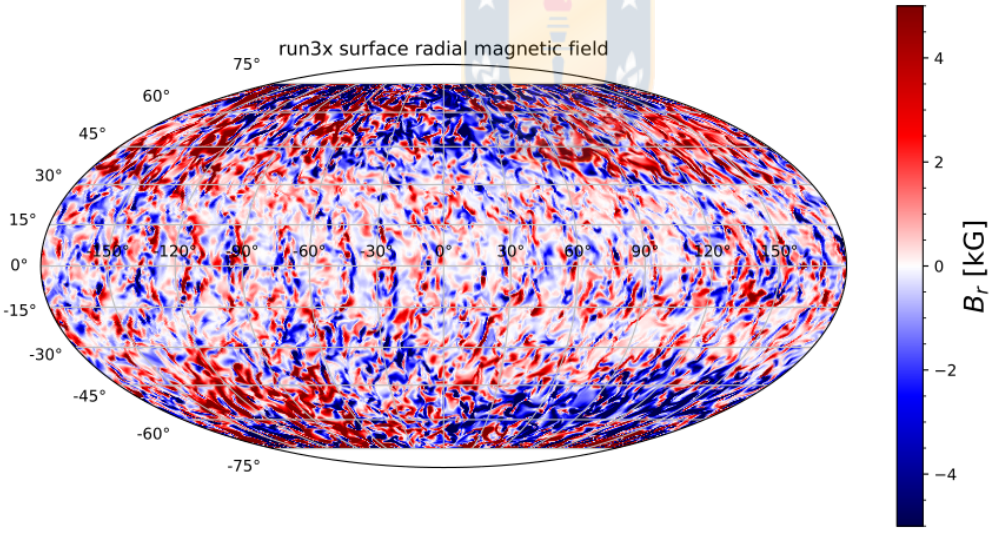

FIGURE 5.9: Radial magnetic field at the surface for run3x. The colorbar is cut at ± 5 kG to improve visualization. Source: own work (Navarrete et al., In preparation).

scale structures. The magnetic field strength at the equator is weaker than in the poles, and no strong non-axisymmetric component is observed. The mean magnetic field strength is 2.5 kG and the extrema are $\pm$ 90 kG. The length of these structures is much larger than real sunspots.

5.2.2 Overview of the magnetic field evolution

We start the analysis by looking at the dynamo solution of the slow rotator. Figure 5.10 shows the evolution of the mean toroidal magnetic field (butterfly diagram) of run3x at three radial depths labeled at each panel. At the northern hemisphere there

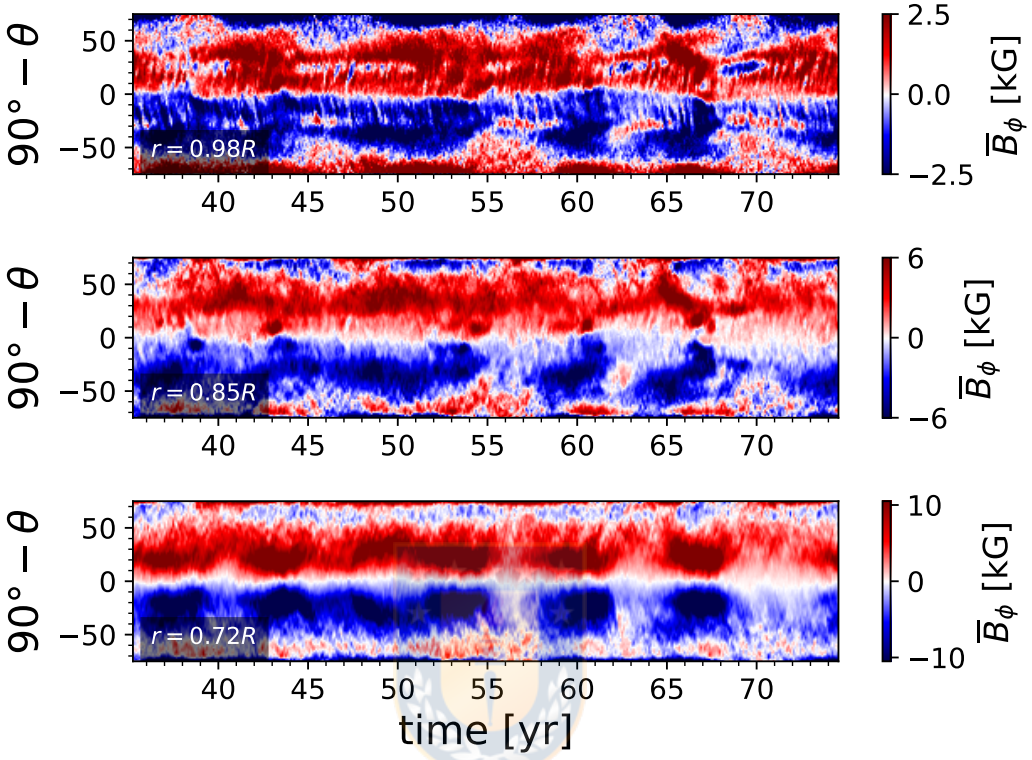

FIGURE 5.10: Time evolution of the mean toroidal magnetic field $\overline{B}_\phi$ at three different depths, labeled at the lower-left corner of each panel. There is no magnetic field migration nor polarity reversals. The magnetic field is changing its intensity and there are short periods where the activity is much weaker. Color bars are cut to improve visualization. Source: own work (Navarrete et al., In preparation).

is an overall positive polarity whereas in the southern hemisphere the dominant polarity is negative, with no magnetic reversals. In each panel, the polarity of the poles is opposite to the dominant polarity. At the bottom of the convective region (third panel) there are weak polarity reversals at both poles. In the middle (second panel), these reversals at the poles are stronger and thus easier to see. At the surface no major reversals of $\overline{B}_\phi$ are observed. Meanwhile, from the equator to mid latitudes the magnetic field is evolving by increasing and decreasing its strength. At the three reference depths there are episodes of decreased activity, for example at the equator during the time frames of 56 to 57 years and 62 to 64 years. The extrema at the bottom, middle, and surface are $\pm$ 20 kG, $\pm$ 7 kG, and $\pm$ 3 kG, respectively.

The evolution of the radial field is shown in Figure 5.11. At the bottom of the convective zone (bottom panel) the behaviour of $\overline{B}_r$ is similar to the one described for

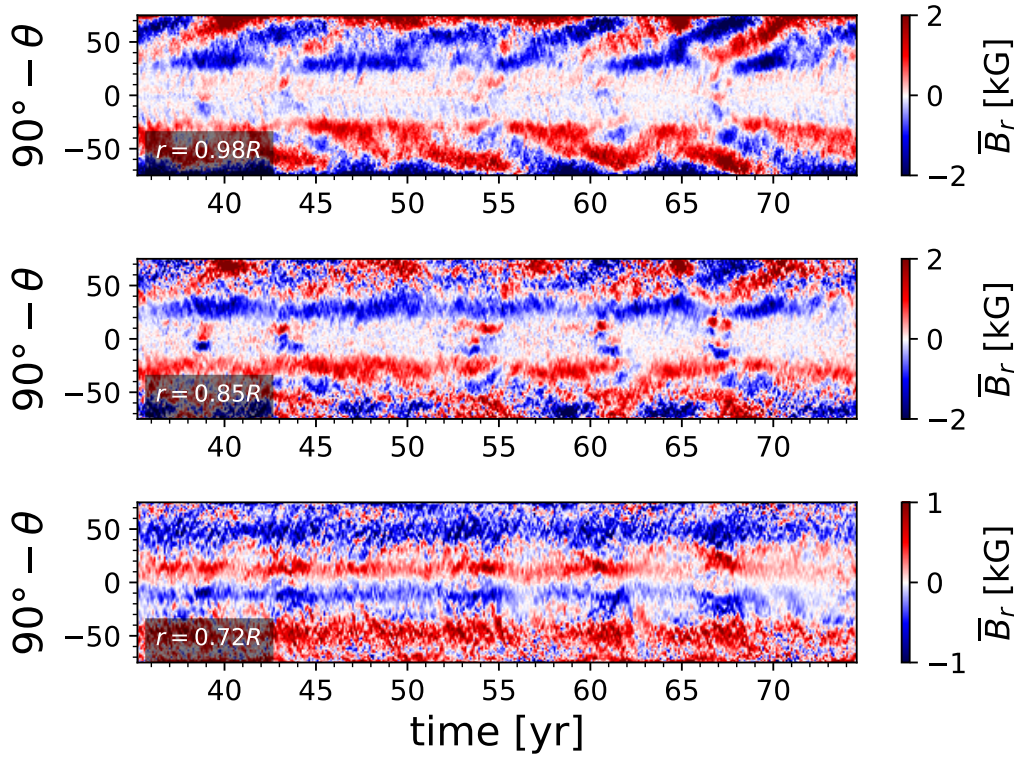

FIGURE 5.11: Time evolution of the mean radial magnetic field $\overline{B}_r$ at three different depths, labeled at the lower-left corner of each panel. A poleward migration of the magnetic field is clearly seen at the surface of the domain, but there is no activity at the equator in the surface and middle of the domain. Sporadic activity is seen at the equator. Source: own work (Navarrete et al., In preparation).

the toroidal field at the surface. At low latitudes and towards the equator the magnetic field is positive (negative) at the northern (southern) hemisphere, and there are no signals of polarity reversals. In the middle of the convective region we start seeing hints of a poleward migrating dynamo wave (see second panel in Figure 5.11) acting at latitudes of $\pm 50^\circ$ in both poles. Meanwhile, at mid latitudes ($\pm 30^\circ$) a persisting negative (positive) magnetic field is obtained with no migration. Whereas at the equator, the mean radial magnetic field is weaker but with periods of increased strength at $t = 39, 43, 55, 51,$ and, 67 years. In the surface of the star (top panel) a dynamo wave is obtained with a poleward migration. In the equator the strength of $\overline{B}_r$ is weaker with periods of increased strength at the same times as in the middle of the computational domain.

5.2.3 Origin of the Q_{xx} fluctuations

Here we discuss the origin of the variations in Q_{xx}, which is shown in Figure 5.12. As a starting point we compare the average radial magnetic field at the surface averaged over the north pole is shown in Figure 5.13. We can see peaks of the magnetic field and how they relate to the quadrupole moment. The first peak of the magnetic field

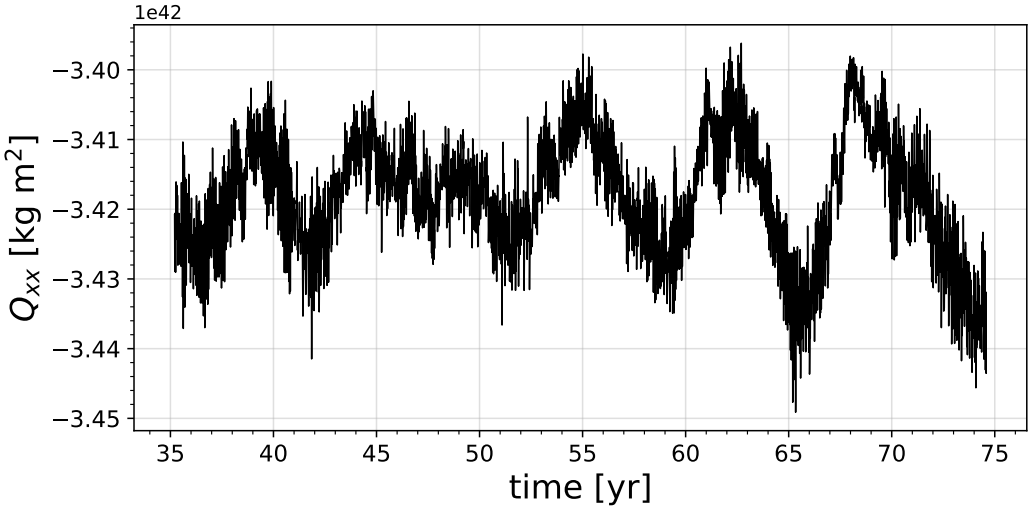

FIGURE 5.12: Evolution of the gravitational quadrupole moment in run3x. The very high frequency oscillations with hydrodynamic origin are still present. The obtained large variations have a period of $\sim$ 5 to 6 years. Source: own work (Navarrete et al., In preparation).

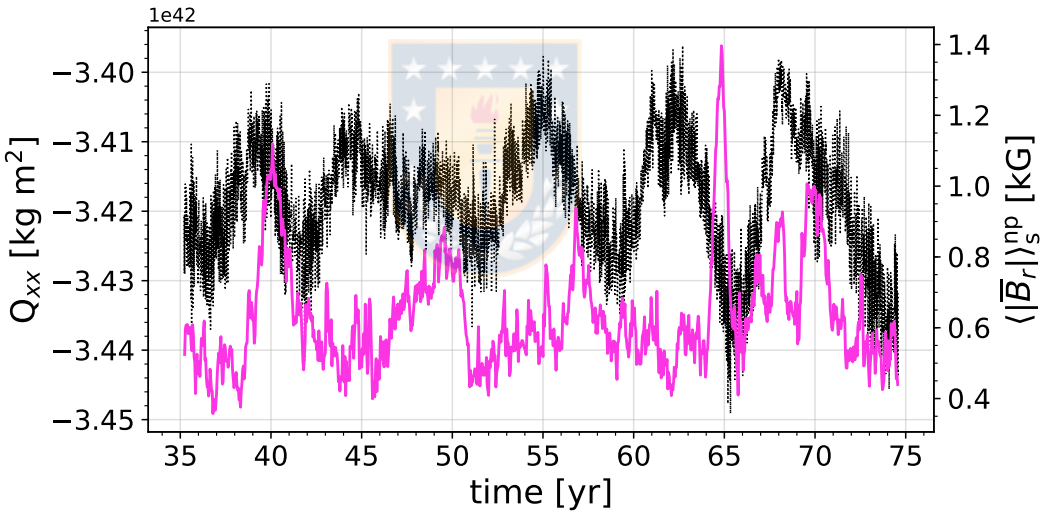

FIGURE 5.13: Time evolution of the gravitational quadrupole moment component Q_{xx} (black-dotted line) together with the absolute value of the azimuthal-average of the radial magnetic field at the surface averaged over the north pole (magenta-solid line). The variations of Q_{xx} can be interpreted as a reaction to the changes of the magnetic field intensity (see text). Source: own work (Navarrete et al., In preparation).

at $t = 40$ years can be related to the minimum of Q_{xx} at $t = 41.7$ years. Then, the continuous increase in the magnetic field intensity from $t = 45$ years to $t = 50$ years is reflected in a decrease of Q_{xx} starting at the 45 years mark to $t = 51$ years.

To see this trend more clearly, we plot in Figure 5.14 the same figure but with the right y-axis inverted and also the magnetic field average is shifted in time by 1.77 years. By doing this we see the trend more clearly and a very close correlation

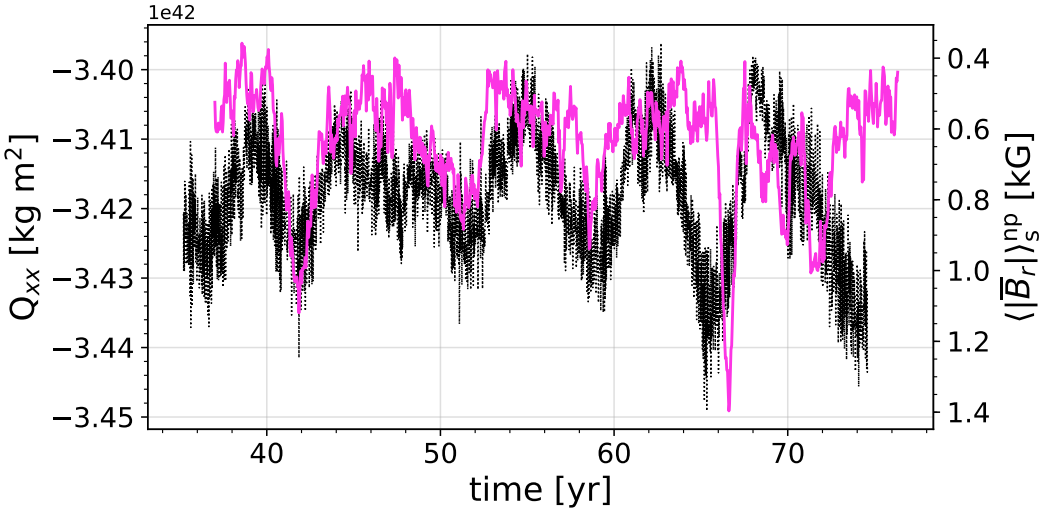

FIGURE 5.14: Same as Figure 5.13 but with the right y-axis inverted and the averaged magnetic field is shifted 1.77 years in time. Source: own work (Navarrete et al., In preparation).

is revealed due to a phase shift in the variation of Q_{xx} and B_r. A stronger (weaker) magnetic field is related to an increase (decrease) in the absolute value of Q_{xx}. This figure shows how the magnetic field is intimately related to the overall density field of the star, proving the first step of the Applegate mechanism.

Now, we explore the correlation between the Reynolds stress tensor component $\overline{R}_{r\phi} = \overline{u'_r u'_\phi}$, which is known to trigger azimuthal differential rotation (Käpylä et al., 2016). This is shown in Figure 5.15. The stress at the surface and middle of the com-

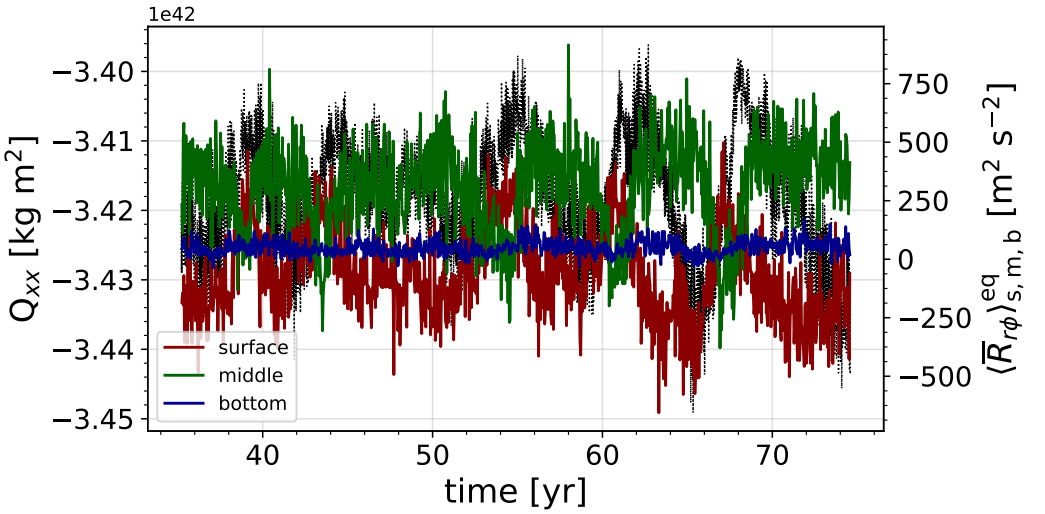

FIGURE 5.15: Time evolution of the gravitational quadrupole moment component Q_{xx} together with the mean averaged of the Reynolds stress component $R_{r\phi}$ at the equator in the surface (darkred), middle (darkgreen), and bottom (darkblue). Source: own work (Navarrete et al., In preparation).

putational domain is very well correlated to the changes on the quadrupole moment,

whereas the one at the bottom is weak and thus has a small contribution and weak correlation to Q_{xx}. From this figure we can interpret how the speed-up (slow-down) of the outer layers increase (decrease) Q_{xx}. This is a key point in the Applegate mechanism, as it was predicted by Applegate (1992) how Figure 5.15 should look like but with analytic arguments.

Finally, we study how the angular momentum affects Q_{xx}. In Figure 5.16, we plot the angular momentum per unit volume averaged over the north pole at the surface (darkred), middle (darkgreen), and bottom (darkblue). From this figure we see how

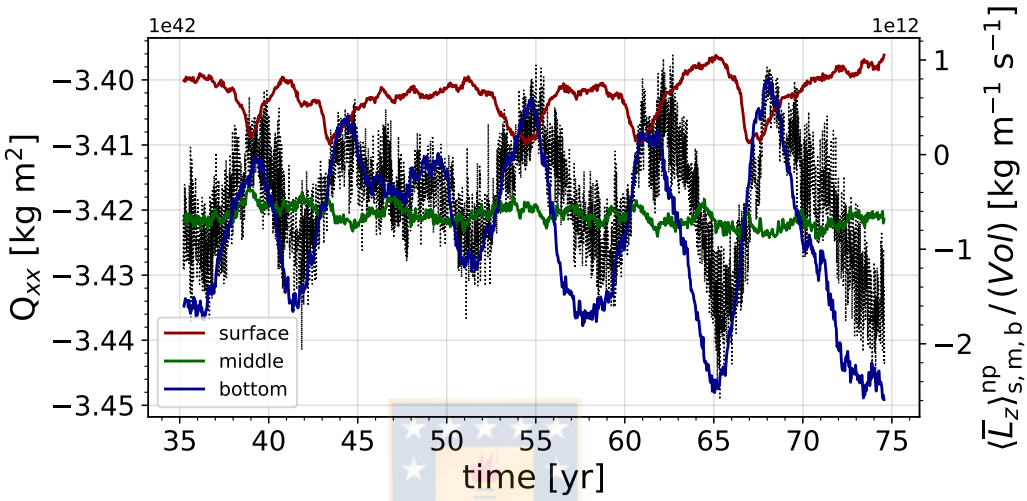

FIGURE 5.16: Time evolution of the gravitational quadrupole moment component Q_{xx} (black-dotted line) together with the angular momentum per unit volume averaged over the north pole at the surface (darkred), middle (darkgreen), and bottom (darkblue) . Source: own work (Navarrete et al., In preparation).

the outer layers carry more angular momentum than the inner ones, and at the surface there is an anticorrelation between the angular momentum and Q_{xx}, whereas at the bottom it turns into a clear correlation. When the angular momentum is larger at the bottom than at the surface, the equatorial portion of the bottom is rotating as fast as on the surface. As this happens the part in the middle is a transition, where rotation is slower.

5.2.4 Gravitational quadrupole moment evolution

Figure 5.12 shows the time evolution of Q_{xx}. There are very high frequency oscillations, with a period of ∼0.18 years, which persist at every moment in the simulations. These oscillations have a hydrodynamic origin rather than an hydromagnetic one, confirmed by the purely-hydro run where these fluctuations are the only ones present (see Section 5.1).

The variations in Q_{xx} are not strictly periodic. There is an episode in its evolution where it takes more time to reach a minimum from a maximum, taking place place from $t \sim 44$ yr to $t \sim 52$ yr. Also, there is one episode when Q_{xx} reaches a global

minimum at $t = 65$ yr. This behaviour is to be expected to a certain degree as the full set of MHD equations are highly non linear. Overall, these fluctuations have a period of ~ 5 to 6 years and semi-amplitudes of $\sim 2.4 \times 10^{40}$ kg m^2.

Keeping in mind the rescaling (see Section 3.2.6), and that the parameters of the magnetically active star in PCEB V471 Tau is close to the Sun, and in this simulations we have the convective region of a Sun-like star, we can use the results from our simulations to estimate the impact in V471 Tau. We take the Q_{xx} semi-amplitude as

$$\Delta Q_{xx} = 2.4 \times 10^{40}\,\mathrm{kg\ m^2} \tag{5.14}$$

and adopt a binary separation of 3.3 $R_\odot$. Inserting this into Equation (2.33) yields

$$\frac{\Delta P}{P} = 2.1 \times 10^{-8}. \tag{5.15}$$

Furthermore,

$$O - C = \frac{\Delta P}{P}\frac{P_{\mathrm{mod}}}{2\pi}, \tag{5.16}$$

where P_{mod} is the modulation period of the $O - C$ diagram (see Applegate, 1992). Combining this equation with Equation (2.33) yields

$$O - C = 0.635\,\mathrm{s}. \tag{5.17}$$

Marchioni et al. (2018) presented the most updated analysis of the eclipsing times of V471 Tau. The authors reported two period variations, one with $O - C = 151$s and $P_{\mathrm{mod}} = 35$ years. The other contribution has a semi-amplitude of $O - C = 20$ s and a modulation period of $P_{\mathrm{mod}} = 9.7$ years. The semi-amplitude obtained from the simulations in this case vary far from the observations in this case (but see the case of run20x in Section 5.3). We must emphasize that in this simulation the rotation rate if much lower than in V471 Tau.

As an exercise, if we change the binary separation from 3.3 $R_\odot$ to 2.0 $R_\odot$ the numbers we obtain are

$$\frac{\Delta P}{P} = 5.74 \times 10^{-8}, \tag{5.18}$$

and

$$O - C = 1.72\,s. \tag{5.19}$$

The peaks might be correlated to the appearance of the radial magnetic field at the equator (see Figure 5.11).

5.3 The case of the fast rotator (run20x)

5.3.1 Overview of convective and magnetic states

Snapshots at the end of the simulation are shown in Figure 5.17 as a Mollweide projection of the surface radial velocity, i.e. the convection velocity at the top, where

colorbars are cut to improve visualization. The banana cells here are still present at

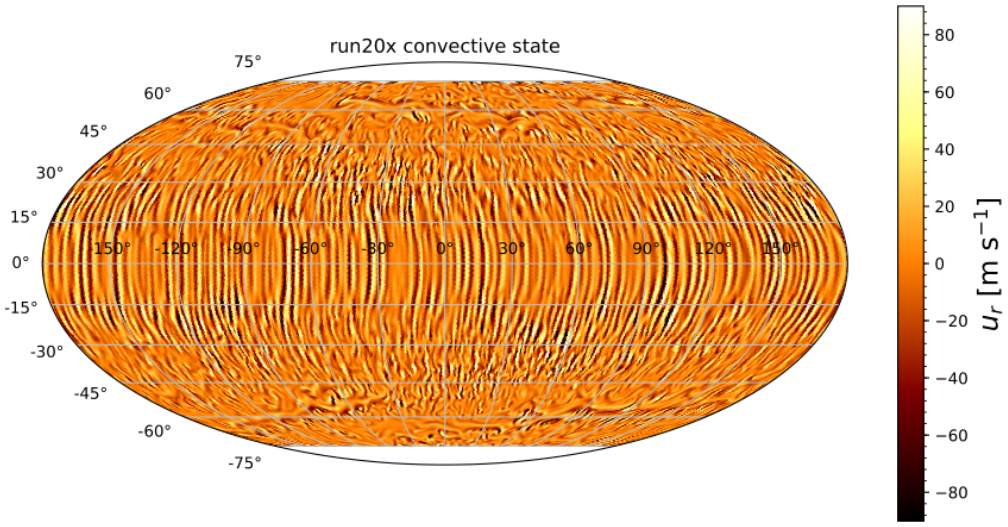

FIGURE 5.17: Mollweide projection of the radial velocity at the surface for run20x. Colorbars are cut to improve visualization. Source: own work (Navarrete et al., In preparation).

the equator but with a decreased azimuthal extent in comparison to run3x. At higher latitudes the size of the convection cells are also reduced. The average convective velocity is 19.4 m s^{-1}, with extrema of 700 m s^{-1} and -561 m s^{-1}.

In Figure 5.18 we plot the surface radial magnetic field at the end of run20x, where colorbars are cut to improve visualization. The radial magnetic field is very

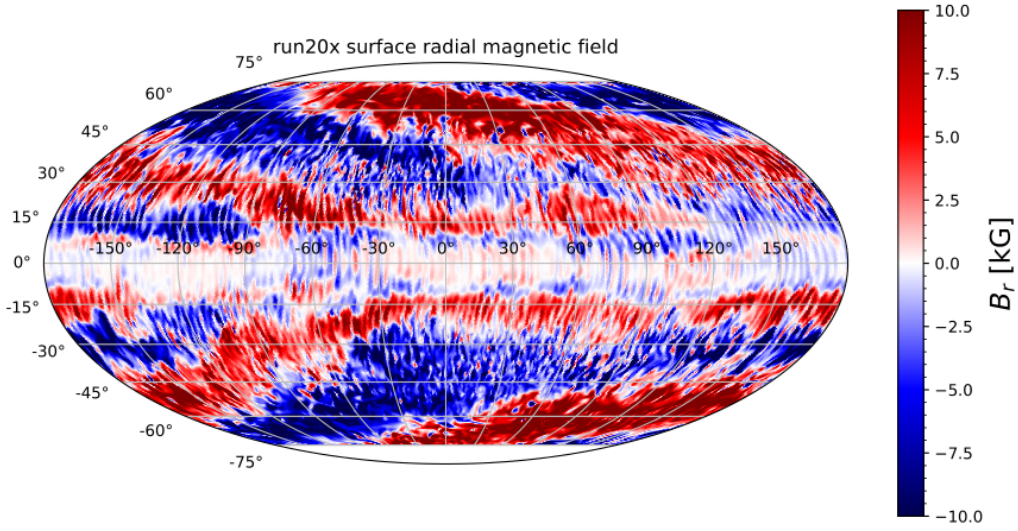

FIGURE 5.18: Mollweide projection of the radial magnetic field at the surface for run20x. Colorbars are cut to improve visualization. Source: own work (Navarrete et al., In preparation).

different from the one in run3x. It is stronger and is more organized. The mean of the radial magnetic field is 4.5 kG, 1.8 times stronger than in run3x. The extrema are

$\sim \pm 90$ kG, the same as in run3x. These large size magnetic structures can cover up to the full azimuthal extent and range from their respective pole to the equator.

5.3.2 Overview of the magnetic field evolution

We follow here the same approach as in the case of the slow rotator. Figure 5.19 shows the mean toroidal magnetic field, i.e. butterfly diagram, at three depths labeled at the lower left corner of each panel. The magnetic field in this case is much

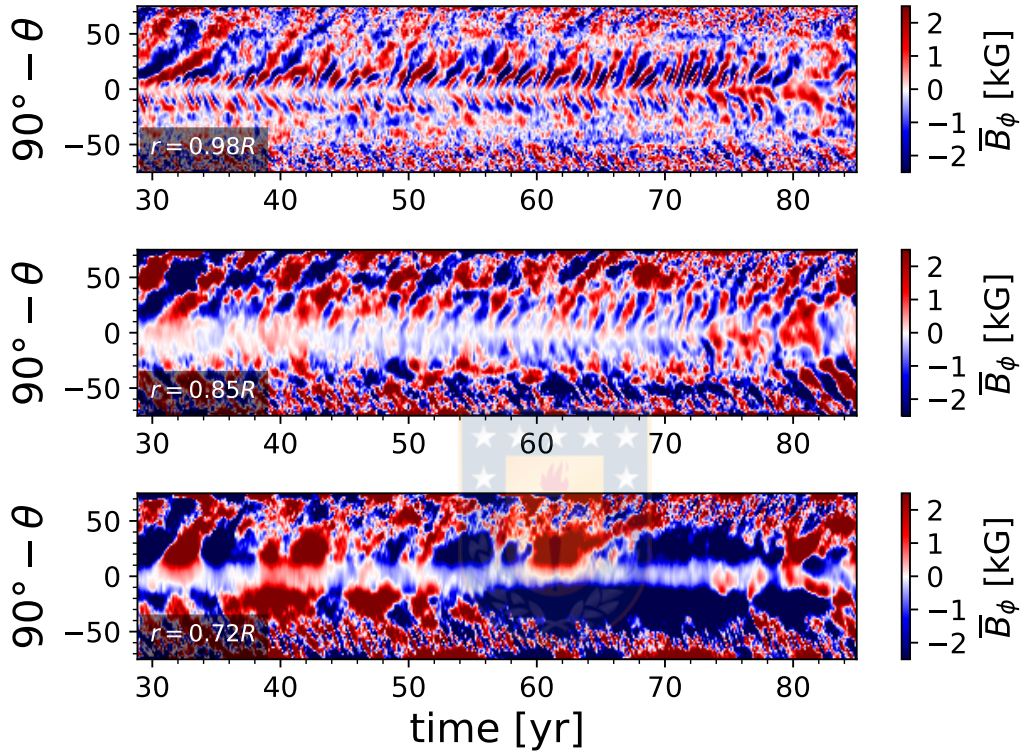

FIGURE 5.19: Time evolution of the mean azimuthal toroidal magnetic field $\overline{B}_\phi$. A poleward migration of the magnetic field is clearly seen at the surface and middle of the domain. At the equator there is an overimposed dynamo wave operating at the north-pole at latitudes between $\sim 5°$ to $\sim 50°$. This non axisymmetric wave is slowly vanishing. The colorbars are cut at ± 2.5 kG for better visualization. Source: own work (Navarrete et al., In preparation).

more complex. At the bottom of the domain the dynamo solution is cyclic and generally ranges from the equator to the poles at the beginning. The maximum amplitudes are ± 12 kG. At later times there is a standing magnetic field from 57 years to 76 years, covering most of the south pole. The dynamo solution at the middle of the domain is persistently cyclic with a poleward migration. Here the extrema of the magnetic field are ± 8 kG. At the surface and at the equator there is an axi-symmetric dynamo wave at low latitudes with extrema of ± 5 kG. Overimposed there is also a non-axisymmetric dynamo wave operating at the north pole at latitudes between $\sim 5°$ to $\sim 50°$, which is slowly decaying in amplitude. The absence of a strong

toroidal magnetic field is due to the radial field boundary condition (see Käpylä et al., 2016; Warnecke et al., 2016).

The same diagram as before but for $\overline{B}_r$ is shown in Figure 5.20. Here, the presence

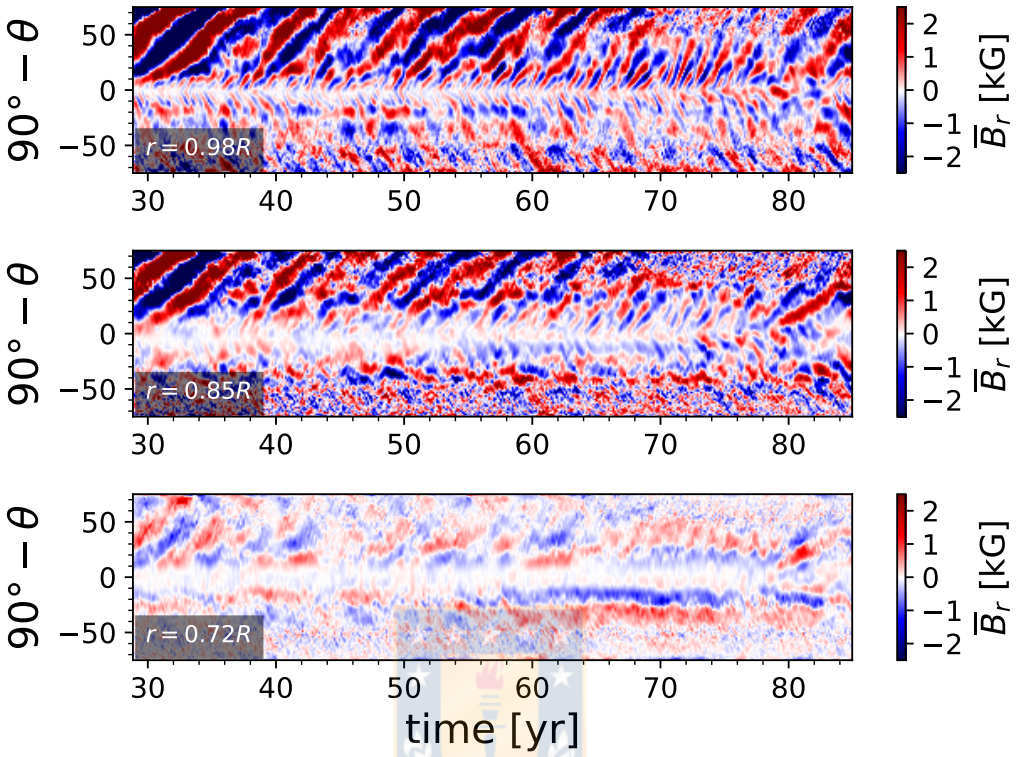

FIGURE 5.20: Time evolution of the mean radial magnetic field $\overline{B}_r$. The non-axisymmetric dynamo wave is clearly seen at the surface and middle of the domain. It is also clearly seen the decrease of its magnitude. Right before the 70 years mark this wave almost disappears and starts to reappear by the end of the simulation. Source: own work (Navarrete et al., In preparation).

of a non-axisymmetric dynamo wave with decreasing amplitude in time is clearly visible and the magnetic fields have a poleward migration. At early times, the surface extrema is ± 20 kG and at the bottom is ± 8 kG. At the stage of the disappearance of the non-axisymmetric between 68 to 80 years the extrema are ± 4 and ± 3 kG respectively.

In both diagrams the behaviour is very different from the case of run3x. This is because the excited dynamo wave depends on the rotation rate of the simulation (see e.g. Viviani et al., 2018). The major differences in the magnetic field evolution between run3x and run20x is that first, the intensity of $\overline{B}_r$ in the former is larger by a factor of 2 at the surface. Second, the overall intensity of the magnetic field in the latter is decaying, whereas in run3x it remains constant on the large scale. And third, the magnetic field is migrating virtually everywhere in run20x, whereas a weak migrating component was found only in specific parts in run3x (see Figure 5.11). We note in summary that the behaviour of the magnetic field is considerably

more complex in the rapidly rotating case.

5.3.3 Origin of the Q_{xx} fluctuations

Analogously, we explore the origin of the Q_{xx} fluctuations. Figure 5.21 shows the time evolution of the gravitational quadrupole moment component, Q_{xx}. We first

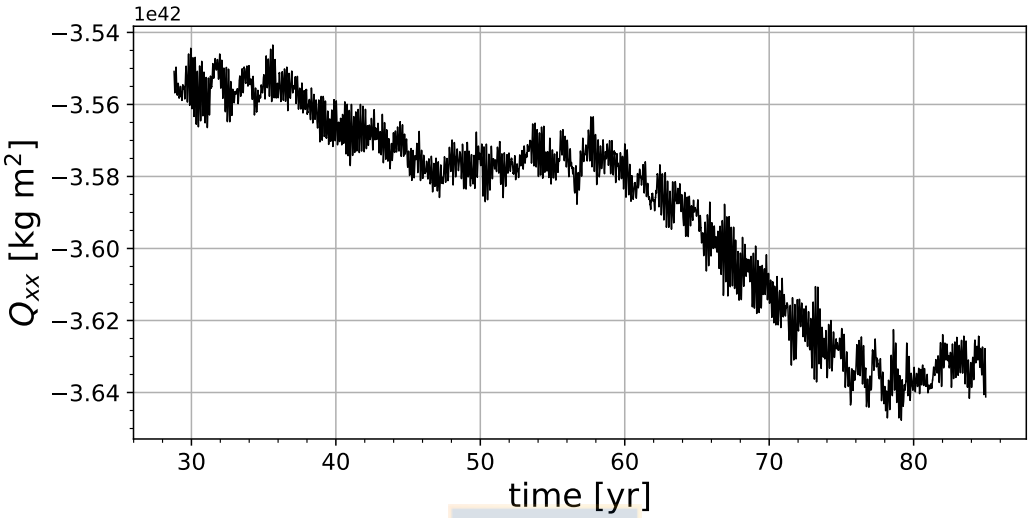

FIGURE 5.21: Time evolution of the gravitational quadrupole moment component Q_{xx} in run20x. Source: own work (Navarrete et al., In preparation).

compare the mean radial magnetic field averaged at the north pole in the surface of the domain, depicted in Figure 5.22. The sharp decrease of $\langle \overline{B}_r \rangle_s^{np}$ reflects how the non-axisymmetric dynamo wave is vanishing (same as in Figure 5.20). It can also be interpreted and seen how Q_{xx} reacts to this by decreasing as well. This correlation is not seen when the same average is taken but at the south pole (see Figure 5.23). In this Figure it can be seen how the south pole has a weaker contribution to the magnetic field when compared to the north pole, which is stronger by a factor of $\lesssim 10$ at $t \sim 32$ years and steadily decreases until they become nearly equal. This quantity starts to increase at the 80 years mark (same as the north-pole component; see Figure 5.22) which coincides with the weak increase in Q_{xx}.

Finally, it can be seen from Figure 5.24 that the average magnetic field at the equatorial portion of the surface of the star does not have important variations nor correlations with Q_{xx}.

Similarly, we plot the same averages the Reynolds stress component $r\phi$ (not the absolute value) at the equator and at the three depths. Figure 5.25 shows such quantities. The average of $\overline{R}_{r\phi}$ at the surface is steadily increasing while Q_{xx} decreases. Meanwhile, the stress at the deeper layers is approximately constant compared to the one at the surface. This hints at a strong anti-correlation between the Reynolds stress at the outer layers. This makes sense as the speed-up/speed-down of the outer

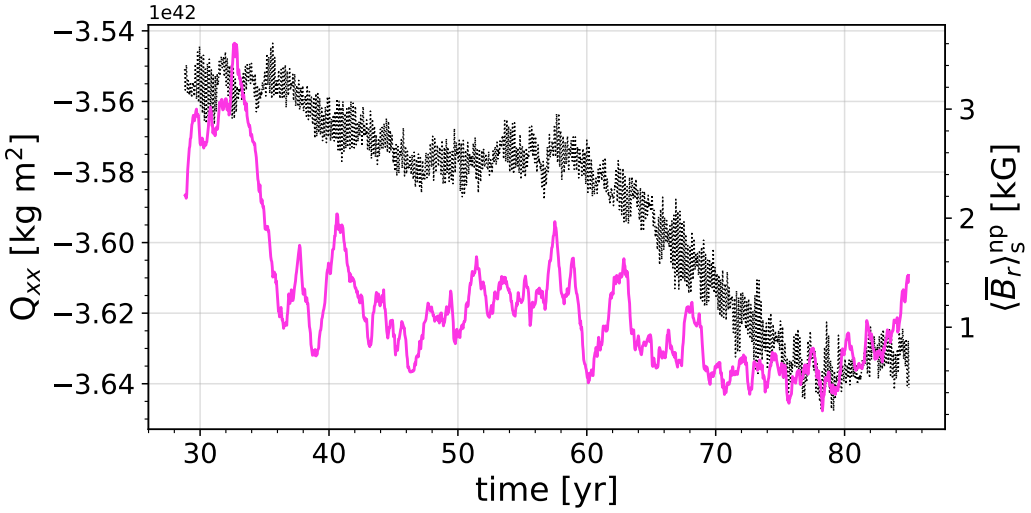

FIGURE 5.22: Time evolution of the gravitational quadrupole moment component Q_{xx} (black-dotted line) together with the absolute value of the mean radial magnetic field averaged at the north pole in the surface of the domain (magenta-solid line). The overall decrease in the averaged magnetic field is due to the characteristics of the dynamo wave. Source: own work (Navarrete et al., In preparation).

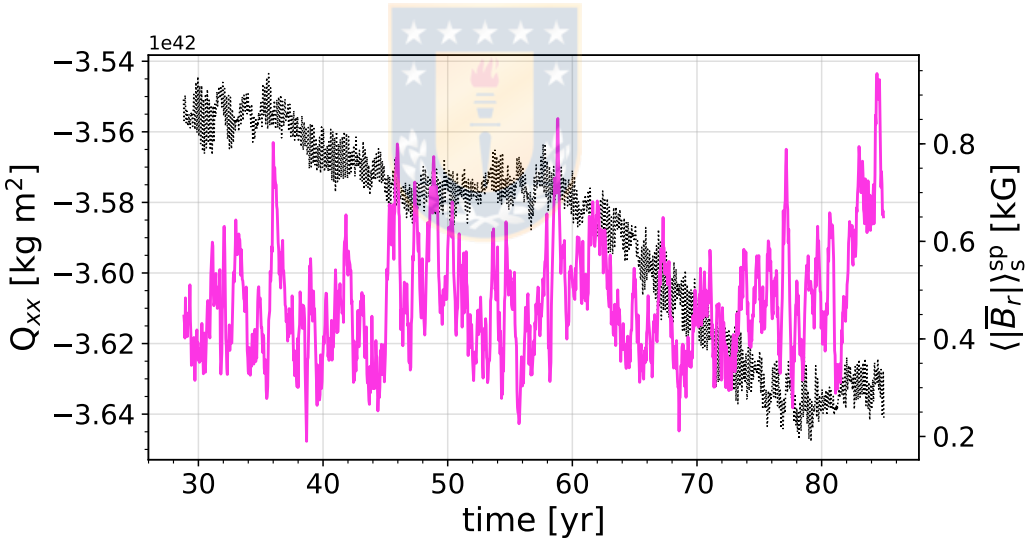

FIGURE 5.23: Time evolution of the gravitational quadrupole moment component Q_{xx} (black-dotted line) together with the absolute value of the mean magnetic field component r averaged at the south pole in the surface of the domain (magenta-solid line). Source: own work (Navarrete et al., In preparation).

layers are the ones which have a larger impact on the changes on Q_{xx} (see Applegate, 1992).

To investigate how the angular momentum transfer affects Q_{xx}, we plot the mean angular momentum per unit volume averaged over the north pole at the three depths in Figure 5.26. We can see how the quadrupole moment reacts with a good correlation to changes in L_z at the bottom, the same as in the case of the slow rotator.

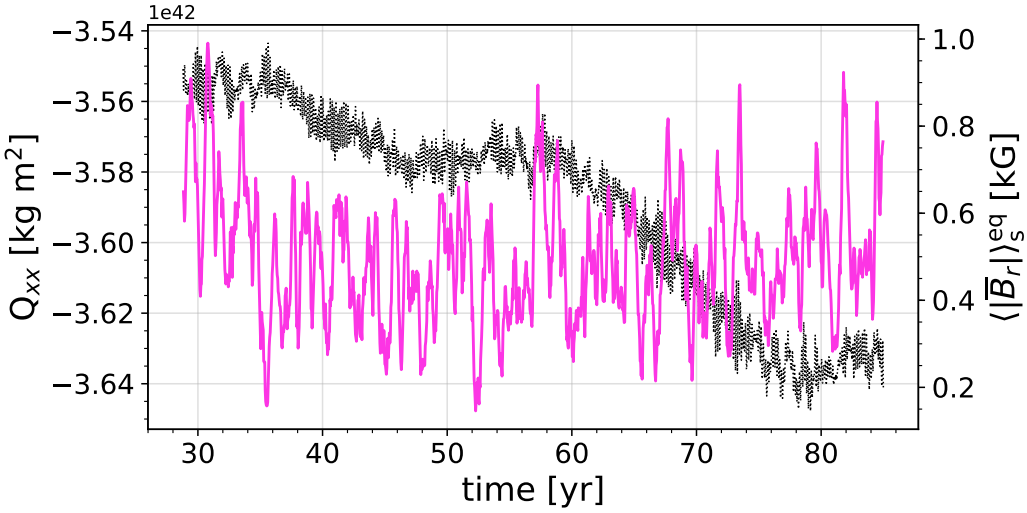

FIGURE 5.24: Time evolution of the gravitational quadrupole moment component Q_{xx} (black-dotted line) together with the absolute value of the mean magnetic field component B_r averaged at the equator in the surface of the domain (magenta-solid line). Source: own work (Navarrete et al., In preparation).

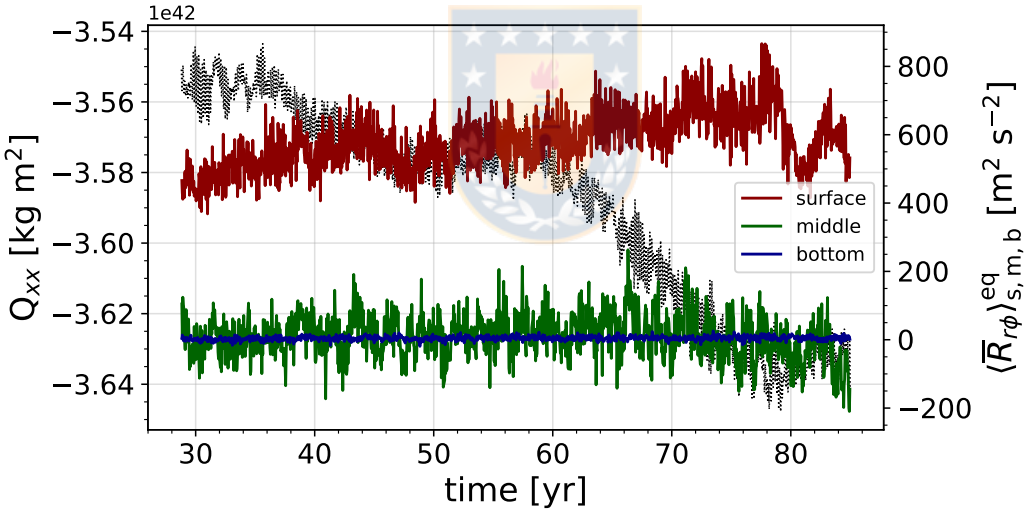

FIGURE 5.25: Time evolution of the gravitational quadrupole moment component Q_{xx} (black-dotted line) together with the mean averaged Reynolds stress component $R_{r\phi}$ at the equator in the surface (dark red line), middle (dark green line), and bottom (dark blue line) of the domain. There is a clear anti-correlation between Q_{xx} and the stress at the equator whereas no correlation is seen between the other two averages. Source: own work (Navarrete et al., In preparation).

While at early times L_z at the bottom increases and Q_{xx} remains constant, the correlation in both quantities after the 40 years mark is high. From this figure we can infer that the angular momentum in the inner layers is correlated to the variations in the quadrupole moment.

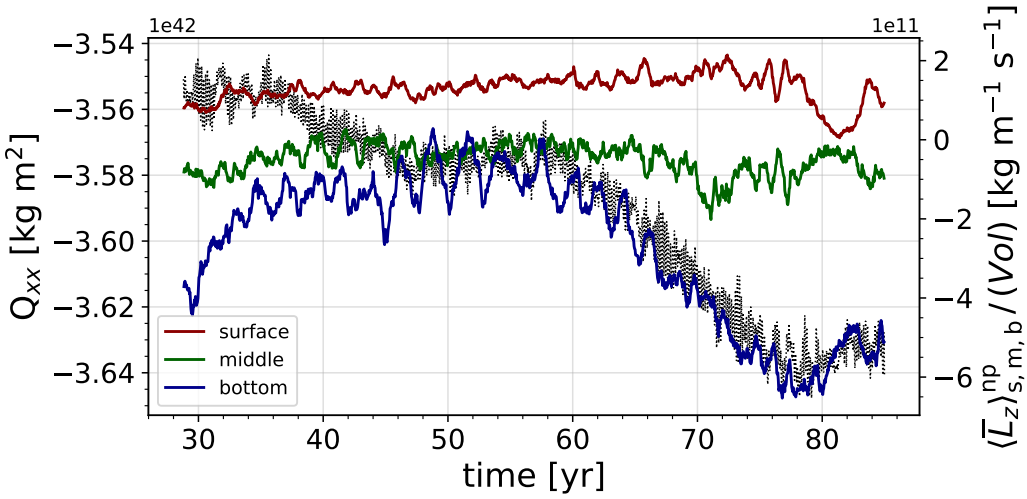

FIGURE 5.26: Time evolution of the gravitational quadrupole moment component Q_{xx} (black-dotted line) together with the angular momentum per unit volume averaged over the north pole at the surface (darkred), middle (darkgreen), and bottom (darkblue) for the fast rotator. Source: own work (Navarrete et al., In preparation).

5.3.4 Gravitational quadrupole moment evolution

The purely-hydro oscillations in Q_{xx} (see Section 5.1) are present, same as in run3x. The differences in the overall behaviour of Q_{xx} in this run are remarkably different from the case of run3x, showing a more complex behaviour. At the beginning from 29 to 37 years Q_{xx} remains constant on larger scales with the presence of oscillations with a period of ∼1.9 years. After the 37 years mark, Q_{xx} decreases from -3.555×10^{42} kg m^2 to -3.579×10^{42} kg m^2. After this, the above described behaviour starts again but now the decrease is stronger and starts at 60 years. Q_{xx} changes from -3.579×10^{42} to -3.640×10^{42}. Analogously to the case of run3x where we rescaled the gravitation quadrupole moment (see Section 3.2.6), we take the system parameters of the magnetically active component in the PCEB V471 Tau and remember that this run has a rotation rate and stellar parameters similar to the magnetically active star in this system, but now we take the maximum and minimum of Q_{xx} to obtain

$$\Delta Q_{xx} = 1.042 \times 10^{41}\,\mathrm{kg\,m^2} \tag{5.20}$$

and adopt a binary separation of 3.3 $R_\odot$. Inserting this into Equation (2.33) yields

$$\frac{\Delta P}{P} = 9.153 \times 10^{-8}. \tag{5.21}$$

Furthermore,

$$O - C = \frac{\Delta P}{P} \frac{P_{\mathrm{mod}}}{2\pi} \tag{5.22}$$

where $P_{\rm mod}$ is the modulation period of the O-C diagram semi-amplitude (see Applegate, 1992) with (2.33). In our case $P_{\rm mod} = 50$ years. Thus

$$O - C = 23\,\mathrm{s}. \tag{5.23}$$

The semi-amplitude obtained from the simulations is closer to the second contribution found by Marchioni et al. (2018), whereas the modulation period is closer to the first one. However, both semi-amplitude and modulation period are somewhat arbitrary as the zero-level of the Q_{xx} plot in the simulations cannot be determined as the $O - C$ diagram in observations. For this reason the numbers obtained from the simulation should be taken as minimum/maximum values rather than precise.

As an example, if we change the binary separation from 3.3 $R_\odot$ to 2.0 $R_\odot$, then the results would be

$$\frac{\Delta P}{P} = 2.942 \times 10^{-7}. \tag{5.24}$$

5.4 Discussion and conclusions

With the aim of searching for the Applegate mechanism in action, we have studied the gravitational quadrupole moment variations arising from magnetic activity through directly solving the 3D MHD equations with the PENCIL CODE.

From the two simulations we have run we see two very different behaviours in the quadrupole moment evolution. In the slow rotator, quasi-periodic oscillations can easily be seen by eye. Meanwhile, in the fast rotator case the evolution is much more complex. This complexity is also observed in the magnetic field evolution. The slow rotator has a relatively simple magnetic field behaviour, showing no magnetic field reversals at all and no migrating dynamo wave. Whereas the fast rotator has a very complex magnetic field evolution. It has a poleward migrating magnetic field at the equator, an overimposed non-axisymmetric dynamo wave which operates only at the north pole. The latter is also decreasing its amplitude.

We establish a link between the magnetic activity and the gravitational quadrupole moment by means of the Reynolds stress tensor and the angular momentum. In his paper Applegate (1992) studied deformations of the star by transitions, which are deformations in which the magnetic field causes the star to change its hydrostatic configuration. He also noted that the quadrupole moment depends upon the distribution of the angular momentum, specially in the outer layers of the star. While in the original Applegate (1992) model the reaction of the quadrupole moment to the changes in the angular momentum and magnetic field are instantaneous, this is not what we see in our simulations. In the case of the slow rotator it takes the density field $\sim$1.77 years to react to the changes in the magnetic field (see Figure 5.14). When plotting Figure 5.26 we can see how Q_{xx} reacts almost immediately to the change in angular momentum at the bottom, whereas at the outer layers there is no correlation.

While in the case of the slow rotator it is relatively easy to observe, in the fast rotator case the behaviour is much more complex. We attribute this to the differences in their respective magnetic field evolution, with the fast rotator presenting a more complex behaviour.

The work by Völschow et al. (2018), based on Lanza (2005) and Lanza (2006), includes the most detailed analytic model of the Applegate mechanism. They applied their model to a set of stars with varying mass. The peak in $\Delta P/P$ was found to lie exactly at the transition from partially- to fully-convective stars, with a value of $\Delta P/P \sim 5 \times 10^{-8}$. This then decreases with growing mass down to a mass of 0.5 $M/M_{\odot}$, and then continues rising. The values of $\Delta P/P$ from our simulations are 2.1×10^{-8} and 9.1×10^{-8} for the slow and fast rotator, respectively, but by decreasing the binary separation one can achieve $\Delta P/P = 2.9 \times 10^{-7}$. The numbers for the period variations in our work seems to converge with the ones reported by Völschow et al. (2018) (see Figure 2.4). From the results reported by Marchioni et al. (2018) for V471 Tau we can obtain the following period variations for the system, where the subindexes 1 and 2 indicates the primary $O-C$ variations and secondary (residuals after the subtraction of the primary contribution), respectively:

$$\left.\frac{\Delta P}{P}\right|_1 \sim 8.6 \times 10^{-7}, \tag{5.25}$$

$$\left.\frac{\Delta P}{P}\right|_2 \sim 4.0 \times 10^{-7}. \tag{5.26}$$

$$\tag{5.27}$$

Our conclusions can be summarized as follows:

1. the complexity of the evolution of Q_{xx} is linked to the complexity in the dynamo waves, angular momentum evolution, and Reynolds stress tensor;
2. the reaction of Q_{xx} to the variations in the magnetic field is not instantaneous and might take years;
3. the numbers of the $O-C$ amplitude and $\Delta P/P$ depend upon the overall magnetic field evolution and complexity;
4. the angular momentum at the bottom of the star is more correlated to Q_{xx} rather than the surface's,
5. ΔQ_{xx} seems to have a strong dependence on stellar rotation; and
6. we have shown for the first time the evolution of the gravitational quadrupole moment from 3D MHD simulations of convection in spherical wedges with the aim of proving the Applegate mechanism.

However, to draw stronger conclusions, more simulations are required in order to explore in more detail the parameter space. In particular, exploring how Q_{xx} depends on stellar rotation and mass is important as the magnetically active companion in PCEBs are rotating at a high fraction of their critical stellar rotation and this

scales with the energetical feasibility of the Applegate mechanism (Navarrete et al., 2018), and fully-convective stars produce a higher amplitude of $\Delta P/P$ (Völschow et al., 2018). Following point (3) based on the analysis of the slow rotator, we encourage observers to look for correlations between the $O-C$ diagram and magnetic activity not only as it would be a 1:1 match, but also to consider a phase shift of the magnetic activity indicators.

We end by emphasizing the limits of the model. While there are variations in Q_{xx}, this numbers should be taken as indicative rather than precise. With the current computational power it is impossible to approach to *real* dimensionless parameters that govern stellar plasmas. For example, the magnetic Prandtl number is 1 in the simulations whereas in the Sun it is $\sim 10^{-5}$. The normalized flux in the bottom of the Sun is $\sim 10^{-11}$ whereas in the simulation it is highly enhanced with a value of 3.2×10^{-5}. In the case of the Reynolds number this is more severe, as in the Sun it ranges from 10^{12} to 10^{13} and in the simulations we have Re ~ 40. However, these simulations in previous studies have already proven to be of extreme success in reproducing some of the solar phenomena (see e.g. Viviani et al., 2018; Käpylä et al., 2016; Käpylä et al., 2013; Käpylä, Mantere, and Brandenburg, 2012). Further development of 3D MHD simulations of fully-convective stars will prove to be of great importance as we expect the Applegate mechanism to be an important tool for studying M dwarfs dynamos through ETVs in PCEBs.

Chapter 6

Conclusions and Future Prospects

Unveiling the origin of eclipsing time variations (ETVs) in close binaries is a hard task. Their origin is an important question to answer because particularly in the case of post-common-envelope binaries (PCEBs), the answer to such questions may end up revealing a new tool to study stellar magnetism, planetary formation, or both. The Applegate mechanism was the focus of this thesis, explored with computational tools, with both 1D and 3D numerical approaches.

By using the 1D stellar evolution MESA CODE we find how the energetics of the Applegate mechanism scale with critical stellar rotation rate (work published in Navarrete et al. (2018)). We see that the Applegate mechanism is energetically feasible in at least some PCEBs, in concordance with Völschow et al. (2016).

The second part of the present thesis explores the Applegate mechanism from 3D magneto-hydrodynamic (MHD) simulations for the first time. The MHD equations were solved using the PENCIL CODE, a fully-compressible MHD code. We looked for variations in the gravitational quadrupole moment Q_{xx} arising from magnetic activity, Reynolds stress, and angular momentum, without any prescription, in a set of two simulations which only differ by the rotation rate: one with three times solar rotation and another with twenty times solar rotation. It was found that the variations of Q_{xx} are very well correlated to the three aforementioned physical quantities for the case of the slow rotator. Whereas in the case of the fast rotator it was found that this link is not trivial because there is complex behaviour of all the quantities mentioned above.

We conclude that the changes in Q_{xx} depend on the excited dynamo wave in the simulations, together with the evolution of the Reynolds stress and angular momentum.

Disentangling between the Applegate mechanism and the planetary hypothesis is not an easy task. Combining theoretical studies with long eclipsing times coverage, magnetic activity measurements, and attempts to direct imaging the proposed third bodies like the one by Hardy et al. (2015) is the only way to solve this problem.

The future work is the development of 3D MHD models of fully convective stars. These models are highly desirable, not only to explore the Applegate mechanism but also for studying the dynamo itself and its impact on their planetary systems. The first step is to start with the model by Dobler, Stix, and Brandenburg (2006), where

they presented a fully-convective model for convection in rotating spheres. This setup did not produce magnetic cycles because it either did not run for long enough or the parameter dependence was not explored in detail; it remained untouched for the following years after the publication of the model.

The idea is to first obtain magnetic cycles with the previously cited model by using more realistic setups and long simulations. Several physical processes can be studied with the simulations, with the Applegate mechanism being only one of them. The magnetic field generation is interesting enough by itself as how the magnetic field is generated in fully convective stars is not yet fully understood. The density fluctuations during a magnetic cycle can be of particular importance in the field of exoplanets as the light time travel effect (LTTE) is routinely used to infer the presence of planets around binary stars (e.g., Borkovits et al., 2016).

We expect the Applegate mechanism to be a promising tool for the area of stellar dynamos in the future.

Bibliography

Almeida, L. A., F. Jablonski, and C. V. Rodrigues (Mar. 2013). "Two Possible Circumbinary Planets in the Eclipsing Post-common Envelope System NSVS 14256825". In: *ApJ* 766, 11, p. 11. DOI: 10.1088/0004-637X/766/1/11. arXiv: 1210.3055 [astro-ph.SR].

Applegate, J. H. (Feb. 1992). "A mechanism for orbital period modulation in close binaries". In: *ApJ* 385, pp. 621–629. DOI: 10.1086/170967.

Baliunas, S. L. et al. (Apr. 1996). "A Dynamo Interpretation of Stellar Activity Cycles". In: *ApJ* 460, p. 848. DOI: 10.1086/177014.

Bear, E. and N. Soker (Oct. 2014). "First- versus second-generation planet formation in post-common envelope binary (PCEB) planetary systems". In: *MNRAS* 444, pp. 1698–1704. DOI: 10.1093/mnras/stu1529. arXiv: 1403.4430 [astro-ph.SR].

Beavers, W. I., A. Lui, and T. J. Herczeg (Jan. 1986). "V471 Tauri - A three-body orbit". In: *ApJ*, pp. 785–787. DOI: 10.1086/163855.

Beuermann, K., S. Dreizler, and F. V. Hessman (July 2013). "The quest for companions to post-common envelope binaries. IV. The 2:1 mean-motion resonance of the planets orbiting NN Serpentis". In: *A&A* 555, A133, A133. DOI: 10.1051/0004-6361/201220510. arXiv: 1305.6494 [astro-ph.SR].

Beuermann, K. et al. (Oct. 2010). "Two planets orbiting the recently formed post-common envelope binary NN Serpentis". In: *A&A* 521, L60, p. L60. DOI: 1,0.1051/0004-6361/201015472. arXiv: 1010.3608 [astro-ph.SR].

Beuermann, K. et al. (Apr. 2012a). "The quest for companions to post-common envelope binaries. II. NSVS14256825 and HS0705+6700". In: *A&A* 540, A8, A8. DOI: 10.1051/0004-6361/201118105. arXiv: 1202.5990 [astro-ph.SR].

Beuermann, K. et al. (July 2012b). "The quest for companions to post-common envelope binaries. III. A reexamination of <ASTROBJ>HW Virginis</ASTROBJ>". In: *A&A* 543, A138, A138. DOI: 10.1051/0004-6361/201219391. arXiv: 1206.3080 [astro-ph.SR].

Biermann, L. (1951). "Bemerkungen über das Rotationsgesetz in irdischen und stellaren Instabilitätszonen. Mit 1 Textabbildung". In: *Z. Astrophys.* 28, p. 304.

Böhm-Vitense, E. (1958). "Über die Wasserstoffkonvektionszone in Sternen verschiedener Effektivtemperaturen und Leuchtkräfte. Mit 5 Textabbildungen". In: *Z. Astrophys.* 46, p. 108.

Boisse, I., X. Bonfils, and N. C. Santos (2012). "SOAP. A tool for the fast computation of photometry and radial velocity induced by stellar spots". In: *A&A* 545, A109, A109. DOI: 10.1051/0004-6361/201219115. arXiv: 1206.5493 [astro-ph.IM].

Borkovits, T. et al. (Feb. 2016). "A comprehensive study of the Kepler triples via eclipse timing". In: *MNRAS* 455, pp. 4136–4165. DOI: 10.1093/mnras/stv2530. arXiv: 1510.08272 [astro-ph.SR].

Bours, M. C. P. et al. (Dec. 2014). "Testing the planetary models of HU Aquarii". In: *MNRAS* 445, pp. 1924–1931. DOI: 10.1093/mnras/stu1879. arXiv: 1409.3586 [astro-ph.SR].

Bours, M. C. P. et al. (Aug. 2016). "Long-term eclipse timing of white dwarf binaries: an observational hint of a magnetic mechanism at work". In: *MNRAS* 460, pp. 3873–3887. DOI: 10.1093/mnras/stw1203. arXiv: 1606.00780 [astro-ph.SR].

Brandenburg, A. (Apr. 2003). "Computational aspects of astrophysical MHD and turbulence". In: *Advances in Nonlinear Dynamics*. Ed. by A. Ferriz-Mas and M. Núñez, p. 269. DOI: 10.1201/9780203493137.ch9.

Brandenburg, A. and W. Dobler (Aug. 2002). "Hydromagnetic turbulence in computer simulations". In: *Computer Physics Communications* 147, pp. 471–475. DOI: 10.1016/S0010-4655(02)00334-X. eprint: astro-ph/0111569.

Brinkworth, C. S. et al. (Jan. 2006). "Detection of a period decrease in NN Ser with ULTRACAM: evidence for strong magnetic braking or an unseen companion". In: *MNRAS* 365, pp. 287–295. DOI: 10.1111/j.1365-2966.2005.09718.x. eprint: astro-ph/0510331.

Cowling, T. G. (Nov. 1933). "The magnetic field of sunspots". In: *MNRAS* 94, pp. 39–48. DOI: 10.1093/mnras/94.1.39.

Dobler, W., M. Stix, and A. Brandenburg (Feb. 2006). "Magnetic Field Generation in Fully Convective Rotating Spheres". In: *ApJ* 638, pp. 336–347. DOI: 10.1086/498634. eprint: astro-ph/0410645.

Dubé, C. and P. Charbonneau (Sept. 2013). "Stellar Dynamos and Cycles from Numerical Simulations of Convection". In: *ApJ* 775, 69, p. 69. DOI: 10.1088/0004-637X/775/1/69.

Faria, J. P. et al. (Apr. 2016). "Uncovering the planets and stellar activity of CoRoT-7 using only radial velocities". In: *A&A* 588, A31, A31. DOI: 10.1051/0004-6361/201527899. arXiv: 1601.07495 [astro-ph.EP].

Goździewski, K. et al. (Apr. 2015). "The HU Aqr planetary system hypothesis revisited". In: *MNRAS* 448, pp. 1118–1136. DOI: 10.1093/mnras/stu2728. arXiv: 1412.5899 [astro-ph.EP].

Guinan, E. F. and E. M. Sion (Aug. 1984). "IUE spectroscopy of the degenerate components in the Hyades close binaries V471 Tauri and HZ9". In: *AJ* 89, pp. 1252–1255. DOI: 10.1086/113619.

Hansen, C. J., S. D. Kawaler, and V. Trimble (2004). *Stellar interiors : physical principles, structure, and evolution*.

Hardy, A. et al. (Feb. 2015). "The First Science Results from Sphere: Disproving the Predicted Brown Dwarf Around V471 Tau". In: *ApJ* 800, L24, p. L24. DOI: 10.1088/2041-8205/800/2/L24. arXiv: 1502.05116 [astro-ph.EP].

Hardy, A. et al. (July 2016). "The detection of dust around NN Ser". In: *MNRAS* 459, pp. 4518–4526. DOI: 10.1093/mnras/stw976. arXiv: 1604.05808 [astro-ph.EP].

Horner, J. et al. (Sept. 2012). "A detailed investigation of the proposed NN Serpentis planetary system". In: *MNRAS* 425, pp. 749–756. DOI: 10.1111/j.1365-2966.2012.21620.x. arXiv: 1207.0038 [astro-ph.EP].

Horner, J. et al. (2013). "A detailed dynamical investigation of the proposed QS Virginis planetary system". In: *Monthly Notices of the Royal Astronomical Society* 435.3, pp. 2033–2039. DOI: 10.1093/mnras/stt1420. eprint: /oup/backfile/content_public/journal/mnras/435/3/10.1093/mnras/stt1420/2/stt1420.pdf. URL: +http://dx.doi.org/10.1093/mnras/stt1420.

Johns-Krull, C. M. and J. A. Valenti (Mar. 1996). "Detection of Strong Magnetic Fields on M Dwarfs". In: *ApJ* 459, p. L95. DOI: 10.1086/309954.

Käpylä, M. J. et al. (May 2016). "Multiple dynamo modes as a mechanism for long-term solar activity variations". In: *A&A* 589, A56, A56. DOI: 10.1051/0004-6361/201527002. arXiv: 1507.05417 [astro-ph.SR].

Käpylä, P. J., M. J. Mantere, and A. Brandenburg (Aug. 2012). "Cyclic Magnetic Activity due to Turbulent Convection in Spherical Wedge Geometry". In: *ApJ* 755, L22, p. L22. DOI: 10.1088/2041-8205/755/1/L22. arXiv: 1205.4719 [astro-ph.SR].

Käpylä, P. J. et al. (July 2011). "Reynolds stress and heat flux in spherical shell convection". In: *A&A* 531, A162, A162. DOI: 10.1051/0004-6361/201015884. arXiv: 1010.1250 [astro-ph.SR].

Käpylä, P. J. et al. (Nov. 2013). "Effects of Enhanced Stratification on Equatorward Dynamo Wave Propagation". In: *ApJ* 778, 41, p. 41. DOI: 10.1088/0004-637X/778/1/41. arXiv: 1301.2595 [astro-ph.SR].

Kippenhahn, R., A. Weigert, and A. Weiss (2012). *Stellar Structure and Evolution*. DOI: 10.1007/978-3-642-30304-3.

Käpylä, Petri (Oct. 2006). "Local numerical modelling of magnetoconvection and turbulence - implications for mean-field theories". In: ISBN: 952-10-3397-5.

Lanza, A. F. (Nov. 2005). "On the orbital period modulation of RS CVn binary systems". In: *MNRAS* 364, pp. 238–246. DOI: 10.1111/j.1365-2966.2005.09559.x.

— (July 2006). "Internal stellar rotation and orbital period modulation in close binary systems". In: *MNRAS* 369, pp. 1773–1779. DOI: 10.1111/j.1365-2966.2006.10415.x.

Lanza, A. F. and M. Rodonò (June 2004). "Magnetic activity and dynamics of close binaries". In: *Astronomische Nachrichten* 325, pp. 393–401. DOI: 10.1002/asna.200310239.

Lee, J. W. et al. (Feb. 2009). "The sdB+M Eclipsing System HW Virginis and its Circumbinary Planets". In: *AJ* 137, pp. 3181–3190. DOI: 10.1088/0004-6256/137/2/3181. arXiv: 0811.3807.

Marchioni, L. et al. (Sept. 2018). "The Mystery of the Invisible Brown Dwarf Companion to the Eclipsing Binary V471 TauriAnalysis of 45 Years of Eclipse Timings Including K2". In: *Research Notes of the American Astronomical Society* 2.3, 179, p. 179. DOI: 10.3847/2515-5172/aae36f.

Maxted, P. F. L. et al. (Dec. 2004). "RXJ2130.6+4710 - an eclipsing white dwarf-M-dwarf binary star". In: *MNRAS* 355, pp. 1143–1154. DOI: 10.1111/j.1365-2966.2004.08393.x. eprint: astro-ph/0409251.

Miyake, Fusa et al. (2017). "Large 14C excursion in 5480 BC indicates an abnormal sun in the mid-Holocene". In: *Proceedings of the National Academy of Sciences* 114.5, pp. 881–884. ISSN: 0027-8424. DOI: 10.1073/pnas.1613144114. eprint: https://www.pnas.org/content/114/5/881.full.pdf. URL: https://www.pnas.org/content/114/5/881.

Morgan, D. P. et al. (Oct. 2012). "The Effects of Close Companions (and Rotation) on the Magnetic Activity of M Dwarfs". In: *AJ* 144, 93, p. 93. DOI: 10.1088/0004-6256/144/4/93. arXiv: 1205.6806 [astro-ph.SR].

Nasiroglu, I. et al. (Mar. 2017). "Is There a Circumbinary Planet around NSVS 14256825?" In: *AJ* 153, 137, p. 137. DOI: 10.3847/1538-3881/aa5d10. arXiv: 1701.05211 [astro-ph.EP].

Navarrete, F. H. et al. (July 2018). "Applegate mechanism in post-common-envelope binaries: Investigating the role of rotation". In: *A&A* 615, A81, A81. DOI: 10.1051/0004-6361/201732425. arXiv: 1803.07637 [astro-ph.SR].

Nelson, B. and A. Young (June 1970). "A New Eclipsing Binary Containing a Very Hot White Dwarf". In: *PASP* 82, p. 699. DOI: 10.1086/128946.

Oshagh, M., R. Heller, and S. Dreizler (Apr. 2017). "How eclipse time variations, eclipse duration variations, and radial velocities can reveal S-type planets in close eclipsing binaries". In: *MNRAS* 466, pp. 4683–4691. DOI: 10.1093/mnras/stw3313. arXiv: 1610.04047 [astro-ph.EP].

Paczynski, B. (1976). "Common Envelope Binaries". In: *Structure and Evolution of Close Binary Systems*. Ed. by P. Eggleton, S. Mitton, and J. Whelan. Vol. 73. IAU Symposium, p. 75.

Parker, E. N. (Sept. 1955). "Hydromagnetic Dynamo Models." In: *ApJ* 122, p. 293. DOI: 10.1086/146087.

Parsons, S. G. et al. (2010). "Precise mass and radius values for the white dwarf and low mass M dwarf in the pre-cataclysmic binary NN Serpentis". In: *Monthly Notices of the Royal Astronomical Society* 402.4, pp. 2591–2608. DOI: 10.1111/j.1365-2966.2009.16072.x. eprint: /oup/backfile/content_public/journal/mnras/402/4/10.1111/j.1365-2966.2009.16072.x/2/mnras0402-2591.pdf. URL: +http://dx.doi.org/10.1111/j.1365-2966.2009.16072.x.

Paxton, B. et al. (Jan. 2011). "Modules for Experiments in Stellar Astrophysics (MESA)". In: *ApJS* 192, 3, p. 3. DOI: 10.1088/0067-0049/192/1/3. arXiv: 1009.1622 [astro-ph.SR].

Perdelwitz, V. et al. (Mar. 2017). "Detection of Accretion X-Rays from QS Vir: Cataclysmic or a Lot of Hot Air?" In: *A&A, submitted*.

Perdelwitz, V. et al. (Sept. 2018). "Long-term variations in the X-ray activity of HR 1099". In: *A&A* 616, A161, A161. DOI: 10.1051/0004-6361/201732222. arXiv: 1806.03033 [astro-ph.SR].

Pulley, D. et al. (Mar. 2018). "The quest for stable circumbinary companions to post-common envelope sdB eclipsing binaries. Does the observational evidence support their existence?" In: *A&A* 611, A48, A48. DOI: 10.1051/0004-6361/201731125. arXiv: 1711.03749 [astro-ph.SR].

Rädler, K.-H. (1980). "Mean-field approach to spherical dynamo models". In: *Astronomische Nachrichten* 301, pp. 101–129. DOI: 10.1002/asna.2103010302.

Robertson, P., A. Roy, and S. Mahadevan (June 2015). "Stellar Activity Mimics a Habitable-zone Planet around Kapteyn's Star". In: *ApJ* 805, L22, p. L22. DOI: 10.1088/2041-8205/805/2/L22. arXiv: 1505.02778 [astro-ph.EP].

Schleicher, D. R. G. and S. Dreizler (Mar. 2014). "Planet formation from the ejecta of common envelopes". In: *A&A* 563, A61, A61. DOI: 10.1051/0004-6361/201322860. arXiv: 1312.3479 [astro-ph.EP].

Schleicher, D. R. G. and R. E. Mennickent (June 2017). "A dynamo mechanism as the potential origin of the long cycle in double periodic variables". In: *A&A* 602, A109, A109. DOI: 10.1051/0004-6361/201628900. arXiv: 1703.03876 [astro-ph.SR].

Schleicher, D. R. G. et al. (June 2015). "Planet formation in post-common-envelope binaries". In: *Astronomische Nachrichten* 336, p. 458. DOI: 10.1002/asna.201412184. arXiv: 1501.01656 [astro-ph.SR].

Schwope, A. D., H. C. Thomas, and K. Beuermann (Apr. 1993). "Discovery of the Bright Eclipsing Polar RX:J2107.9-0518". In: *A&A* 271, p. L25.

Soker, N. (Sept. 2000). "A Solar-like Cycle in Asymptotic Giant Branch Stars". In: *ApJ* 540, pp. 436–441. DOI: 10.1086/309326. eprint: astro-ph/0001281.

Somers, G. et al. (Oct. 2017). "M Dwarf rotation from the *K2* young clusters to the field. I. A Mass-Rotation Correlation at 10 Myr". In: *ArXiv e-prints*. arXiv: 1710.07638 [astro-ph.SR].

Soon, W. H., S. L. Baliunas, and Q. Zhang (Sept. 1993). "An interpretation of cycle periods of stellar chromospheric activity". In: *ApJ* 414, pp. L33–L36. DOI: 10.1086/186989.

Steenbeck, M., F. Krause, and K.-H. Rädler (Apr. 1966). "Berechnung der mittleren LORENTZ-Feldstärke ???? X ???? für ein elektrisch leitendes Medium in turbulenter, durch CORIOLIS-Kräfte beeinflußter Bewegung". In: *Zeitschrift Naturforschung Teil A* 21, p. 369. DOI: 10.1515/zna-1966-0401.

Vaccaro, T. R. et al. (Sept. 2015). "The V471 Tauri System: A Multi-data-type Probe". In: *ApJ* 810, 157, p. 157. DOI: 10.1088/0004-637X/810/2/157. arXiv: 1506.05067 [astro-ph.SR].

Vanderbosch, Z. P. et al. (Mar. 2017). "V471 Tauri: Examining Eclipse Timing Variations with two Independent Clocks". In: *20th European White Dwarf Workshop*. Ed. by P.-E. Tremblay, B. Gaensicke, and T. Marsh. Vol. 509. Astronomical Society of the Pacific Conference Series, pp. 571–574.

Vitense, E. (1953). "Die Wasserstoffkonvektionszone der Sonne. Mit 11 Textabbildungen". In: *Z. Astrophys.* 32, p. 135.

Viviani, M. et al. (Aug. 2018). "Transition from axi- to nonaxisymmetric dynamo modes in spherical convection models of solar-like stars". In: *A&A* 616, A160, A160. DOI: 10.1051/0004-6361/201732191. arXiv: 1710.10222 [astro-ph.SR].

Völschow, M., R. Banerjee, and F. V. Hessman (Feb. 2014). "Second generation planet formation in NN Serpentis?" In: *A&A* 562, A19, A19. DOI: 10.1051/0004-6361/201322111. arXiv: 1312.7512 [astro-ph.EP].

Völschow, M. et al. (Mar. 2016). "Eclipsing time variations in close binary systems: Planetary hypothesis vs. Applegate mechanism". In: *A&A* 587, A34, A34. DOI: 10.1051/0004-6361/201527333. arXiv: 1512.01960 [astro-ph.SR].

Völschow, M. et al. (Nov. 2018). "Physics of the Applegate mechanism: Eclipsing time variations from magnetic activity". In: *A&A* 620, A42, A42. DOI: 10.1051/0004-6361/201833506. arXiv: 1809.00910 [astro-ph.SR].

Warnecke, J. et al. (Dec. 2016). "Influence of a coronal envelope as a free boundary to global convective dynamo simulations". In: *A&A* 596, A115, A115. DOI: 10.1051/0004-6361/201526131. arXiv: 1503.05251 [astro-ph.SR].

Williamson, J. H. (Mar. 1980). "Low-Storage Runge-Kutta Schemes". In: *Journal of Computational Physics* 35, pp. 48–56. DOI: 10.1016/0021-9991(80)90033-9.

Wittenmyer, R. A., J. Horner, and J. P. Marshall (May 2013). "On the dynamical stability of the proposed planetary system orbiting NSVS 14256825". In: *MNRAS* 431, pp. 2150–2154. DOI: 10.1093/mnras/stt299. arXiv: 1302.4137 [astro-ph.EP].

Zahn, J.-P. (Aug. 1989). "Tidal evolution of close binary stars. I - Revisiting the theory of the equilibrium tide". In: *A&A* 220, pp. 112–116.

Zahn, J.-P. and L. Bouchet (Oct. 1989). "Tidal evolution of close binary stars. II - Orbital circularization of late-type binaries". In: *A&A* 223, pp. 112–118.

Zorotovic, M. and M. R. Schreiber (Jan. 2013). "Origin of apparent period variations in eclipsing post-common-envelope binaries". In: *A&A* 549, A95, A95. DOI: 10.1051/0004-6361/201220321. arXiv: 1211.5356 [astro-ph.SR].